INSTITUTO SUPERIOR DE ENGENHARIA DO PORTO
MESTRADO EM ENGENHARIA MECÂNICA




LASER POWDER BED FUSION OF INCONEL® 718: OPTIMIZATION OF PROCESS PARAMETERS AND RESIDUAL STRESS ANALYSIS BEFORE AND AFTER HEAT TREATMENT

RAFAEL DE SÁ BARROS
dezembro de 2019

POLITÉCNICO
DO PORTO

LASER POWDER BED FUSION OF INCONEL® 718: OPTIMIZATION OF PROCESS PARAMETERS AND RESIDUAL STRESS ANALYSIS BEFORE AND AFTER HEAT TREATMENT

Rafael de Sá Barros

2019
ISEP – School of Engineering
Department of Mechanical Engineering

POLITÉCNICO
DO PORTO

POLITÉCNICO
DO PORTO

Instituto Superior de Engenharia do Porto

POLITECNICO DI TORINO

LASER POWDER BED FUSION OF INCONEL® 718: OPTIMIZATION OF PROCESS PARAMETERS AND RESIDUAL STRESS ANALYSIS BEFORE AND AFTER HEAT TREATMENT

Rafael de Sá Barros
1131036

Dissertation presented to ISEP – School of Engineering to fulfill the requirements necessary to obtain a Master's degree in Mechanical Engineering, carried out under the guidance of the Adjunct Professor Francisco José Gomes da Silva (FGS) and co-supervision of the Associate Professor Eleonora Atzeni

2019
ISEP – School of Engineering
Department of Mechanical Engineering

POLITÉCNICO DO PORTO

POLITÉCNICO
DO PORTO

JURY

President
Rui Filipe Neves Araújo Rego, PhD
Adjunct Professor, Department of Mechanical Engineering, ISEP
Supervisor
Francisco José Gomes da Silva, PhD
Adjunct Professor, Department of Mechanical Engineering, ISEP
Co-supervisor
Eleonora Atzeni, PhD
Associate Professor, Department of Management and Production Engineering, POLITO
Examiner
Fernando Jorge Lino Alves, PhD
Associate Professor, Department of Mechanical Engineering, FEUP

KEYWORDS

Metals Additive Manufacturing, Laser Powder Bed Fusion, Inconel® 718, Residual stresses, Hole-drilling strain-gage method

ABSTRACT

Metals Additive Manufacturing (AM) is a “flourishing” technology, developing fast and successfully. Laser Powder Bed Fusion (LPBF) is among the most used metals AM processes in industry. Inconel® 718 (IN718) is a nickel-based superalloy that maintains its exceptional properties at high and low temperatures, thereby, it is a material commonly used to fabricate high performance components.

The purpose of this work is to study the residual stress (RS) evolution of IN718 parts fabricated by LPBF, before and after heat treatment. Firstly, specimens with different combinations of parameters were fabricated to select the optimal LPBF process parameters. With the results from that part of the work, the influence of the individual process parameters on the porosity was studied. Then, new specimens were fabricated with the selected parameters and the RS analyzed by the hole-drilling strain-gage method, in as-built, solution annealed (SA) and SA plus double-aged (DA) conditions.

It was concluded that increasing the scanning speed contributes to the reduction of the porosity. Also, for lower scanning speeds, 400 mm/s and lower, a hatching distance of 0.13 mm was defined as optimal. For higher scanning speeds, 600 and 800 mm/s, no relevant influence of the hatching distance, from 0.05 to 0.11 mm, on the porosity was observed. Laser power and layer thickness were not studied. Larger pores were found in specimens with higher porosity. Also, the specimens with higher porosity presented irregular pores and with lower porosity presented spherical-like pores.

Regarding the RS evolution, as-built top surface presented uniform RS distribution of approximately 400 MPa. Lateral surface presented anisotropic distribution, with RS magnitudes of 600 to 800 MPa in build direction and 200 to 300 MPa horizontally. After the SA heat treatment, the RS decrease greatly to values between 50 – 200 MPa. Series of carbides were found at the grain boundaries, which were attributed as the cause for oscillations in the RS profile. SA plus DA condition presented RS between 10 to 50 MPa. Heat-treated specimens revealed compressive RS at immediately near the surface.

PALAVRAS CHAVE

Fabricação aditiva de metais, Fusão a laser em leito de pó, Inconel® 718, Tensões residuais, Método do furo cego incremental

RESUMO

A fabricação aditiva (FA) de metais é uma tecnologia "florescente", em rápido desenvolvimento e com sucesso. Fusão a laser em leito de pó (LPBF) está entre os processos de FA de metais mais usados na indústria. Inconel® 718 é uma superliga à base de Nickel, que mantém as suas propriedades excecionais a altas e baixas temperaturas, desse modo, é comummente usada para produzir componentes de alto desempenho.

O objetivo deste trabalho é estudar a evolução das tensões residuais (TR) de partes produzidas por LPBF, antes e pós tratamento térmico. Primeiramente, produziram-se amostras com diferentes combinações de parâmetros do processo LPBF para selecionar os melhores parâmetros. Com os resultados obtidos dessa parte do trabalho, foi estudada a influência na porosidade dos diferentes parâmetros. Então, produziram-se novas amostras com os parâmetros selecionados e foram analisadas as TR pelo método do furo cego incremental, nas condições: "as-built", recozido (SA) e SA mais envelhecimento duplo (DA).

Concluiu-se que o aumento da velocidade de varredura contribuí para a redução da porosidade. Também, para velocidades mais baixas, 400 mm/s e abaixo, a distância entre passagens de 0.13 mm foi definida como ótima. Para velocidades mais altas, 600 mm/s e 800 mm/s, a influência da distância entre passagens, de 0.05 a 0.11 mm, na porosidade é desprezível. A potência do laser e a espessura das camadas não foram estudados. Poros maiores foram observados nas amostras com maior porosidade. Também, as amostras com maior porosidade exibiram poros irregulares, e com menor porosidade poros esféricos.

Em relação à evolução das TR, a face superior "as-built" apresentou uma distribuição das TR uniforme de aproximadamente 400 MPa. A face lateral apresentou distribuição anisotrópica, com TR entre 600 e 800 MPa na direção de deposição, e entre 200 e 300 MPa horizontalmente. Nas amostras SA, as TR reduziram substancialmente para valores entre 50 e 200 MPa. Foram detetados conjuntos de carbonetos, aos quais se atribuiu a

ocorrência de oscilações no perfil das TR. A condição SA mais DA apresentou TR entre 10 e 50 MPa. As amostras tratadas termicamente revelaram TR à compressão bem próximo da superfície.

LIST OF SYMBOLS AND ABBREVIATIONS

List of abbreviations

3D	Three-dimensional
AC	Air Cooling
AM	Additive Manufacturing
AMTECH	Advanced Manufacturing Technologies Research Group
ASTM	American Society for Testing and Materials
BCT	Body-Centered Tetragonal
BJ	Binder Jetting
CAD	Computer-Aided Design
CNC	Computer Numeric Control
DA	Double Aging Heat Treatment
DED	Direct Energy Deposition
DIGEP	Department of Management and Production Engineering
DISAT	Department of Applied Science and Technology
DMD	Direct Metal Deposition
DMLS	Direct Metal Laser Sintering
EB	Electron Beam
EBM	Electron Beam Melting
EBSD	Electron backscatter diffraction
EDS	Energy dispersive X-Ray spectroscopy
FA	*Fabricação Aditiva*
FAA	Federal Aviation Administration
FC	Furnace Cooling
FCC	Face-Centered Cubic
FDM	Fused Deposition Modeling
FSAM	Friction Stir Additive Manufacturing
GSC	Green Sand Casting
H	Horizontally Built
HIP	Hot Isostatic Pressing
HO	Homogenization Heat Treatment
HT1	Heat Treatment 1

HT2	Heat Treatment 2
IN718	Inconel® 718
ISO	International Organization for Standardization
L	Lateral Surface
LAM	Laser Additive Manufacturing
LC	3D Laser Cladding
LED	Linear Energy Density
LENS	Laser-Engineered Net Shaping
LOM	Laminated Object Manufacturing
LPBF	Laser Powder Bed Fusion
ND	Neutron Diffraction
OR	Build Orientation
PBF	Powder Bed Fusion
POLITO	Polytechnic University of Turin (*Politecnico di Torino*)
RS	Residual Stress
SA	Solid Solution Annealing Heat Treatment
SEM	Scanning Electron Microscopy
SLA	Stereolithography
SLM	Selective Laser Melting
SLS	Selective Laser Sintering
T	Top Surface
TPMS	Triply Periodic Minimal Surfaces
TR	*Tensões Residuais*
UAM	Ultrasonic Additive Manufacturing
UNS	Unified Numbering System
V	Vertically Built
VED	Volumetric Energy Density
W-EDM	Wire Electrical Discharge Machining
WNR	Material Number (*Werkstoffnummer*)
WQ	Water quenching
XRD	X-ray Diffraction

List of units

°C	Degree Celsius
µm	Micron
g	Gram
g/cm^3	Grams per cubic centimeter
GPa	Gigapascal
h	Hour
HB	Brinell hardness
HRC	Rockwell C hardness

HV	Vickers hardness
J/m	Joules per meter
J/m^3	Joules per cubic meter
J/mm^3	Joules per cubic millimeter
K/m	Kelvins per meter
K/s	Kelvins per second
kHz	Kilohertz
kW	Kilowatt
l/min	Liters per minute
m/min	Meters per minute
mg	Milligram
mm	Millimeter
mm/s	Millimeters per second
mm^2	Square millimeter
mm^2/min	Square meters per minute
mm^3	Cubic millimeter
MPa	Megapascal
nm	Nanometer
rpm	Rotations per minute
W	Watt

List of symbols

$	Dollar
%	Percentage
€	Euro
CoCr	Cobalt-Chromium
DO_{22}	Crystal structure of Gamma double-prime phase
DO_a	Crystal structure of Delta phase
E	Young's modulus
ɣ	Gamma matrix
ɣ'	Gamma prime phase (Ni(Al,Ti))
ɣ''	Gamma double-prime phase (Ni_3Nb)
h	Hatching distance
$L1_2$	Crystal structure of Gamma prime phase
m_a	Mass in air
max	Value of the maximum principal stress
min	Value of the minimum principal stress
m_w	Mass in water
N	Layer number
NbC	Niobium Carbide
P	Laser power

t	Layer thickness
v	Scanning speed
β	Maximum principal stress direction
δ	Delta phase (Ni_3Nb)
ε	Elongation at break
ρ	Volumetric mass density of the specimen
ρ_{IN718}	Volumetric mass density of the Inconel® 718 powder
ρ_w	Volumetric mass density of the water
$\sigma_{0.2}$	Yield strength
σ_{max}	Maximum principal stress
σ_{min}	Minimum principal stress
σ_r	Ultimate tensile strength

FIGURES INDEX

TABLES INDEX

INDEX

INTRODUCTION

1 INTRODUCTION

1.1 CONTEXTUALIZATION

1.1.1 ADDITIVE MANUFACTURING

Additive manufacturing (AM) of metallic parts is a “flourishing” technology with the development of novel materials and process improvements. AM process consists of building parts by a layer-by-layer approach (Gibson, Rosen, & Stucker, 2010; Schmidt et al., 2017; Tofail et al., 2018; Zuback & DebRoy, 2018). A proper software slices the 3D CAD model of the desired part in several thin layers, perpendicular to the build direction, as exaggeratedly exemplified in Figure 1. Thus, the AM machine equipped with an energy source is capable of progressively join thin layers of material on top of each other, forming the part (DebRoy et al., 2018; Ngo, Kashani, Imbalzano, Nguyen, & Hui, 2018). ISO/ASTM 52900:2015 (2015) international standard defines AM as a “process of joining materials to make parts from 3D model data, usually layer upon layer, as opposed to subtractive manufacturing and formative manufacturing methodologies”.

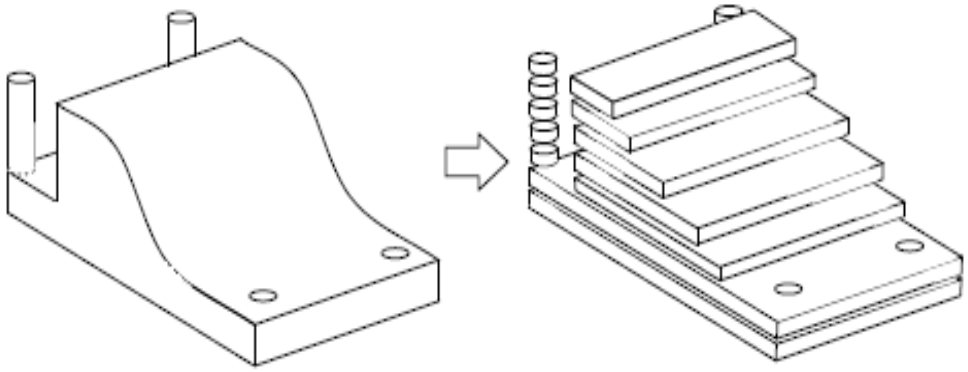

Figure 1 – A rough example of a sliced 3D CAD model (Allaire, Dapogny, Faure, & Michailidis, 2017)

1.1.2 AM BENEFITS AND CHALLENGES

As a layer-by-layer technology, AM is able to build parts with high levels of complexity and is suitable for production of highly customized parts (DebRoy et al., 2018; Ngo et al., 2018; Niaki, Torabi, & Nonino, 2019). Moreover, it produces directly from a 3D CAD model which means that no tools are required, such as punches, dies, cutting tools, etc. Thus, enabling reduction of changeover times and costs, and allowing full customization for each single part (DebRoy et al., 2018; Niaki et al., 2019). Other benefits of AM are (Ålgårdh et al., 2017; DebRoy et al., 2018; Ford & Despeisse, 2016; Gibson & Khorasani, 2019; Gibson et al., 2010; Ngo et al., 2018; Niaki et al., 2019; Wohlers, Campbell, Diegel, Kowen, & Caffrey, 2017):

- Build of near net shape or end-use products in one step;
- Production of high-quality parts with good mechanical properties and very low porosity, usually aided by post-processing techniques;
- Cost efficient for small batch production;
- Build geometry optimized parts with topology optimization (see Figure 2) and lattice-based structures, which can lead to light-weight components;
- Usually, less raw material is required to produce the same complex part when comparing AM with conventional subtractive processes;
- Reusability of raw material (powders processes), being a resource efficient technology;
- Different approaches to the technology, for example, AM can be used to repair or remanufacture parts and surface cladding;
- Design and build of multiple parts as a single one, thus eliminating unnecessary assemblies;
- Produce parts on demand, eliminating the need of spare parts inventory and decreasing lead times.

Figure 2 – Topology optimization focusing on part functionality with GENERATE software from Frustum (USA) (Sher, 2018)

Raw material for metallic materials to be processed via AM process can be supplied in the form of powder, wire (Zuback & DebRoy, 2018) or sheet (DebRoy et al., 2018) depending on the AM process. Owing to these features/benefits, metals AM processes are currently widely found in the production of prototypes, tools and semi-finished or finished products in the aerospace, automotive, biomedical/medical and energy industries (DebRoy et al., 2018; Gibson & Khorasani, 2019; Ngo et al., 2018; Niaki et al., 2019; Wohlers et al., 2017). Despite these benefits, still exists several challenges to spread AM to other industries, such as (Ålgårdh et al., 2017; Ford & Despeisse, 2016; Niaki et al., 2019; Tofail et al., 2018; Wohlers et al., 2017):

- Expensive machines (high acquisition costs), mainly owing to be a technology under development and the need of expensive components (for example, lasers and mirror galvanometers, electron beams, etc.);
- Expensive raw material, as the global volume produced is relatively low when compared to other materials used in conventional manufacturing processes and, specifically, to powder AM processes the powder production is expensive as the AM process requires a specific shape and controlled size distribution of the powder;
- Reduced throughput, it is fundamental to increase the AM throughput to improve productivity, thus reducing amortization costs per part. Throughput can be optimized with full process automatization, faster operating speeds, multiple energy sources, larger build platforms/chambers, etc.;
- Post-processing techniques are usually required to improve surface quality and/or mechanical properties;
- Personnel with lack of competence and no "know-how" inside the company, owing to be a novel technology;
- Lack of proper standards and regulation, however, ISO (International Organization for Standardization) and ASTM (American Society for Testing and Materials) are cooperating in the creation of international standards for AM, regarding different processes and materials. ISO/ASTM 52900 (2015) is the current standard and is under development;
- Immature technology (mainly metals AM), as a recent and in development technology AM cannot give guarantees of standard quality over a long period of production, for example, after a few days of machine running, recalibrations may be needed to ensure a quality within the standards;
- Traditional mindset, an effort must be done to change organizational culture and mindsets to accept new methods and technologies, sometimes this can be the most difficult challenge inside a company.

When justifying the high costs of AM, must be taken into consideration the reduced weight, improved part functionality, reduced maintenance of components, customer satisfaction, and other factors. A process-to-process comparison with conventional manufacturing processes will likely fail (Wohlers et al., 2017). It is believed that AM will replace several conventional processes in diverse industries, however, Gibson and Khorasani (2019) stated that AM technology is not set to replace conventional processes but to give additional opportunities to improve manufacturing as a whole.

1.1.3 HISTORY

The first attempts to create a solid part under a layer-by-layer approach goes back to the late 1960s. At that time, two laser beams with different wavelengths, focused in the middle of a vat of a photopolymer resin, were used to solidify the material at the

intersection point. In 1967, a patent for a similar technique was applied, however, this technology had no success for commercial purposes (Wohlers & Gornet, 2014).

AM technology is available commercially only for the past 30 years. In 1987, 3D Systems (USA) was the first manufacturer to provide an AM system to the market named Stereolithography (SLA). Fused Deposition Modeling (FDM) and Laminated Object Manufacturing (LOM) were introduced in the market by Stratasys (USA) and Helisys Inc. (USA, currently out of business), respectively, in 1991. Selective Laser Sintering (SLS) became available commercially in 1992 by DTM Corporation (USA, acquired by 3D Systems in 2001) to process polymer powders (Wohlers & Gornet, 2014). Others AM technologies were developed during those first years of AM but have not had success commercially or are less known.

In the late 1990s emerged the first metal-based processes to market. AeroMet (UK, currently out of AM business) was founded in 1997 and introduced a process named Laser Additive Manufacturing (LAM), which used a high-power laser as a thermal source and titanium alloys in the form of powders. In 1998, Laser-Engineered Net Shaping (LENS), a metal powder system was commercially available by Optomec (USA). Next year, in Germany, was introduced the Selective Laser Melting (SLM) process, similar to SLS but based in metal powders.

A laser-cladding process using metal powders, Directed Energy Deposition (DED), was introduced in 2000 to manufacture and repair parts. At world fair EuroMold 2001, EOS GmbH (Germany) announced its EOSINT 380 equipment, dedicated to building metal parts based on SLS technology, with significant speed improvements. Also, a new system was presented by Concept Laser GmbH (Germany) combining SLS, laser marking and laser machining in one machine (Wohlers & Gornet, 2014).

Arcam AB (Sweden, acquired recently by GE Additive, now Arcam EBM) are experts on manufacturing Electron Beam Melting (EBM) equipment (work principle similar to SLM) and, in 2002, installed their first two equipments at clients (“Arcam History,” n.d.). In 2009, EOS released two materials to use in their own equipment, a Nickel-based superalloy, Inconel 718 (IN718), and an aluminum alloy, Al-Si10-Mg. At EuroMold 2013, DMG Mori Seiki (Japan) introduced the Lasertec 65, a hybrid machine that combines DED AM process with milling, with 5-axis CNC control. In 2015, Additive Industries (Netherlands) introduced a multi-laser Powder Bed Fusion (PBF) machine, the MetalFAB1 (Wohlers & Gornet, 2014).

Among other important breakthroughs not described, metal AM technology has spread rapidly in the industry in the past 10 years. Even though, between 2014 and 2015 equipment acquisitions has decreased, it recovered in the next years, with metal AM machines manufacturers having difficulties to keep up with the demand, mainly of metal PBF systems, which incorporate LPBF and EBM (Wohlers & Gornet, 2014). Owing to

companies, institutions and government efforts to do research in order to develop and improve this technology, novel processes, materials and machines are expected to surge in the next few years.

1.1.4 ADDITIVE MANUFACTURING MARKET (PRESENT AND FORECASTS)

Wohlers Associates (USA) is an independent consulting firm that has been publishing annual reports about global AM industry for several years. The data found in their reports was obtained from AM systems manufacturers, AM clients and AM service providers (Wohlers et al., 2017). Next, are presented a few graphs with relevant information from the past years about AM growth with data retrieved from Wohlers Report 2017.

The graph of Figure 3 shows the increasing trend of using AM for the production of final parts, from 2003 to 2016. It went from almost nothing (3.9%) to 60.6% in 2016 representing an estimation of $3.66 billion market. However, it is uncertain if production and assembly tools (jigs, fixtures, drills, guides, etc.) are included in these 60.6% (Wohlers et al., 2017).

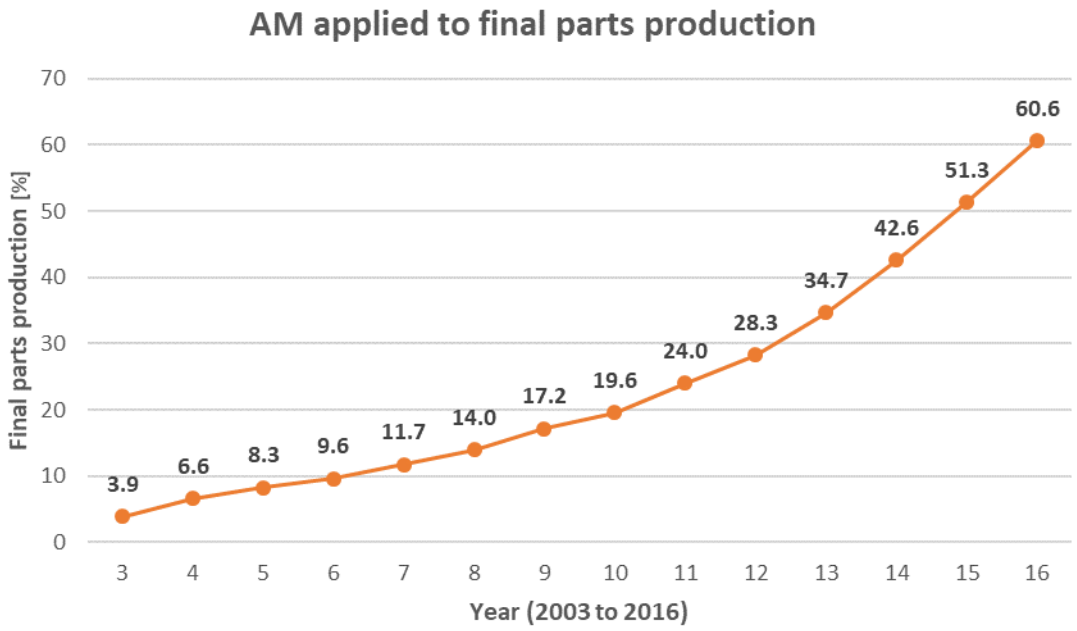

Figure 3 – Additive manufacturing applied to production of final parts, percentage per year (Wohlers et al., 2017)

Figure 5 graph shows the estimated revenue of the past years from the materials sold for AM processes. Orange line represents all material families and blue line is related only with metals. It is estimated that in 2016 a total of $903 million was spent by clients to purchase raw material for their AM processes, an increase of 17.5% from the previous year. Of those $903 million, $126.8 million are only from metals. From 2015 to 2016, metals revenue grew 43.9% (Wohlers et al., 2017).

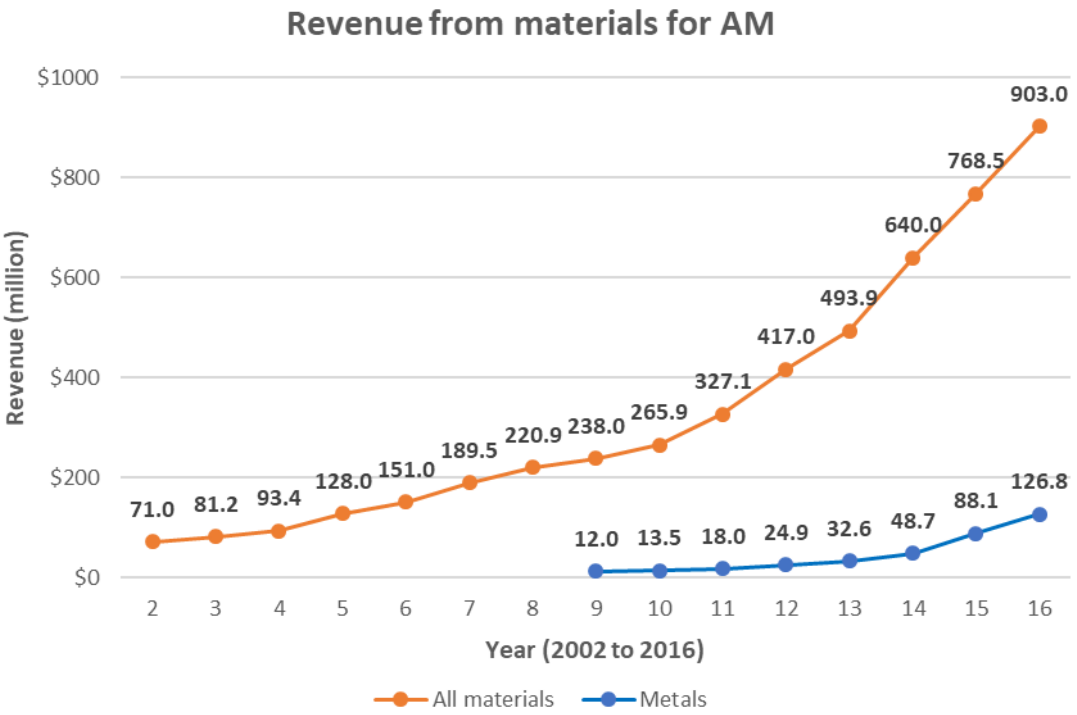

Figure 5 – Revenue of raw materials for additive manufacturing processes (millions of dollars), from 2002 to 2016 (Wohlers et al., 2017)

The circle graph of Figure 4 divides all the $903 million revenue from 2016 into diverse material families. Polymers and filaments take a big segment of the graph, however, metals already take 14%, which is promising (Wohlers et al., 2017).

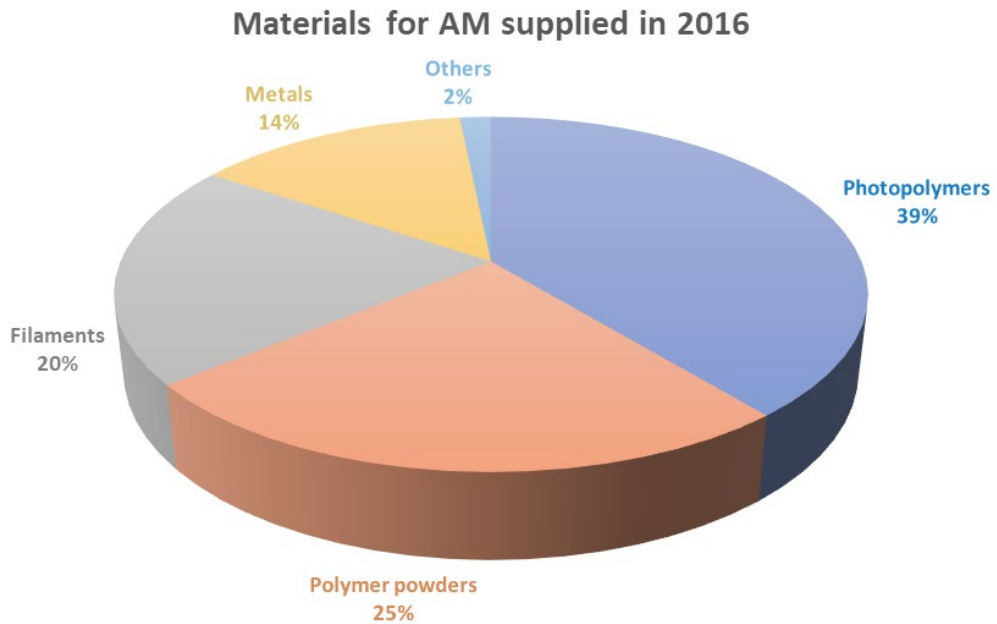

Figure 4 – Percentage of material families corresponding to the raw material revenue of 2016 (Wohlers et al., 2017)

Figure 6 graph represents the annual sales of metals AM machines from 2000 to 2016. A great increase trend can be observed in the last years, with 957 equipments sold in 2016, a 18.4% growth since 2015. In 2016, the average acquisition price of a metal AM

machine was $566,570 and it is estimated that the revenue from 2016 sales was $542.2 million (Wohlers et al., 2017).

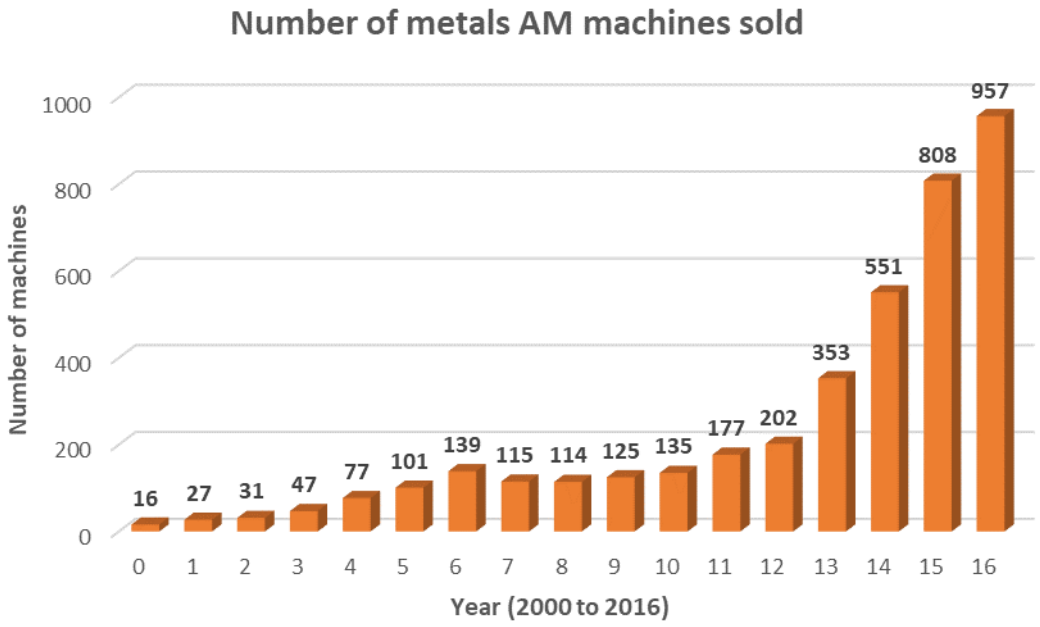

Figure 6 – Number of metals additive manufacturing machines sold per year from 2000 to 2016 (Wohlers et al.,

It is obvious the increasing trend of the AM market. McCue (2018) published an article in Forbes (USA) business magazine about the Wohlers Report 2018 from Wohlers Associate (USA). The global AM market exceeded $7.3 billion in 2017, an increase of 21% in comparison with 2016. Also, an increase of 80% in metals AM machines sold, with 1768 equipments sold, was reported. Recently, McCue (2019) published an article regarding the Wohlers Report 2019, where a forecast of the AM market for the next years is presented. Global AM industry is estimated to reach $15.8 billion by 2020, $23.9 billion by 2022 and $35.6 billion by 2024. Also, it is referred that a total of 177 manufacturers of industrial AM machines were in activity in 2018.

Lately, several large investments have been made to create AM facilities by major brands. Siemens (Germany), BMW (Germany) and Johnson & Johnson (USA) are just a few examples. Siemens (Germany) awarded $135 million to Swinburne University of Technology (Australia) for creation of an Industry 4.0 laboratory focused on AM of carbon composites. BMW (Germany), a cars and motorcycle manufacturer, invested €12.3 million in the foundation of the Additive Manufacturing Campus (Germany), which will focus on the development of new parts for prototypes, series production and customized solutions. Johnson & Johnson (USA), a company related to medical and pharmaceutical industries, launched the Global Centre of Excellence for 3D bioprinting at the Trinity College Dublin (Ireland) (“Major 3D Printing investments,” 2018).

1.2 PURPOSE AND MAIN GOALS

Metals AM is a relatively recent technology, where new techniques are being developed, the existing AM machines and systems are being improved, and "new materials" dedicated specifically to AM processes have been and are being developed. This makes room for a wide range of new studies in a diversity of areas, directly and indirectly, related with AM. The purpose of this work is to understand the residual stress (RS) evolution of parts fabricated by laser PBF (LPBF) with an IN718 powder (material enhanced for AM applications), before and after heat treatment. Thus, this study aims to contribute to the pool of works related with the "new materials" dedicated to AM and the LPBF process.

To accomplish the purpose of this work two main goals have been established. The LPBF machine utilized to carry out this study was recently acquired, thereby, the process parameters for producing IN718 parts with this machine model did not exist in-house. Thus, the first goal is to obtain a set of process parameters capable of producing IN718 parts with acceptable porosity and good mechanical properties. Moreover, the results obtained from the process parameters selection must be analyzed and studied possible individual parameter influences on LPFB-ed IN718.

The second goal is to produce LPBF-ed IN718 specimens for RS analysis, with the previously obtained set of process parameters. To study the RS evolution, some of the specimens will have to be submitted to a standardized heat treatment. The results for the RS analysis must be obtained by the hole-drilling strain-gage method, a technique available in-house. Then a complete analysis of the RS results must be made, and then drawn the respective conclusions.

To accomplish the proposed goals, support the experimental work and highlight the importance of this study, an intense research through the available scientific literature must be made, mainly focusing on the metals AM state-of-the-art and previous works related with LPBF-ed IN718.

1.3 THESIS STRUCTURE

The thesis structure is divided into six chapters and several subchapters. The first chapter, the current one, is the introduction. Herein, firstly, an approach to AM in general is made, then the motivation and objectives of this work are presented, finishing with a few details of the institution where the experimental work was carried out.

The second chapter comprises the bibliographic work, there is presented the state-of-the-art of the metals AM technology encompassing different processes and materials suitable for metals AM. Also, a literature review on IN718 parts/specimens fabricated by AM (mainly fabricated by the LPBF process) is presented. To finish this chapter, is

explained and are introduced a few characteristics of the hole-drilling strain-gage method.

Chapter three contains all the equipments utilized to achieve the results presented in this works and the respective manufacturers and models. Also, a brief methodology is described.

The experimental work is detailed in the chapter four. Firstly, the LPBF equipment, the powder material and the adopted scanning strategy are detailed. Next, the work related to the selection of the best set of process parameters is described. Lastly, the RS analysis is presented with the respective results and discussion.

In the chapter five are detailed all the conclusions, regarding both the process parameters selection and the RS analysis. Posteriorly, are proposed a few interesting topics to address in future works related with LPBF-ed IN718.

The sixth chapter shows all the references and sources of information (books, scientific papers, websites, datasheets, etc.) consulted to write this thesis, sorted alphabetically.

Lastly, the chapter seven comprises auxiliary information fundamental for the development of this thesis. For example, tables from where values were retrieved or complementary results that may be of interest to consult and prove the calculated values presented in the thesis development.

1.4 WELCOMING INSTITUTION

This work was carried out abroad at the Polytechnic University of Turin (POLITO). POLITO is a university based in the city of Turin, Italy, established in 1859. It is among the most prestigious public education and research institutions in the engineering branch, at both international and national levels. By the 2019 QS World University Ranking, POLITO got classified as the thirty-first (31st) best university in the world on the subject of Mechanical, Aeronautical, Manufacturing and Production Engineering. Also, it is a university that puts efforts in building an international student community, with the enrollment of 16% foreign students in the 2017/2018 academic year (“Politecnico at a glance,” 2019).

The experimental work was carried out in two different departments, the Department of Management and Production Engineering (DIGEP) and the Department of Applied Science and Technology (DISAT). At the DIGEP, the specimens were built, and the RS measured and analyzed in partnership with staff from the Advanced Manufacturing Technologies (AMTECH) research group. At the DISAT, were performed activities concerning specimen preparation, porosity evaluation and microstructure analysis.

BIBLIOGRAPHIC WORK

2.1 METAL ADDITIVE MANUFACTURING

2.2 ADDITIVE MANUFACTURING PROCESSES

2.3 MATERIALS FOR ADDITIVE MANUFACTURING

2.4 LITERATURE REVIEW ON INCONEL® 718 IN ADDITIVE MANUFACTURING

2.5 HOLE-DRILLING STRAIN-GAGE METHOD

2 BIBLIOGRAPHIC WORK

In the previous chapter a generic introduction to Additive Manufacturing technology was made. In this chapter the focus is metal AM technology, therefore, whenever the term AM is used henceforward, it is merely related to metal AM.

2.1 METAL ADDITIVE MANUFACTURING

2.1.1 FUNDAMENTALS

PBF and DED are the main AM techniques for production of metallic parts. These techniques use a beam as a high energy density source to selectively melt the material, the most common are a laser or an electron beam (EB) (Bandyopadhyay & Traxel, 2018; DebRoy et al., 2018; Ngo et al., 2018; Schmidt et al., 2017; Zuback & DebRoy, 2018). Both techniques and energy sources will be discussed in detail further, with special regard to LPBF, once it is the technique used to produce the specimens analyzed in this work.

Other AM techniques for manufacturing metallic parts exist or are under development, for example, Ultrasonic Additive Manufacturing (UAM) (Fujii, Shimizu, Sato, & Kokawa, 2016; Hehr & Dapino, 2017; Levy et al., 2018; Wolcott, Hehr, Pawlowski, & Dapino, 2016), Friction Stir Additive Manufacturing (FSAM) (Khodabakhshi & Gerlich, 2018; Sharma et al., 2017; Z. Zhao, Yang, Li, & Li, 2019) and Binder Jetting (BJ) (Bai & Williams, 2015; Mostafaei et al., 2019; Mostafaei, Stevens, Ference, Schmidt, & Chmielus, 2018). However, these had received less attention from the research community or are not suitable for industry yet, needing further developments and improvements.

Regarding to materials for AM, raw material suppliers and machine manufacturers are putting efforts to develop materials exclusive for AM processes, thus increasing the process efficiency and output quality. As well, there is an opportunity to create new materials owing to the AM characteristics, which are extremely distinct from the conventional manufacturing processes.

Diversity of materials for AM is increasing greatly, however, it is limited yet, a few material classes that are available commercially are Nickel-based alloys, Steels, Titanium and its alloys, Aluminum, Cobalt-based and Copper-based alloys, etc. (Bourell et al., 2017; DebRoy et al., 2018; Herzog, Seyda, Wycisk, & Emmelmann, 2016; Ngo et al., 2018). Most common materials for each class and its characteristics related to AM process are discussed ahead, with special regard to the Nickel-based superalloy IN718, material studied in this work.

2.1.2 METAL ADDITIVE MANUFACTURING VS. CONVENTIONAL MANUFACTURING

When comparing AM processes with conventional processes, they are frequently compared with casting and forging or CNC machining. When taking in consideration casting and forging, a comparison of built part properties is generally adopted. Owing to complex metallurgy conditions during AM processes, such as melt pools overlapping, extreme temperature gradients accompanied by rapid solidification and directional heat, microstructure presents a significant refinement and residual stresses are easily generated (Prakash, Nancharaih, & Rao, 2018).

Vevers et al. (2018) compared the mechanical properties of GJS-400-15 (cast Iron material) specimens produced by LPBF and Green Sand Casting (GSC) techniques. Through experimental work, they found similar microstructure in both conditions. LPBF specimens presented slightly high tensile strength and elongation, medium-high hardness compared with GSC range values and greater surface roughness.

Prakash et al. (2018) in a review of LPBF, casting and forging processes concluded that LPBF can obtain parts with higher strength and hardness, in contrast it presents poor fatigue properties, low plasticity and anisotropy. LPBF accuracy and surface roughness are similar with precision casting but lower when compared with precision forging. In the other case, AM processes comparison with CNC machining, a process to process comparison is usually made, which is discussed in Table 1.

Table 1 - Comparison of AM and CNC machining (Gibson et al., 2010; Prakash et al., 2018; Varotsis, n.d.)

Characteristic	Comparison
Work principle	AM is an additive process while CNC machining is a subtractive one, thereby CNC machining requires a “block” of material bigger than the part being produced, cutting tools and fixtures. AM requires feedstock, a substrate and controlled chamber with inert gas at atmosphere pressure or vacuum.
Raw material	Usually, AM leftovers can be reused, and built parts are near net shape, thereby it is a material efficient process. As a subtractive process, CNC machining results in substantial waste of material. However, CNC machining is suitable for a broader range of metals. A few materials are more adequate or easier to work with in AM processes than in CNC machining owing to their properties, for example, Titanium and superalloys such as Inconel®.
Part complexity	AM increases its advantage over CNC machining as much complex the part geometry is. Owing to no need of tools in AM, it is almost a complexity-free technology, while parts

Characteristic	Comparison
	produced by CNC machining can have several geometry constraints due to tool dimensions, fixture devices, jigs, cutting angle, number of axis, etc.
Material properties	CNC machining produces parts with great mechanical properties and with isotropic behavior. AM parts can achieve great mechanical properties also, in as-built condition (with enhanced process parameters) or after post-processing, but they are harder to predict. CNC machining produce parts with well-defined properties because it is more predictable, while AM parts can present voids and anisotropy.
Accuracy	CNC machining is capable of manufacturing parts with high accuracy, tolerances lower as 25 µm are achievable. AM can achieve good accuracy, tolerances of 100 µm or lower are feasible. However, AM accuracy can diversify with the axis, usually Z-axis (build direction) exhibit less accuracy. An overall precision below 50 µm was achieved on Cobalt-Chromium (CoCr) specimens using an EOS GmbH (Germany) machine (Braian, Jönsson, Kevci, & Wennerberg, 2018).
Time	Taking in consideration the same volume of material, it is required less time to remove it in CNC machining, than to add it in AM. However, this is a small part of the whole. While AM can produce one part or more in a single stage, CNC machining requires tools changes, fixture changes and careful process planning (part complexity dependent), thus full time consumed to make a part may be superior in CNC than in AM. This characteristic is very dependent of material used, geometry complexity and accuracy required.
Part size	Currently CNC machining is more suitable to build larger parts. Building large parts with AM processes can be tough, because during process high amount of RS are generated and high deformations are expected. Also, larger chambers are required, and it is costly to control atmosphere of such chambers. Sciaky Inc. (USA) developed an EB-based machine capable of building parts with approximately 5.8 m length and 1.2 m width and height (“The EBAM 300 Series,” 2019).

2.1.3 APPLICATIONS BY INDUSTRY

AM processes are currently widely found in a number of industries, such as, aerospace, automotive, biomedical, medical, energy, etc. (DebRoy et al., 2018; Gibson & Khorasani, 2019; Ngo et al., 2018; Niaki et al., 2019; Wohlers et al., 2017). Currently, the aerospace industry is one of the main drivers of AM. A few examples of parts/components manufactured by AM in the aerospace industry are presented next.

GE Aviation (USA) is currently producing fuel nozzles for their LEAP® engine by AM, shown in Figure 7.a. Thus, a component made of 20 welded parts was reduced to a single part, resulting in a weight reduction of 25% and five times more durable ("Applications for metal AM," n.d.; "GE Reveals How," 2017). In October 2018, a mark of 30000 fuel nozzles produced by AM was reached ("New manufacturing milestone," 2018).

STELIA Aerospace (France) in partnership with Constellium (Netherlands), Centrale Nantes (France) and CT Ingénierie (France), designed a prototype for self-reinforced fuselage panels, shown in Figure 7.b, and used AM to directly build the stiffeners on the surface, eliminating the need of fixing screws or welding ("World Premiere for AM," 2018). RUAG (Switzerland) together with Altair Engineering Inc. (USA) and EOS GmbH (Germany) support, improved an antenna bracket for RUAG's Sentinel satellite through topology optimization, shown in Figure 7.c. Was achieved 40% weight reduction and exceeded by 30% the minimum rigidity requirements. In addition to, this component was certified and approved for its utilization in outer space ("Aerospace: RUAG," n.d.).

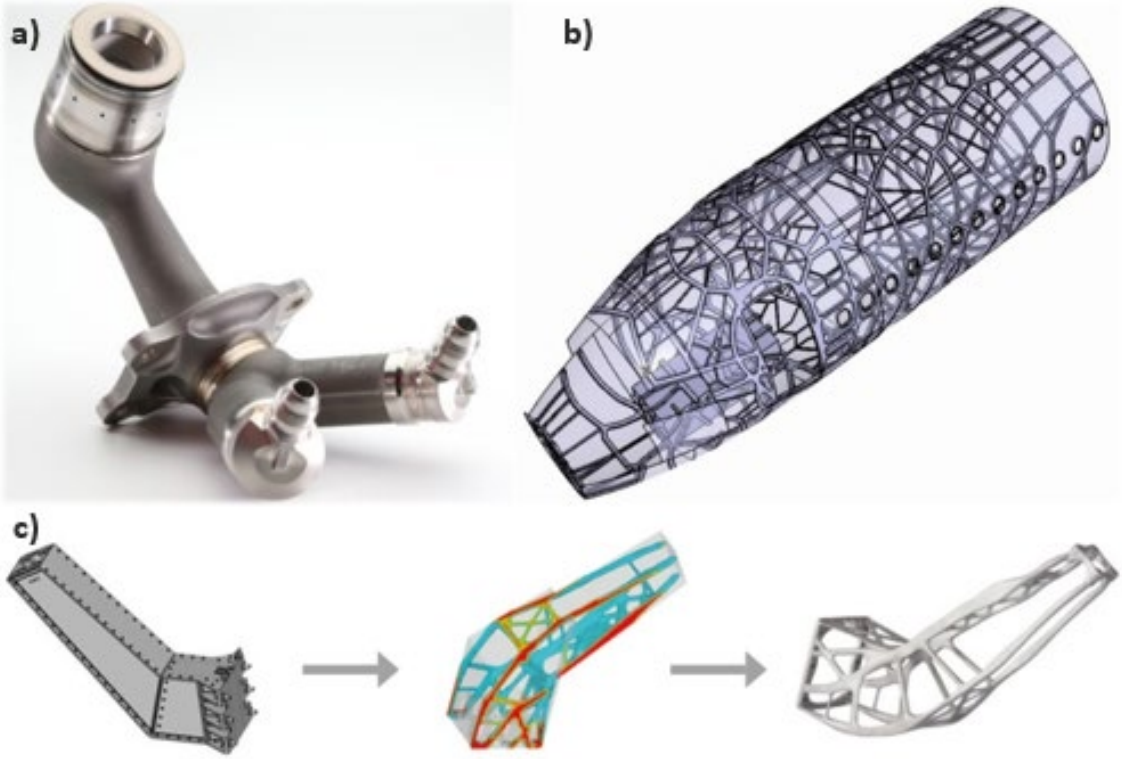

Figure 7 – Examples of AM on aerospace applications: a) LEAP® engine fuel nozzle ("GE Reveals How," 2017); b) STELIA Aerospace self-reinforced fuselage panel ("World Premiere for AM," 2018); and c) topology optimization of antenna bracket for RUAG's satellite ("Aerospace: RUAG," n.d.)

In February 2017, Norsk Titanium (Norway) in collaboration with Boeing (USA) got the World's first structural Titanium component, manufactured by AM, certified by the FAA (Federal Aviation Administration, USA) ("Norsk Titanium to Deliver," 2017). Optomec (USA) offers a service fully dedicated to repair blisks (rotor disk and blades, parts of a turbomachine) through a DED-based process, using materials as Ti-6Al-4V, IN718 and others ("Learn how LENS systems," n.d.).

Great developments are being made in the biomedical and medical industries owing to AM, as it allows to manufacture lattice structures and highly customized parts (parts made in function of the patient's body). AM technology is an opportunity for change on the implants and prosthesis industries.

Liu et al. (2018), Burton et al. (2019) and Alabort et al. (2019) conducted studies and experiments about new designs for metallic implants based on lattice structures produced by PBF processes. Those lattice structures are based on Triply Periodic Minimal Surfaces (TPMS), a few examples are shown in Figure 8. Moreover, Yuan et al. (2019) made a review of AM technology suitability for porous metal implants and TPMS structures. Overall, great results were achieved. The mechanical properties were above the minimums required and owing to TPMS structures, implants can be similar to bone tissues, what enhances the cell growth on the new surface and reduce the body rejection. In addition, Burton et al. (2019) approaches the possibility of using the void space of the lattice structure to carry medicine that will be released over time. All of this is possible owing to the capability of AM to manufacture open cellular structures.

Figure 8 – Examples of TPMS structures for new implants designs with contribution of AM (Burton et al., 2019)

Regarding to the automotive industry, as it is a highly competitive industry, information about specific applications is difficult to find in the literature. AM has several benefits for this industry, such as, faster development cycles, component weight reduction, a smaller number of parts (part consolidation) and customized geometries. AM has been adopted for several years in the automotive industry for rapid prototyping and rapid tooling, nowadays, several automotive manufacturers already started or are making the first steps in investing and adopting AM technology to manufacture end-use parts, a few examples of those manufacturers are: Ford (USA), BMW (Germany), Volkswagen (Germany), Audi (Germany), Bugatti (France), General Motors (USA), Toyota (Japan), etc. (Goehrke, 2018).

2.2 ADDITIVE MANUFACTURING PROCESSES

2.2.1 POWDER BED FUSION

The specimens analyzed in this work were produced by LPBF. The working principle of all PBF processes is similar, coming up with small differences between each other. On the market a few PBF-based processes are found, such as, LPBF, SLM, SLS, Direct Metal Laser Sintering (DMLS), Laser Cusing, EBM, etc. (Gibson et al., 2010; Ngo et al., 2018; X. Zhao et al., 2015). SLS was among the first AM processes to be commercialized. Within the mentioned processes, LPBF and EBM are the most common to produce metallic parts.

PBF processes have a few features in common. A mechanism to supply and spread the powder with a specified layer thickness is essential. Also, one or more thermal sources are required to generate fusion on a controlled region of the layer and a controlled atmosphere to avoid oxidation and degradation of the material. Different fusion mechanisms exist depending on the process and working material, these are: full melting, liquid-phase sintering, chemically-induced binding and solid-state sintering. Regarding to metals, full melting is commonly adopted owing to the capability of producing high-density structures and parts with unique properties (Gibson et al., 2010).

Figure 9 illustrates a schematic view of a LPBF process (Badiru, Valencia, & Liu, 2017). It is composed of a powder reservoir (left side), a build chamber (right side) and a high energy density source system (laser and scanner). The first two have an integrated elevating system, they go up and down, respectively, in function of the layer thickness.

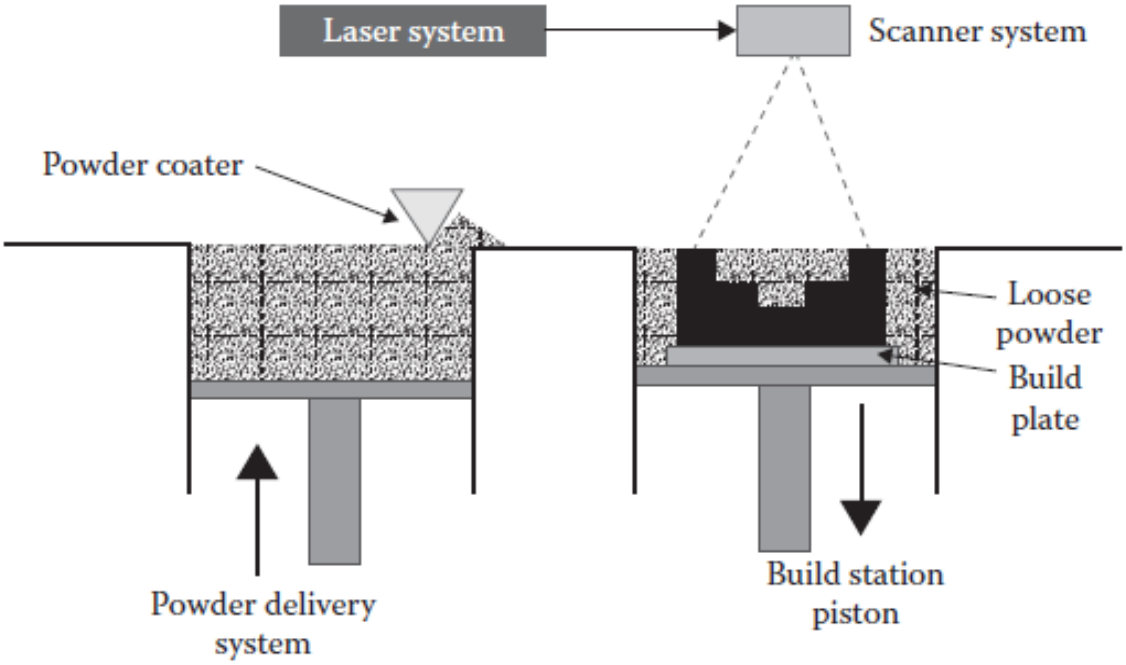

Figure 9 – Schematic representation of LPBF technology (Badiru et al., 2017)

A thin layer of a micro powder (typically 20 to 50 µm) is spread across a substrate (build plate) or the previous layer using a re-coating blade or roller (Zuback & DebRoy, 2018), then a laser through galvanometric mirrors, scans the powder bed surface, melting the new powder and some of the solidified material from the previous layer (important to reach the previous layer to create well-bonded and high-density structures). Thereby, melted material solidifies and the part is built progressively from bottom to top (Z-direction, or also known as build direction) (Ngo et al., 2018; X. Zhao et al., 2015).

Usually, support structures are required, either to support down-facing surfaces, owing to the high-density of the material, or to reduce part distortion, due to the high RS resultant from the extreme temperature gradient, typically, 10^6 K/m for LPBF without substrate preheating (Chow, 2018). The build plate is used to fix the part and avoid its movement during the process, moreover, it works as a heat sink to prevent parts from warping (Wohlers et al., 2017).

The EBM process uses an EB as a heat source. Thereby, the heating mechanism is different from LPBF. On LPBF a laser heats the powder bed via photon absorption, while on the EBM process focused electrons transfer kinetic energy (Zenou & Grainger, 2018). The electrons are deflected when going through a gas at atmospheric pressure, thus the EBM process requires vacuum in the build chamber (small quantity of inert gas is accepted to remove other gases and oxygen) (Gibson et al., 2010). Figure 10 shows a schematic example of an Arcam EBM (Sweden) machine, where is shown the EB column (upper part) and the build chamber (lower part). Inside the column the EB is generated and then the deflection lens controls its position inside the build chamber (Galati & Iuliano, 2018).

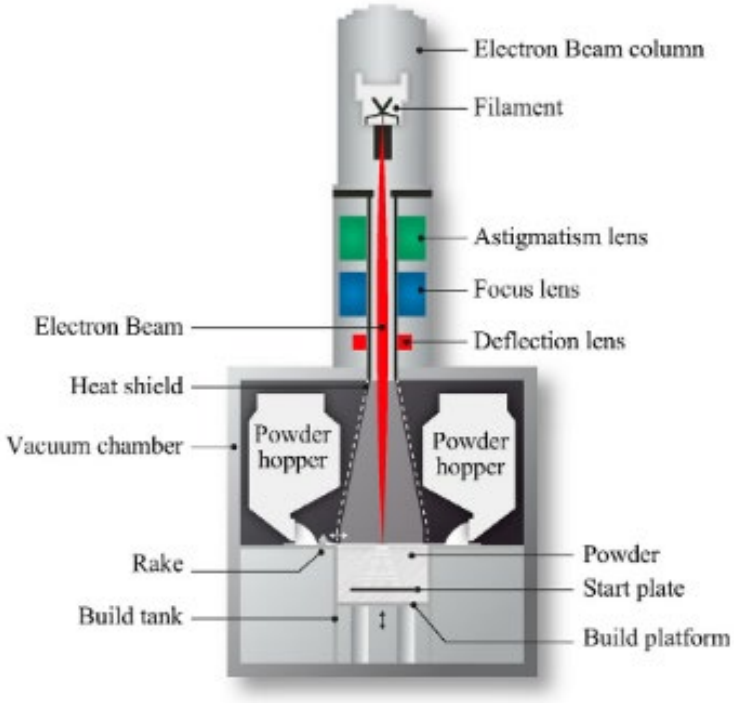

Figure 10 – Schematic example of an Arcam EBM (Sweden) machine (Galati & Iuliano, 2018)

Usually, the powders used on EBM are larger than those on LPBF, the size range can vary from 45 to 105 µm and 15 to 45 µm, respectively (Zenou & Grainger, 2018). Thus, LPBF produces smoother surfaces and more detailed features. The EBM tends to generate lesser RS and different microstructure compared with LPBF. This owing to the required higher preheating temperature of the EBM, resulting in lower temperature gradients (Gibson et al., 2010).

EBM machines can be more expensive than LPBF machines (Wohlers et al., 2017). On the other hand, EBM equipment is more efficient. During the EB generation, most of the electrical energy is converted to the beam, while in laser technology the converted energy efficiency is lower. In the early systems, CO_2 lasers were used, however, not well suitable for the required magnitude of energy in metal AM systems. Nowadays Ytterbium and Nd-YAG lasers are used. The energy cost advantage of EBM is being reduced over time with adopting fiber lasers on LPBF, achieving 70 – 80% conversion efficiency. Many LPBF machines are equipped with laser powers in the range of 200 – 500 W, which is suitable for most of the metals, however, when higher energy is required (above 1 kW), EBM is more suitable at a moderate cost. EBM allows higher scan speed than LPBF. (Gibson et al., 2010; Zenou & Grainger, 2018). Table 2 summarizes all the main characteristics that differentiate from LPBF and EBM processes.

Table 2 – Differences between PBF technologies: LPBF and EBM (Gibson et al., 2010)

Characteristic	LPBF	EBM
Thermal source	Laser	Electron beam
Atmosphere	Inert gas	Vacuum
Beam dynamics	Galvanometric mirrors	Deflection coils
Energy absorption	Absorptivity limited	Conductivity limited
Preheating	Infra-red heaters	Electron beam
Scan speeds	Limited by galvanometer inertia	Very fast (magnetic-driven)
Energy costs	High	Moderate
Surface finish	Excellent to moderate	Moderate to poor
Feature resolution	Excellent	Moderate
Materials	Polymers, metals and ceramics	Metals (conductors)

2.2.2 DIRECTED ENERGY DEPOSITION

DED is also known as Direct Metal Deposition (DMD), LENS from Optomec (USA), 3D Laser Cladding (LC), etc. depending on the application and specific process details. On DED process, a focused thermal source (laser, EB or plasma) melts the material as it is being deposited in the melt pool. The material can be in the form of powder or wire (Gibson et al., 2010; Zenou & Grainger, 2018). Laser is the most common source of thermal energy on DED (Wohlers et al., 2017).

The main constituents of a DED machine are the deposition head and the work base (fixture table), as shown in Figure 11. The deposition head comprises the thermal source, the powder/wire feeder and gas nozzles (in case of powders one nozzle with coaxial channels exist) and, occasionally, control sensors. Simpler machines have a 3-axis system, in those cases, only the deposition head has motion and the build direction is vertical (horizontal layers). More sophisticated systems are available, for example, deposition head fixed in a robotic arm, and 4- or 5-axis machines, where besides the head movements, the work base has one or two motion axes. These improved systems allow to build in other directions than vertical, thus allowing the fabrication of more complex geometries (Gibson et al., 2010; Wohlers et al., 2017; Zenou & Grainger, 2018).

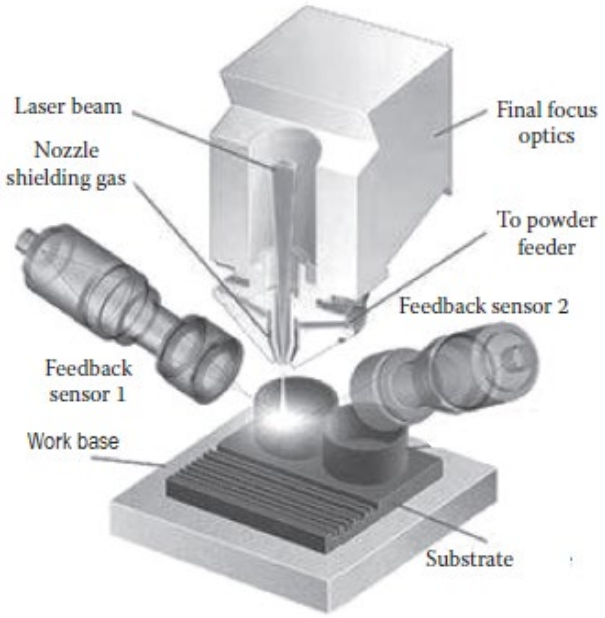

Figure 11 – Schematic representation of DED technology (Badiru et al., 2017)

A substrate or a part needs to be fixed on the work base to start the DED process. For parts to be repaired or remanufactured, the starting surface does not need to be flat. During material deposition and melting, the material must be protected to prevent oxidation, it can be achieved by different approaches. Similar to PBF, a closed chamber filled with an inert gas for laser systems or a chamber under vacuum for EB systems can be used. In addition to, a common technique is localized shielding, where a shielding gas is released directly into the molten pool area, protecting that specific zone during the melting and cooling process. This last approach is not suitable for reactive metals, such as Titanium alloys (Badiru et al., 2017; Gibson et al., 2010; Zenou & Grainger, 2018).

Regarding the type of material supplied, wire is effective for simple geometries, coating or building parts where porosity is acceptable. Otherwise, the powder must be chosen, mainly when complex geometries and nearly fully dense parts are required. Wire feeding is easier to control than powder feeding, this is, wire systems have 100% material capture into the melt pool, while in powder systems capture efficiency is low

(Gibson et al., 2010). Table 3 presents a comparison between the three AM technologies described previously, LPBF, EBM and DED (laser-based).

Table 3 – Comparison of AM technologies: LPBF, EBM and DED (Badiru et al., 2017; Zenou & Grainger, 2018)

Characteristic	LPBF	EBM	DED (laser-based)
Build capacity	Limited	Limited	Large and flexible
Beam size	0.1 – 0.5 mm	0.2 – 1 mm	2 – 4 mm
Layer thickness	15 – 45 µm	45 – 105 µm	0.5 – 1 mm
Build rate	Low	Low	High
Surface finish	Very good	Medium	Coarse
Residual stress	High	Low	High
Feature resolution	Very good	Good	Medium
Repair/Remanufacture	Possible (requires horizontal plane)	Not possible	The most suitable
Multi material	Not possible	Not possible	Possible

2.2.3 ULTRASONIC ADDITIVE MANUFACTURING

Twenty years ago, the first attempts were made to adapt LOM to fabricate parts using sheets of metal, where, firstly the sheets are cut and then stacked and bonded. Yoshino et al. (Yoshino, Obikawa, & Shinozuka, 2000) developed a machine which used low melting point alloys between layers to bond the metal sheets. Yi et al. (S. Yi, Liu, Zhang, & Xiong, 2004) identified two key problems of LOM techniques applied to metals, model accuracy and bonding technology, and then introduced a new approach, bonding the sheets with diffusion welding technology.

Ultrasonic Additive Manufacturing (UAM) is a solid-state joining technique. UAM produces metal parts by bonding thin metal layers (tapes and foils), typically with a thickness between 100-150 µm, on top of each other by ultrasonic metal welding principles. A normal force on top of the build along with ultrasonic vibrations (20 kHz) is applied by a sonotrode (horn) that oscillates transversely to its rolling movement, bonding the previous deposited tapes. Thereby, the most important parameters to control on an UAM process are the normal force, ultrasonic speed and horn travel speed/rolling speed (Levy et al., 2018; Wolcott et al., 2016).

Figure 12 presents a simple schematic of UAM technology (O'Brien & Sinnes, 2015). On it is represented the transducer that produces the rotation movement, the horn that produces the ultrasonic vibrations and the base plate where the part will be built. To increase bond quality and allow bonding of a broader range of materials some mechanisms have two transducers (one in each side of the horn), increasing the welding power (Hehr & Dapino, 2017).

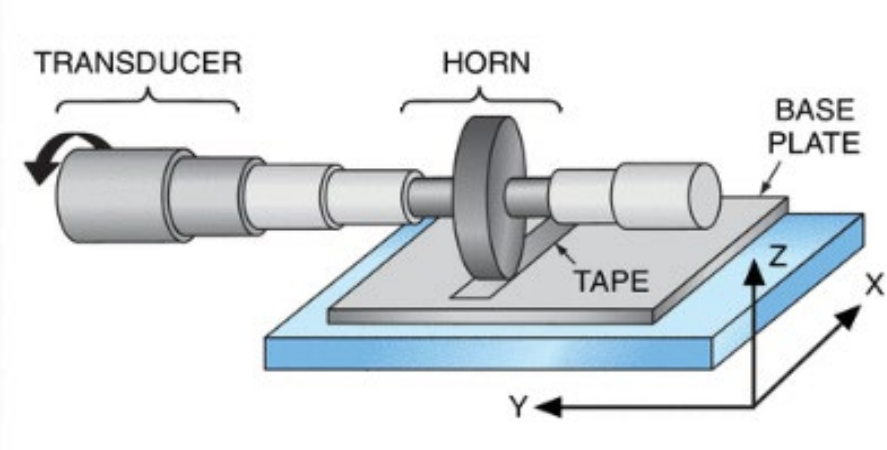

Figure 12 – Schematic representation of UAM technology (O'Brien & Sinnes, 2015)

Defects, such as voids or weak bonding in the interfaces, are detrimental to the mechanical properties of UAM parts (Levy et al., 2018). The key mechanisms present in UAM include the dispersion of surface oxides under pressure to create atomically clean metal surfaces and plastic deformation of the roughness to promote intimate contact between the surfaces being joined. This results in bonding regions with size range of 10 – 20 µm (Gibson et al., 2010; Hehr & Dapino, 2017).

UAM technology does not require high temperatures to join the materials, thus it is considered a low temperature process. Typically, the maximum temperature in the process does not exceed 50% of the melting temperature of the materials being joined. As a layer-by-layer and low temperature technology, UAM brings the possibility to join dissimilar materials and to create smart structures. These structures can have embedded components, such as sensors, actuators, processors and other micro devices that can sense, transmit, control and react in specific environmental conditions (Gibson et al., 2010; Levy et al., 2018; Wolcott et al., 2016).

It is usual to use UAM systems combined with CNC milling systems (Wohlers et al., 2017; Wolcott et al., 2016). Thus, it can be an additive-subtractive process with intermittent bonding and material removal, which can be helpful to create complex features, smart structures and enhanced net-shape parts (elimination of the stair-stepping effect caused by the layer thickness) (Hehr & Dapino, 2017). In addition, by incorporating a CNC system, UAM parts can achieve high dimensional accuracy and better surface finish (Gibson et al., 2010). Bhatt et al. (2019) proposed a robotic cell to perform UAM in order to overcome the difficulties of working with multi-materials and the input of pre-fabricated components between the layers to produce the smart structures.

2.3 MATERIALS FOR ADDITIVE MANUFACTURING

Materials (feedstock) are the main "root" for AM technology development. With the creation of new materials fully dedicated to AM systems, new opportunities arise in the near future of AM (N. Li et al., 2019). A significant range of metallic materials for AM is

available on the market and it is growing every year. Nickel-based alloys, Aluminum alloys, tool steels, stainless steels, Titanium and its alloys, Cobalt-Chromium alloys and Copper-based alloys, are a few examples of the current available materials for AM systems (Herzog et al., 2016; Wohlers et al., 2017). Intermetallic compounds and metal matrix composites are also in the researchers scope in order to produce it by AM technology (N. Li et al., 2019).

2.3.1 NICKEL-BASED ALLOYS

Also known as Nickel-based (Ni-based) superalloys, such alloys have been developed to work at high temperatures in rough environments (Herzog et al., 2016; Ngo et al., 2018). Ni-based alloys exhibit exceptional properties when compared with other alloys, such as high strength and corrosion resistance at high temperatures, as well as ductility and toughness at both high and low temperatures, among others. Therefore, they are suitable for a wide range of applications (DuPont, Lippold, & Kiser, 2009).

The most common Ni-based alloys used in AM are IN718 (Inconel® alloy 718, UNS N07718, WNR 2.4668), IN625 (Inconel® alloy 625, UNS N06625, WNR 2.4856) and Alloy X (Inconel® HX, Hastelloy® X alloy, UNS N06002, WNR 2.4665). These Ni-based alloys have a wide number of alloying elements, therefore, they are complex to use and the microstructure on the as-built condition is extremely dependent on the chemical composition and thermal histories (Zuback & DebRoy, 2018). The samples analyzed in this work were produced with IN718, this specific material will be deeply discussed further in this chapter.

2.3.2 STEELS

Steels are of high interest for AM applications for being the most common engineering material. The application of different steel grades can go from ordinary to high strength and hardness required applications. Austenitic and precipitation hardenable stainless steels, tool steels and maraging steels are the most common grade steels seen in AM processes. As stated previously, AM technology allows to create unique microstructures, which brings great potential to steel parts fabricated by AM, owing to the allotropy of these iron-based alloys. However, rigorous control of the process parameters is required as austenitic and precipitation hardenable stainless steels phase composition is very sensitive to the cooling rate (Herzog et al., 2016; Ngo et al., 2018).

The steels presented next are commonly found in AM processes. Austenitic stainless steel AISI 316L (UNS S31603, WNR 1.4404), as it is of high interest for biomedical industry because of its corrosion resistance and good biocompatibility. Precipitation hardenable stainless steels 17-4PH (UNS S17400, WNR 1.4548) and 15-5PH (UNS S15500, WNR 1.4540), which combines high strength, hardness and good corrosion resistance. Tool steels M2 (UNS T11302, WNR 1.3343) and H13 (UNS T20813, WNR

1.2344), with high strength and good wear resistance, usually are used to manufacture or repair tools and molds. Maraging steel 18Ni300 (UNS K93120,WNR 1.6358), suitable for aerospace applications or tools, owing to its superior mechanical properties (Yan et al., 2019; Zuback & DebRoy, 2018).

2.3.3 ALUMINUM ALLOYS

The availability of Aluminum (Al) alloys for AM systems is rather low. Regardless of the Al high thermal conductivity, which reduces the RS and allows higher processing speeds, there are a few drawbacks. Laser AM processes are not efficient to build Al parts, because Al has a low radiation absorptivity owing to the high reflectivity in a wide range of wavelengths. Moreover, a few high-strength Al alloys, for example, Al 7000 series, contain highly volatile elements (low boiling point) such as Zinc. This can lead to turbulent melt pools, splatter and porosity. Another drawback is the low viscosity of the molten Al, which restricts the melt pool size, therefore, it is preferable PBF over DED to process Al alloys (Herzog et al., 2016; Ngo et al., 2018).

AlSi10Mg (EN AC-43000) and AlSi12 (EN AC-44200) are the most commonly available Al alloys for AM systems (Herzog et al., 2016; Ngo et al., 2018). These Al-Si alloys have a considerable amount of Silicon (Si) in their composition, which promote eutectic solidification. Compared to other Al alloys, these ones have lower melting point which makes them easier to process and overcome the low absorptivity (Zuback & DebRoy, 2018).

2.3.4 TITANIUM AND ITS ALLOYS

Commercially pure Titanium (Ti) and Ti alloys gathered special attention from specific industries, for example, the aerospace industry. This, owing to Ti low specific density (high strength and low density), being ideal to produce high-performance parts (Zuback & DebRoy, 2018). Producing Ti parts by machining brings high processing costs and long lead times, therefore, it is of extreme interest to build Ti parts with AM technology.

Ti6Al4V (UNS R56400, WNR 3.7165) is the Ti alloy that gathered more interest from the research community and has been widely applied in industry to manufacture end-use parts (Herzog et al., 2016; Ngo et al., 2018).

2.4 LITERATURE REVIEW ON INCONEL® 718 IN ADDITIVE MANUFACTURING

Several research works regarding the application of Inconel® 718 in AM processes exist. Some of these works are reviewed and summarized in this subchapter, with special attention to works which focus on microstructure, mechanical properties and RS analysis. Both in as-built and heat-treated conditions of IN718 samples or parts manufactured by PBF processes, mainly LPBF.

Microstructure and mechanical properties of IN718 fabricated by LPBF have been extensively studied over the past years. The first scientific papers published in scientific journals regarding characterization of IN718 samples built with LPBF technology go back to 2012. Wang et al. (2012) published on "Journal of Alloys and Compounds" and Amato et al. (2012) on "Acta Materialia" scientific papers regarding the microstructure and mechanical properties of IN718 samples fabricated by LPBF.

2.4.1 FUNDAMENTALS

Among Ni-based superalloys, IN718 stands out for its excellent properties and characteristics in a wide range of temperatures. IN718 has good corrosion resistance and high strength at temperatures up to 650°C (J. Li et al., 2019; Mostafa, Picazo Rubio, Brailovski, Jahazi, & Medraj, 2017). It is then widely used for high performance components that requires exceptional mechanical properties at extreme temperatures and environments. For example, it is used to manufacture turbine blades, aerospace parts and components for energy power plants (fossil fuel and nuclear energy) (Deng, Peng, Brodin, & Moverare, 2018; Solberg & Berto, 2019; Yu, Hayashi, Kakehi, & Kuo, 2018).

IN718 is a precipitation strengthening alloy. Its microstructure consists of a Face-centered Cubic (FCC) ɣ phase, also known as ɣ matrix, rich in Ni, Cr and Fe. The ɣ matrix is strengthened by precipitating coherent phases, mainly ɣ'' phase (Ni_3Nb), owing to the IN718 high content of Nb, and slightly ɣ' phase (Ni(Al,Ti)) (Tucho, Cuvillier, Sjolyst-Kverneland, & Hansen, 2017). ɣ'' is a metastable phase and can turn into a δ phase (Ni_3Nb), incoherent with the ɣ matrix (Deng et al., 2018). Moderate amounts of δ at the grain boundaries are beneficial to the notch sensitivity of the material, however, high amounts of δ are detrimental to the mechanical properties, decreasing the strength and plasticity of the material (Zhang et al., 2018). Usually, there are also carbide particles and, owing to interdendritic segregation of Nb and other alloying elements, Laves phase $(Ni,Fe,Cr)_2(Mo,Nb,Ti)$, which are detrimental to the mechanical properties requiring a proper heat treatment to be dissolved (X. Wang, Gong, & Chou, 2017).

ɣ'' phase has a Body-centered Tetragonal (BCT) DO_{22} crystal structure and is disk-shaped, ɣ' phase with a face-centered $L1_2$ crystal structure has a spheroidal shape, and δ phase, with the same chemical formula as ɣ'', has an orthorhombic DO_a crystal structure and is needle-like or plate-like shaped. Laves phase, an intermetallic brittle compound, is irregular and island-like shaped (X. Li et al., 2018; X. Wang et al., 2017).

Typical post-processes used to improve the mechanical properties of IN718 parts are heat-treatments, Hot Isostatic Pressing (HIP) and machining. HIP is used to remove internal voids/pores and machining is used to improve dimensional accuracy and the surface roughness, improving the fatigue life (Solberg & Berto, 2019). Usually, IN718 is heat-treated by solid solution annealing (SA) plus double aging treatments (DA) (Zhou,

Mehta, Mcwilliams, Cho, & Sohn, 2019). The SA treatment is intended to dissolve the undesired phases, such as carbides and Laves, and promote the dissolution of interdendritic segregation, while the post DA treatments are performed in order to involve the formation of the strengthening phases ɣ'' and ɣ'. The SA must be done at a temperature between 980 – 1200°C for 1h followed by DA at lower temperatures, between 650 – 900°C (Cao et al., 2018; Tucho et al., 2017).

ASTM F3055 (2014) standard recommends and specify different heat treatments to perform on IN718 parts produced by AM. In order to reduce the internal porosity, HIP should be performed in a temperature range of 1120 to 1185°C at 100 MPa pressure during 3 to 5h. To relief RS and promote recrystallization, homogenization (HO) can be carried out at 1050 – 1080°C during 1.5h followed by air cooling (AC). For SA and DA, ASTM F3055 (2014) suggest to use the same heat treatments as for wrought IN718. SA should be performed at 980°C for 1h followed by AC or water quenching (WQ), per AMS 5662 (SAE, 2016), or at 1065°C for 1h followed by AC or WQ, per AMS 5664 (SAE, 2017). DA should be performed at 720°C for 8h followed by furnace cooling (FC) for 2h to a temperature of 620°C, maintain at that temperature for 8h and then AC, per AMS 5662 (SAE, 2016).

2.4.2 DENSITY

An important property of structures and parts fabricated by AM, particularly those subjected to loads during their working life, is density (as it is related to porosity). When relative density is below 100%, it means the existence of internal cavities, porosities or cracks. One characteristic of AM is the suitability to fabricate parts with porosities and internal cavities, when it is desired, otherwise, it is considered a defect, as it is detrimental to the mechanical properties and fatigue life of the part, which may result in an unexpected fail under load.

LPBF is capable of building parts with nearly 100% relative density, as reported by Wang et al. (2012), Jia et al. (2014), Tao et al. (2019) and others. Jia et al. (2014) stated that the relative density of the parts is connected with the applied laser energy density, this after observing low densification levels accompanied by open pores when applying low laser energy densities.

Different methods exist to measure the density of AM parts (Spierings & Schneider, 2011). Wang et al. (2012) used an Archimedes' method to determine density of IN718 samples produced by LPBF, while Tao et al. (2019) used a micrograph-based method. In a comparison study, Spierings and Schneider (2011) refers a X-Ray scanning approach.

Archimedes' method is standardized by the ASTM B311 (2017) standard. The method consists of measuring the sample mass in the air, m_a, and then in water (distilled or deionized), m_w, as represented in Figure 13, where is schematized the required

equipment. Then, the volumetric mass density of the sample, ρ, is determined using the following equation *(2.1)*:

$$\rho = \frac{m_a \cdot \rho_w}{m_a - m_w} \qquad (2.1)$$

where ρ_w is the density of water in accordance with the laboratory temperature. Despite the fact that it is an easy method to perform, under certain circumstances, it may lead to misleading results, for example, when there are surface pores or cracks that allow water penetration or formation of bubbles not visible to the human eye (Plessis et al., 2018; Slotwinski, Garboczi, & Hebenstreit, 2014).

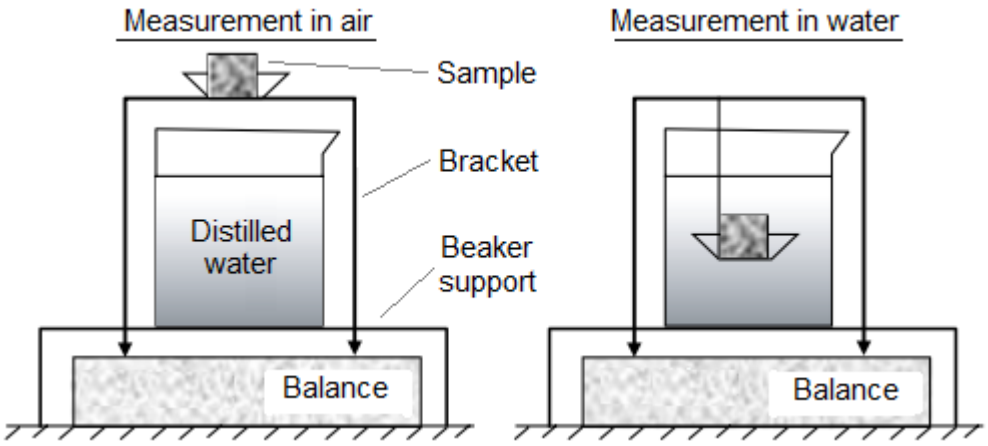

Figure 13 - Schematized illustration of the Archimedes' method, showing the different measurements (Spierings & Schneider, 2011)

Micrograph-based method is a destructive method where the samples need to be cut. After cutting and preparing the surface, images of the cross-section are acquired with an optical microscope at low magnification (in a way that cross-section porosity can be identified). Then, with the aid of an image software, the images are turned into black-and-white images, where the black spots represent the pores. After measuring the area of black spots, it is possible to determine the average porosity and then the density. The drawback of this method is the high deviation of the results (Tao et al., 2019). The X-Ray scanning method generates a 3D image of the sample with a representation of the voids (pores or cracks), however, it is an expensive method and is time consuming for high resolution scanning (in order to detect micro porosity) (Spierings & Schneider, 2011).

2.4.3 MICROSTRUCTURE

Typical characteristics of parts produced by LPBF are shown in Figure 14, which was obtained by low magnification optical microscopy by Li et al. (2018). In that work a "S" scan strategy was adopted, where a continuous laser beam goes forward and back in parallel lines. In addition to, after each layer the pattern rotated 90°. On plane XY (top

view) it is clearly identified the laser beam scanning path, line by line. On plane YZ (front view) it is clearly seen an arch-shaped or “fish-scale” pattern, which represent the cross-section of the laser beam scanning path, i.e., the melt pool profile, which is influenced by the Gaussian energy distribution of the laser. Also, on the plane XZ (lateral view), a similar pattern can slightly be observed, owing to the 90° rotating scan strategy. These characteristics were also reported by other authors under different process parameters and strategies (Tao et al., 2019; Tucho et al., 2017; Z. Wang et al., 2012; Zhang et al., 2018; Zhou et al., 2019).

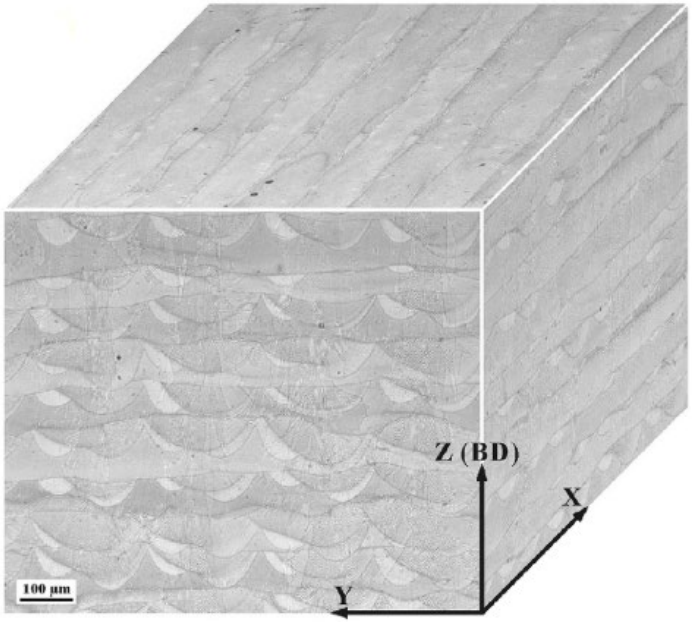

Figure 14 – 3D composite image from lower magnification optical microscopy of IN718 sample fabricated by LPBF (X. Li et al., 2018)

Jia et al. (2014) studied the microstructure features of IN718 parts produced by LPBF under different linear laser energy densities. In that work, was used the linear energy density (J/m), LED, to determine the amount of energy delivered to the powder bed, which was calculated by the equation *(2.2)*. However, it restrains only two parameters, laser power (P) and scannig speed (v). Volumetric energy density (J/m^3), VED, has been widely used in other works related with AM as it enfolds more parameters, it can be determined by the equation *(2.3)*, where h is the hatching distance (distance between laser scan tracks) and t the layer thickness (DebRoy et al., 2018; Herzog et al., 2016; Livescu et al., 2018; Qin et al., 2019; Vrancken, 2016).

$$LED = \frac{P}{v} \qquad (2.2)$$

$$VED = \frac{P}{v \,.\, h \,.\, t} \qquad (2.3)$$

Figure 15 shows the obtained microstructures by Jia et al. (2014) under different LED. Coarsened and fragmented columnar dendrites made of ɣ phase were observed at lower LED, 180 J/m, as shown in Figure 15.a and Figure 15.c. Increasing the energy density delivered to the material, LED of 330 J/m, the columnar dendrites got refined and elongated, presenting an epitaxial growth along build direction (vertical), as seen in Figure 15.b and Figure 15.d. Epitaxial growth along the build direction and fine columnar dendrites are typical characteristics of IN718 parts produced by LPBF, owing to the rapid cooling rate and the heat dissipation through the substrate, as it works as a heat sink (Cao et al., 2018; J. Li et al., 2019; Zhang, Niu, Cao, & Liu, 2015).

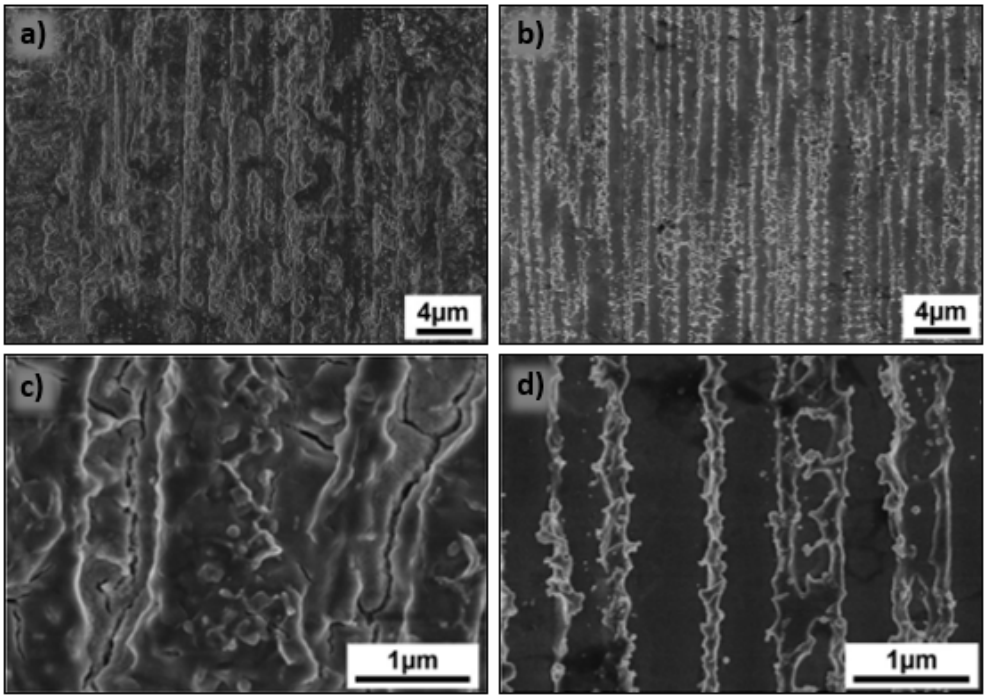

Figure 15 – Microstructure of as-built IN718 samples produced under different LED: a) and c), with lower LED; b) and d), with enhanced parameters, higher LED (Jia & Gu, 2014)

The microstructural evolution of LPBF-ed IN718 samples after heat treatments with different SA temperatures was analyzed by Li et al. (2019). The scan strategy adopted consisted of a pattern of square islands and a rotation of 67° between layers. The typical microstructure of fine columnar dendrites was achieved. In the as-built condition the authors identified the presence of ɣ´´ and ɣ´ phases and no presence of δ phase. The same was observed by Zhang et al. (2018) on a comparative study of microstructure and mechanical properties of parts processed by casting and LPBF processes. In addition, Zhang et al. (2018) also identified a few Carbides at the grain boundaries in the as-built condition.

The temperatures used by Li et al. (2019) to perform SA were 940°C, 980°C, 1020°C and 1060°C for 1.5h followed by WQ. δ phase was then observed, in the heat-treated samples. Plate-like δ phase was formed at the grain boundaries while needle-like δ phase was found heterogeneously distributed in the grains. At higher SA temperatures

the δ phase started to dissolve and at 1020°C was observed that it had completely dissolved into the matrix. DA heat treatment was performed in all of the heat-treated samples, after SA, to precipitate the coherent strengthening phases. First aging treatment was carried out at 720°C for 8h in order to precipitate the ɣ'' phase and the second one at 620°C for 8h, where ɣ' phase precipitated.

Cao et al. (2018) investigated the formation of ɣ'', ɣ' and δ precipitates in the heat-treated condition. After performing SA at 1065°C for 1h, AC plus DA heat treatment, it was identified the presence of three variants of ɣ'' phase with precipitates size between 10 – 50 nm. Also, ɣ' and δ precipitates were found. Li et al. (2019) stated that δ phase was completely dissolved after SA at 1020 ºC, this result may have been affected by the elongated SA time (1.5h) and the cooling method, WQ. However, the typical SA heat treatment applied to IN718 has 1h duration, as it is standardized for wrought and cast IN718 parts.

The effect on microstructure of two different types of heat treatments, HO and SA, was studied by Zhang et al. (2015). In the as-built condition, Laves phases were found in the interdendritic zone and no strengthening phases, as also reported by Li et al. (2018) and Deng et al. (2018). The average primary dendrite arm spacing was determined to be approximately 698 nm, when comparing with the conventional casting process it is seven times smaller in LPBF process, owing to the rapid cooling (Zhang et al., 2015).

HO was performed at 1080°C for 1.5h, AC and the SA at 980°C for 1h, AC. Zhang et al. (2015) stated that the RS existing in the as-built condition benefit the recrystallization during the heat treatments, providing an impetus for grain growth. During the SA, only partial recrystallization occurs, owing to the not high enough temperature and to the grain growth obstruction, by dislocation blocking resultant from the precipitated needle-like δ phase on the grain boundaries.

Fully recrystallization was achieved in the HO heat treatment, however, great variance in grain sizes was observed, what was attributed to the heterogeneous RS distribution, providing different driving forces for recrystallization (Zhang et al., 2015).

Microstructure evolution verified by Deng et al. (2018) in their study of the effect of heat treatments on LPBF-ed IN718 is presented in Figure 16. The yellow squares on the left images (a, c, e, g) represent the area which was magnified and is displayed on the right side (b, d, f, h), respectively.

Figure 16.a corresponds to a direct DA heat treatment, were melt pool boundaries are observed, similar as in the as-built condition, represented by the arc-shaped features in the horizontal direction. As the DA temperature is not high enough, the Laves phase formed during the build process are still present (Figure 16.b). SA plus DA microstructure is shown in Figure 16.c, where can be seen that the melt pool boundaries features

disappeared. In Figure 16.d can be observed that the fine columnar dendritic structures nearly vanished, also can be identified the presence of needle-like δ phase, which precipitated during the SA heat treatment.

After HO plus DA (Figure 16.e) no δ phase was observed and the amount of Laves phase decreased greatly (Figure 16.f). In addition to, the grain coarsening can be easily observed on both images. Figure 16.g corresponds to HO plus SA plus DA. In Figure 16.h, needle-like δ phase is identified. As the Laves phase dissolved during the HO, Nb was released evenly in the matrix, which lead to the precipitation of δ phase during the SA (Deng et al., 2018).

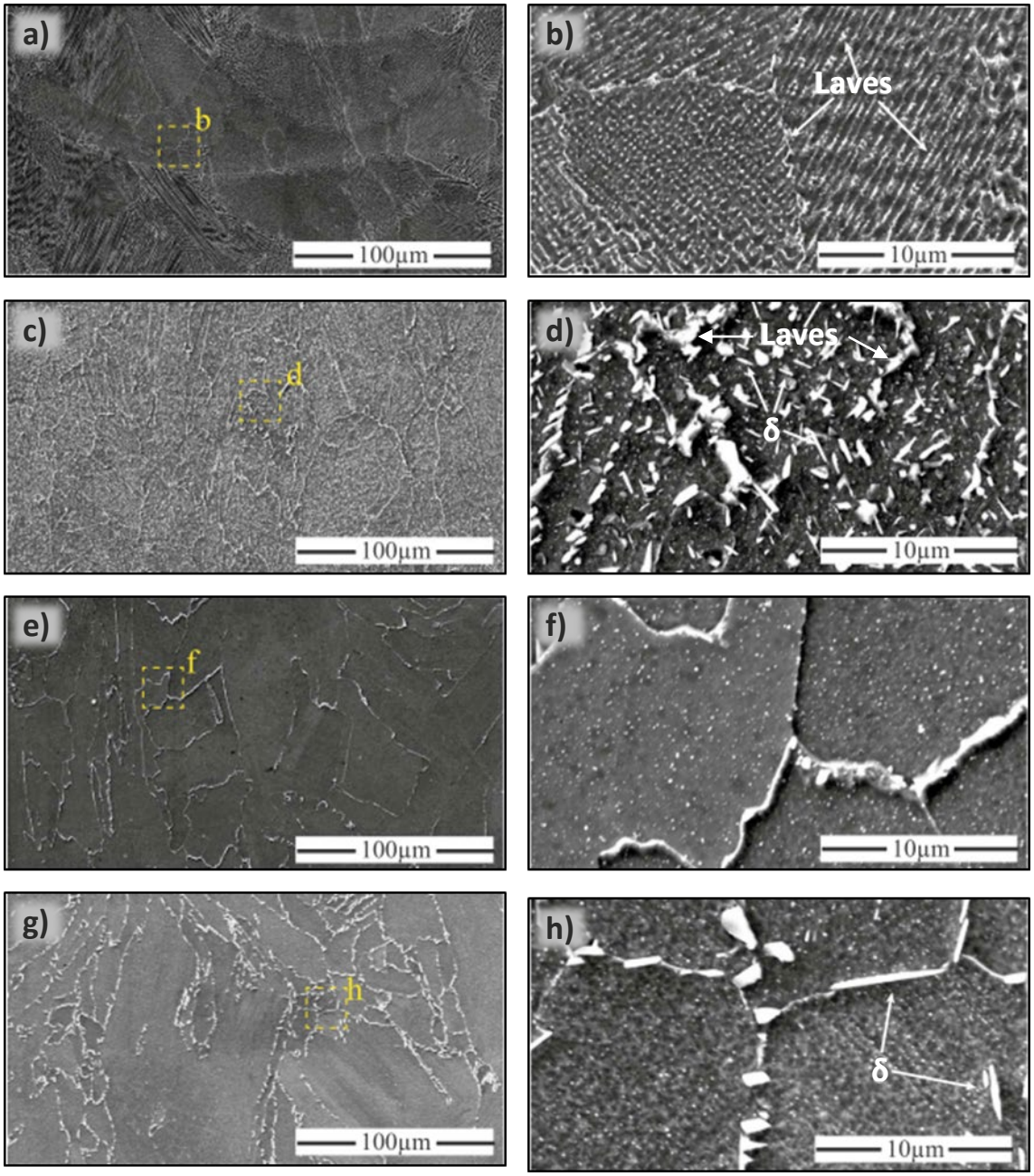

Figure 16 – Microstructure of LPBF-ed IN718 samples after different heat treatments: a) and b), direct DA; c) and d), SA plus DA; e) and f), HO plus DA; and g) and h), HO plus SA plus DA (Deng et al., 2018)

A few more studies of LPBF-ed IN718 in as-built and heat-treated condition exist. Moussaoui et al. (2018) studied the effect of LPBF parameters on microstructure. Chlebus et al. (2015) carried out a work to understand the effect of different heat treatments in cylindrical samples built in different orientations. The chosen orientations were vertical (0,0,1), 45° (0,1,1), 45° x 45° (1,1,1) and horizontal (0,1,0), this assuming the bottom of the specimen positioned at the zero, Y axis as the re-coater travel direction and Z axis as the build direction.

Tucho et al. (2017) tried to completely dissolve the Laves phase into the matrix, performing SA at 1100°C and 1250°C, with different duration times, 1h and 7h for both temperatures. Fully recrystallized microstructure was obtained. Even though the Laves phase decreased greatly, it could not be completely dissolved, remaining tiny precipitates (< 100 nm) on the matrix.

Zhou et al. (2019) performed SA at 980°C and 1065°C for 1h and studied the microstructure and the precipitates evolution between the heat treatment steps. Analyses were done in as-built, direct DA, only SA and SA plus DA conditions.

Popovich et al. (2017) built samples with tailored microstructure and studied the impact of different heat treatments, such as HIP, SA and HIP plus HO plus DA. The LPBF parameters were changed during the building process to build two different microstructures in the same sample. The VED was approximately the same, thereby, the other parameters present in the equation *(2.3)* were altered. On the microstructure analysis, it was clearly observed the coarser grains in the zone processed with higher P, 950 W, and finer grains with lower P, 250 W.

Evolution of the grain boundary network structures was investigated by Holland et al. (2018). Grain orientation mapping, size heterogeneity and distribution were studied. Tao et al. (2019) investigated the solidification process in the scanning tracks by analyzing the characteristics of crystal growth, intercellular spacing and micro segregation.

2.4.4 MECHANICAL PROPERTIES

AM of nickel alloys is a complex process owing to the material chemical composition, which has a wide number of alloying elements. Then, it can precipitate various types of secondary phases, which will affect the ultimate mechanical properties (Zuback & DebRoy, 2018). As stated, IN718 is strengthened by ɣ´´ and ɣ´ phases, which are precipitated during the DA heat treatment. δ phase is formed in the SA heat treatment and its amount must be controlled, as a large amount of δ phase will drastically affect the mechanical properties. However, moderate amounts can be beneficial, as it blocks the dislocation and hamper the grain growth (Zhang et al., 2018).

Regarding IN718 fabricated by LPBF, tensile properties and hardness are the main mechanical properties studied.

Table 4 summarizes most of the results available in the literature obtained by diverse authors for LPBF-ed IN718. Yield strength ($\sigma_{0.2}$), Ultimate tensile strength (σ_r), Young's modulus (E), Elongation at break (ε) and Vickers hardness (HV) are the properties discussed next, in as-built and heat-treated conditions. It is important to highlight that due to the different process parameters selection and machines used, in each single work, the results may diverge from others performed under similar procedures and with same sample conditions.

It can be clearly observed from Table 4 that the tensile properties ($\sigma_{0.2}$ and σ_r) and hardness values are highly improved after performing proper heat treatments. Worst mechanical properties than those in as-built condition were observed when the heat treatment consisted of only SA, as verified by the results of Zhou et al. (2019) and Tucho et al. (2017). These results highlight the importance of performing the DA heat treatment. Trosch et al. (2016) and Zhang et al. (2018) with proper heat treatments performed in LPBF-ed IN718 parts, obtained tensile properties similar to wrought IN718.

Tensile properties obtained in as-built and SA plus DA conditions by Deng et al. (2018), Wang et al. (2012), Zhang et al. (2015) and Chlebus et al. (2015) are compared in the graphs of Figure 17. Despite of the result fluctuation between the different works, it can be observed that the $\sigma_{0.2}$ increased greatly with the heat treatment. σ_r is not represented in the graph but follows the same trend. Relatively to elongation at break the values follow a reverse trend, decreasing with the heat treatment. Deng et al. (2018) stated that the reason for this behavior in mechanical properties is the lack of strengthening phases, such as ɣ'' and ɣ', on the as-built condition, as those are precipitated in the ageing heat treatment.

Regarding the build orientation, horizontal built samples have higher $\sigma_{0.2}$ and σ_r, and lower ε than those built on vertical (Chlebus et al., 2015; Deng et al., 2018). This behavior is identified in Figure 18.a for $\sigma_{0.2}$, σ_r follows the same trend, and in Figure 18.b for ε. After studying this effect, Deng et al. (2018) concluded that the mechanical properties vary with the build orientation, owing to the different crystallographic orientations and the different magnitudes of RS installed.

Deng et al. (2018) also observed that after performing a heat treatment with higher temperatures, the $\sigma_{0.2}$ and σ_r deviation between vertical and horizontal built samples decreased, it can be observed in Figure 18.a for $\sigma_{0.2}$. This behavior was attributed to the relief of the residual stresses, thereby, the main strength mechanism is the precipitated strengthening phases, which are not orientation dependent (Deng et al., 2018). Also, the modification of the crystallographic features contributes to the isotropy of the mechanical properties of the material.

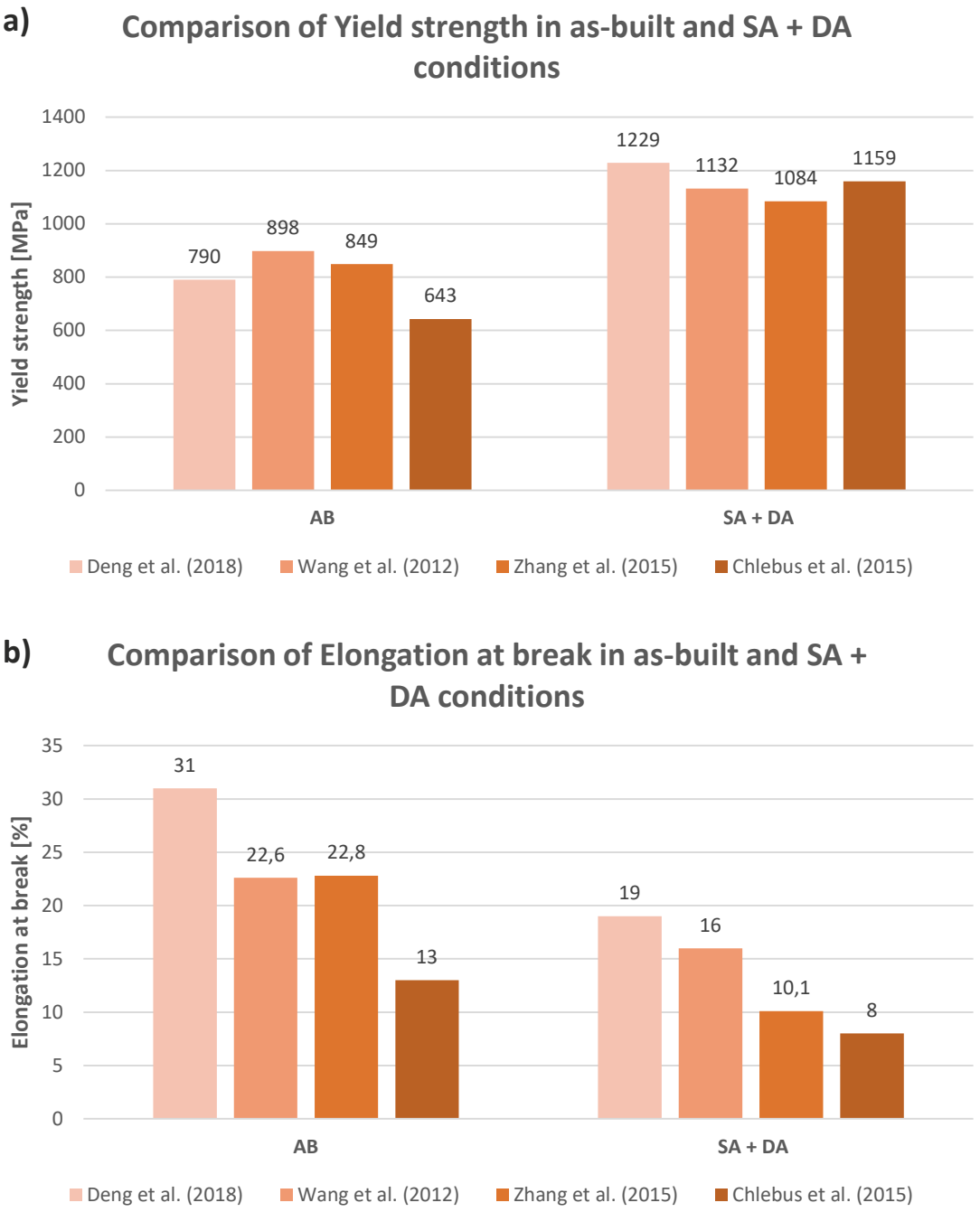

Figure 17 – Comparison of tensile properties in AB and SA plus DA conditions: a) Yield strength; and b) Elongation at break (results retrieved from diverse literature)

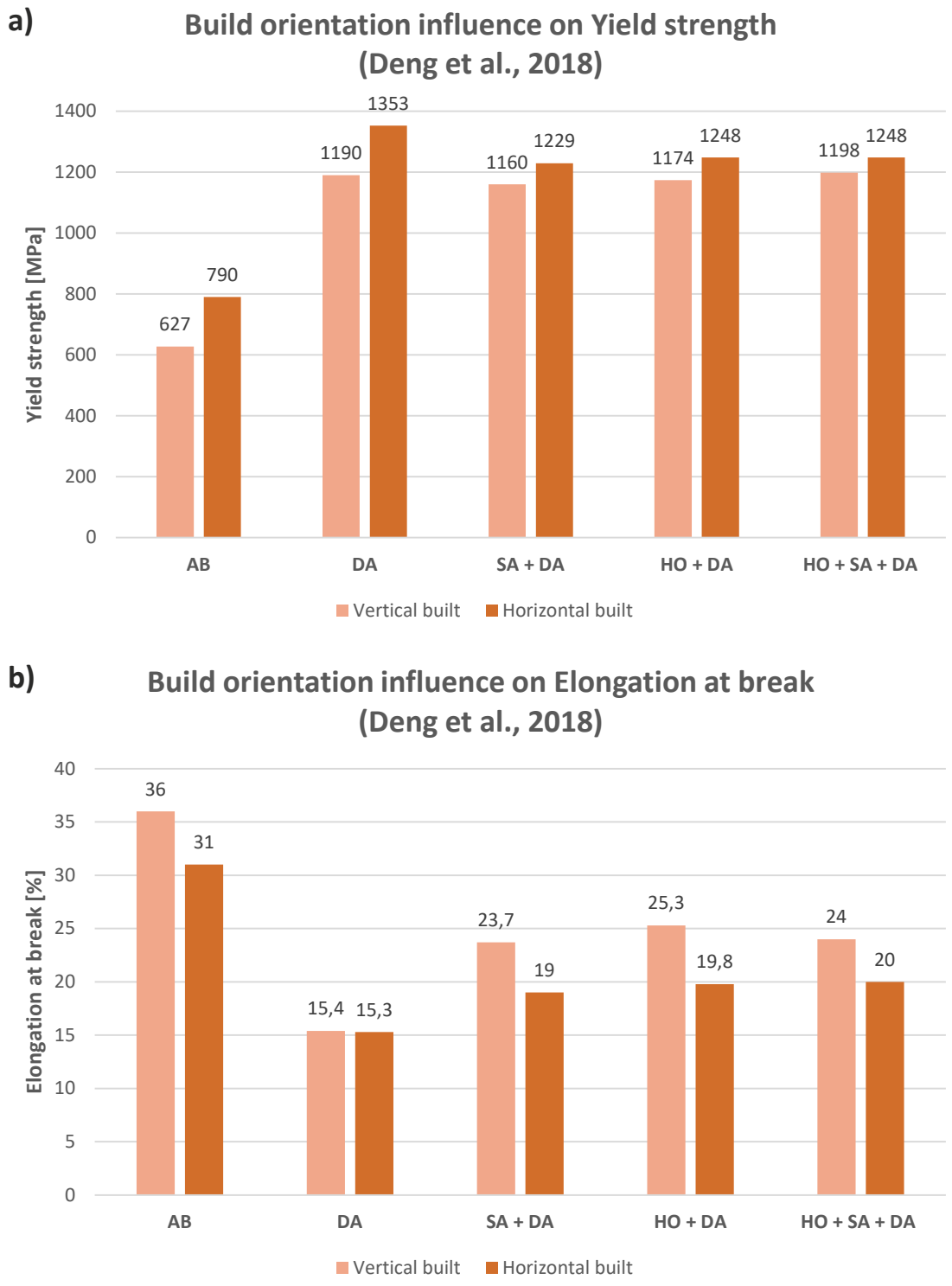

Figure 18 – Build orientation influence: a) Yield strength; and b) Elongation at break, after different heat treatments (Deng et al., 2018)

Table 4 – Mechanical properties of LPBF-ed IN718 in as-built and heat-treated conditions (literature review)

Condition [1]	OR [2]	$\sigma_{0.2}$ [MPa]	σ_r [MPa]	E [GPa]	ε [%]	HV	Source
AB		627	990	203	36	325	(Deng et al., 2018)
		790	1069	200	31	331	
DA		1190	1418	205	15.4	494	
		1353	1509	202	15.3	497	
SA (WQ) + DA	V	1160	1389	199	23.7	491	
	H	1229	1481	212	19	485	
HO (WQ) + DA		1174	1367	210	25.3	495	
		1248	1440	220	19.8	487	
HO (WQ) + SA (WQ) + DA		1198	1371	205	24	487	
		1248	1433	205	20	493	
AB	H	-	-		-	322	(Moussaoui et al., 2018)
HIP + SA + DA	V	1104	1355	-	18.8	477	
	H	1123	1384		22	477	
AB	H	898	1143	-	22.6	365	(Z. Wang et al., 2012)
SA + DA		1132	1319		16	470	
AB	H	-	-	-	-	298	(Amato et al., 2012)
HIP + SA (0.5h)	V	850	1140		28	322	
	H	890	1200		28	369	
SA (1160°C, 4h)	H	-	-		-	382	
AB	H	849	1126	-	22.8	307	(Zhang et al., 2015)
SA + DA		1084	1371		10.1	424	
HO (1.5h) + DA	H	1174	1451	-	13.5	448	(Zhang et al., 2018)
HO (1.5h) + SA + DA		1046	1371		12.3	415	
AB (re-scanned)		572	904	162	19	313	(Chlebus et al., 2015)
		643	991	193	13		
	V	590	954	200	20		
	H	723	1117	208	16		
SA (1100°C, WQ) + DA (620°C for 10h)	45	1074	1320	163	19	463	
	45*45	1159	1377	199	8		
		1152	1371	188	15		
		1241	1457	209	14		
SA + DA (tensile test at room temperature)		1180	1400	-	20.4	-	(Trosch et al., 2016)
		1186	1440		18.5		
		1190	1450		16.9		
SA + DA (tensile test at 450°C)	V	1026	1160		15.9		
	H	1033	1216		12.4		
	45	1080	1255		12.8		
SA + DA (tensile test at 650°C)		860	992		14.2		
		870	1011		3.6		
		855	1074		5.8		

Condition [1]	OR [2]	$\sigma_{0.2}$ [MPa]	σ_r [MPa]	E [GPa]	ε [%]	HV	Source
AB	-	-	-	208	-	296	(Zhou et al., 2019)
SA (WQ)				193		267	
DA				226		467	
SA (WQ) + DA				209		458	
SA (1065°C, WQ)				181		235	
SA (1065°C, WQ) + DA				226		477	
AB	xy xz	-	-	-	-	436 419	(J. Li et al., 2019)
SA (940°C, 1.5h, WQ) + DA						466 437	
SA (980°C, 1.5h, WQ) + DA						511 496	
SA (1020°C, 1.5h, WQ) + DA						487 473	
SA (1060°C, 1.5h, WQ) + DA						480 470	
AB	H	-	-	-	-	304	(Tucho et al., 2017)
SA (1100°C, 1h, WQ)						258	
SA (1100°C, 7h, WQ)						217	
SA (1250°C, 1h, WQ)						210	
SA (1250°C, 7h, WQ)						207	
AB (P = 250 W)	V	668	1011	173	22	320	(Popovich et al., 2017)
SA (850°C, 2h) ^{250}		875	1153	190	17	360	
HIP (150 MPa) ^{250}		645	1025	188	38	310	
HIP + HO + DA ^{250}		1145	1376	190	19	468	
AB (P = 950 W)		531	866	113	21	287	
SA (850°C, 2h) ^{950}		668	884	138	7	338	
HIP (150 MPa) ^{950}		481	788	183	34	262	
HIP + HO + DA ^{950}		1065	1272	188	15	451	
AB (tailored 250/950)		574	873	136	13	285	
SA (850°C, 2h) $^{250/950}$		704	920	167	4	335	
HIP (150 MPa) $^{250/950}$		500	817	187	21	260	
HIP + HO + DA $^{250/950}$		1041	1154	196	7	462	

[1] Sample condition: AB – as-built; SA – solution treated (980°C, 1h, AC) and DA – double aged (720°C, 8h, FC, 2h, 620°C, 8h, AC) per ASM 5662 (SAE, 2016); HO – homogenization (1050 to 1080°C, 1.5h, AC) and HIP – hot isostatic pressing (1120 to 1185°C, 100 MPa, 3 to 5h, AC) per ASTM F3055 (ASTM, 2014); and, if any heat treatment parameter differs from the specified, the parameter is pointed out in parenthesis.

[2] Build orientation: V – parallel to the build direction, vertical; H – perpendicular to the build direction, horizontal; 45 – rotation of 45°; 45*45 – rotation of 45° in both directions; and, xy and xz, plane where the hardness was measured.

2.4.5 RESIDUAL STRESSES

Heterogeneous plastic strains are the source for the RS and these strains can be induced by thermal or mechanical principles (Vrancken, 2016). In LPBF, RS are introduced by thermal principles and they are very common owing to the rapid cooling of the melt pool (Deng et al., 2018). RS are largely spatially non-uniform in AM, which can be detrimental for the mechanical properties and fatigue life. Also, during the building process, they can reduce the dimensional accuracy and lead to geometrical defects, such as distortion and layer delamination (DebRoy et al., 2018). Thereby, it is crucial to know the expected magnitude and orientation of the RS in order to carry out safe and accurate predictions of the final part properties (Bartlett & Li, 2019). Moreover, in this way, it is possible to evaluate a specific post-heat treatment to reduce the RS.

Only a few scientific works are available in the literature about RS on IN718 parts fabricated by LPBF. Yi et al. (2019) had not studied the RS directly, but studied the deformation of sectioned samples under different LED. Larger deformations were found with higher LED, which means that higher LED resulted in higher RS.

The influence of different “island” scanning strategy sizes on the RS was studied by Lu et al. (2015). Samples with “island” size of 2 x 2 mm^2 were the ones with lower RS, however, cracking was observed during the process, what may have contributed to RS relief. 3 x 3 mm^2 size samples generated the higher RS. The scanning strategy with acceptable porosity, no cracking observed, and lower RS was of the size 5 x 5 mm^2.

Ahmad et al. (2018) applied the contour method to determine the RS in LPBF-ed IN718 samples. Near the surface were found tensile stresses above 800 MPa and in the middle of the sample compressive stresses over 400 MPa. Deng et al. (2018) also observed RS of the same magnitude on the surface of as-built samples, the results obtained consisted of tensile stresses of 797.8 MPa and 749.9 MPa on horizontal and vertical built samples, respectively.

Nadammal et al. (2017) measured the surface RS of IN718 samples built with different scanning strategies in order to understand the effect of short and long-distance scan vectors. No direct correlation between RS and scan vector length was observed, just a larger dispersion for the measured results for the scan strategy with longer scan vectors. It is important to highlight from this work that constant compressive stresses from approximately 200 to 400 MPa were found in samples built with short scan vectors, mainly in measures performed along the build direction. Owing to the lack of more relevant works relating RS and LPBF-ed IN718, RS aspects are discussed next for LPBF in general.

The main physical factors that contribute to the RS in LPBF are based on the high scan speed of the laser beam on the powder bed along with the laser power and layer

thickness, which originates high temperature gradients accompanied by rapid heating and cooling rates (about 10^6 K/s for LPBF (Yadroitsev & Yadroitsava, 2015)). These are responsible for the thermal expansion and contraction of the melted material. The next layer to be built is deposited on top of the previous layer or on the substrate, which are at a much lower temperature than the melted material (high temperature gradient). Just after the deposition, the material is divided into a softer hot zone (melted material) and a stronger cold zone (surrounding material), this will generate uneven plastic deformations that will remain accumulated inside the material as RS (DebRoy et al., 2018; Vrancken, 2016).

RS can be classified by Type I, Type II and Type III, depending on the size scale which they are generated and act, as exemplified in Figure 19 by the arrows. Type I can result in severe distortion of the part if the boundary conditions are changed, as they act at macro scale in the whole body. Type II are originated from the differences in grain orientations and anisotropy in crystal structure, this type of RS is common on polycrystalline materials. Type III act in the atomic scale, they exist owing to defects in the crystal lattice, such as atoms dislocations and substitutions. Type I are considered macroscopic RS and are the most important to consider. Type II and III are microscopic RS and are less impactful, however, on multi-phases materials, development of local RS is common, resulting from the different phases behavior to plastic strain and neighbor grains with different crystal orientations (Bartlett & Li, 2019; Vrancken, 2016).

Vrancken (2016) reviewed several works related to LPBF in order to understand the influence of individual parameters from Equation *(2.3)* on the RS magnitude. It was concluded that lower RS can be achieved through lowering the scan speed (v), increasing

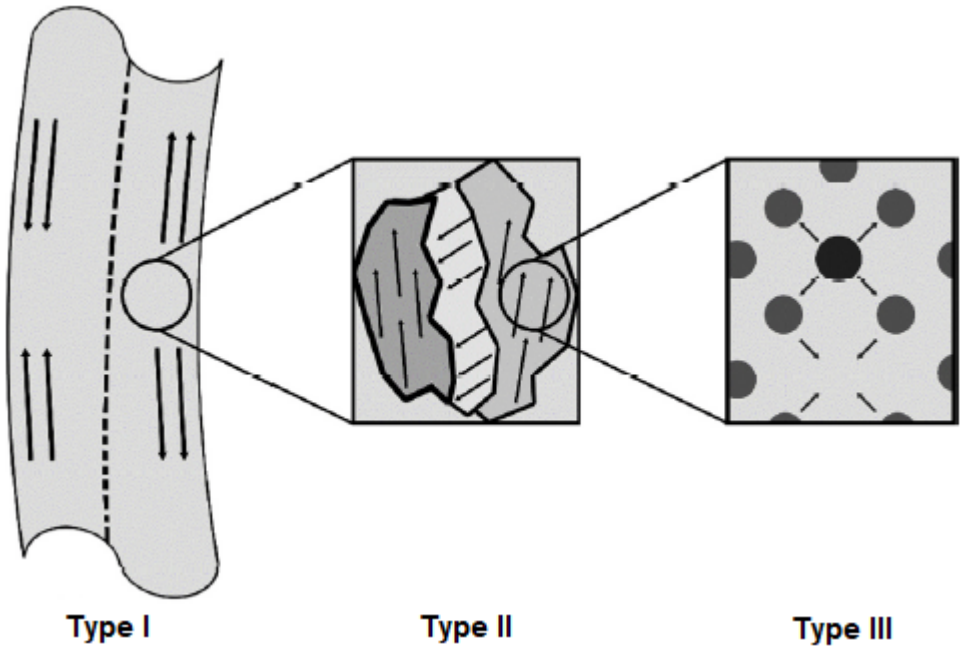

Figure 19 – Exemplification of the different size scales used to classify the residual stresses (Bartlett & Li, 2019)

the laser power (P) or using thicker layers (t). About hatching distance (h), no significant works was available in the literature, thereby the influence of that parameter is unknown. However, caution should be taken when considering these statements, as Bartlett and Li (2019) observed that for specific materials after increasing and decreasing the same LPBF parameter the behavior can be distinct.

The scan vector length can have great influence on the RS magnitude and distribution. It is known that lower scan vectors generate lower residual stresses, thus “island” or “striping” scan strategies are usually adopted instead of one step scanning, these strategies are schematized in Figure 20. By using these more complex scan strategies together with layer rotation, the resulting RS are heterogeneous, which make it harder to predict the final RS magnitude and distribution. From a one-layer point of view, the RS are two or three times higher along the scanning direction than in the transversal direction. However, when considering a part with significant height, the higher RS are expected to be present in the vertical direction (build direction) owing to the bending effect induced by the new melted material on top of the much cooler previous layers (Bartlett & Li, 2019; Deng et al., 2018; Vrancken, 2016).

Relieving RS is usually accomplished by performing post heat treatments. Specific heat treatments allow to obtain the required mechanical properties and microstructure (Tucho et al., 2017). Another technique to mitigate RS, is preheating the build chamber, thus the temperature gradient will be lower and then, lower RS are expected. This may also be important to reduce the distortions while building the part (DebRoy et al., 2018). However, sometimes RS are beneficial, it is usual to perform a mechanical surface deformation technique known as shot peening, in order to induce compressive RS on the surface of the part, as these compressive stresses will increase the resistance to crack initiation and improve the fatigue life (Vrancken, 2016).

Generally, high RS can influence the mechanical behavior in different situations, a few are explained next. Static applications with high loads may result in unexpected failure, as RS superposition with the applied stresses may overcome the yield stress of the material. RS can promote internal local defects, which are detrimental to the fatigue life of parts subjected to high number of cycles, even for small loads. If boundary conditions

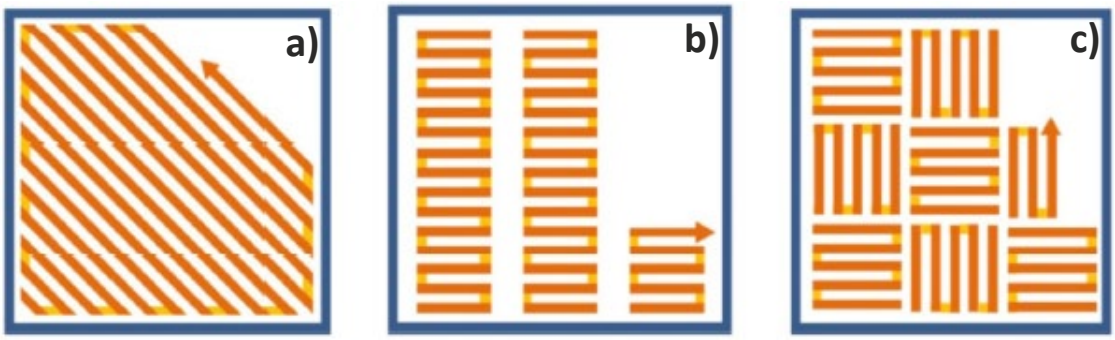

Figure 20 – Different scan strategies for LPBF: a) one step scanning; b) “striping”; and c) “island”, b) and c) have shorter scan vectors, thereby results in lower residual stresses (Qiu, Kindi, Aladawi, & Hatmi, 2018)

are changed, the RS will redistribute and self-equilibrate again, this may lead to unexpected deformations of the part. Intergranular corrosion may occur if RS of Type I and II are exposed on the surface and, thus result in stress-corrosion cracking (Vrancken, 2016).

Commonly, for PBF processed parts, tensile stresses near the surface and compressive stresses on the middle regions are expected, as it has been observed by several authors by computational models and experimental works (Bartlett & Li, 2019; DebRoy et al., 2018; Vrancken, 2016). Notwithstanding, contradictory results were obtained for a specific material, H13 tool steel, by Cottam et al. (2014) and Ghosh et al. (2007) on experimental and simulation works, respectively. The compressive stresses at the surface were attributed to the lower martensitic transformation temperature of the H13 tool steel (Vrancken, 2016).

A diversity of techniques exists and have been employed to measure the RS on LPBF fabricated parts. X-ray diffraction (XRD) (Y. Liu, Yang, & Wang, 2016; Yadroitsev & Yadroitsava, 2015) and neutron diffraction (ND) (Wu, Brown, Kumar, Gallegos, & King, 2014) are two non-destructive techniques. These diffraction techniques measure the lattice spacing using Bragg's law and compare it with the non-deformed lattice parameter. Although these techniques are the ones with better accuracy, XRD only allows measures at the surface and ND is of high complexity in order to calculate the lattice strain (Bartlett & Li, 2019; DebRoy et al., 2018).

Destructive methods such as the contour method (Vrancken, Cain, Knutsen, & Humbeeck, 2014) and hole-drilling strain-gage method (Casavola, Campanelli, & Pappalettere, 2009; Salmi & Atzeni, 2017) also have been used. The contour method requires to cut the part completely on a plane (sectioned). After the cut, the RS will redistribute to achieve static equilibrium at boundaries, which will result on in-plane deformations of the cut section. These deformations are measured and then the RS calculated (Bartlett & Li, 2019; Vrancken, 2016). Hole-drilling strain-gage method is considered a semi-destructive technique and is described in detail on the next subchapter as it is the technique used in this work to determine the RS.

2.5 HOLE-DRILLING STRAIN-GAGE METHOD

This technique is standardized by the ASTM E837 (2013) standard, which describes it as: "The hole-drilling strain-gage method determines residual stresses near the surface of an isotropic linear-elastic material. It involves attaching a strain rosette to the surface, drilling a hole at the geometric center of the rosette, and measuring the resulting relieved strains. The residual stresses within the removed material are then determined from the measured strains using a series of equations" (ASTM, 2013).

The hole-drilling strain-gage method, or just the hole-drilling method, has been used to measure RS of LPBF-ed parts by Salmi and Atzeni (2017) for AlSi10Mg, Swain et al. (2019) for Ti6Al4V and Casavola et al. (2009) for AISI Grade 18Ni300 Maraging Steel.

This technique allows to measure the in-plane strains (driven by the installed RS) near the surface of a part to a certain depth and determine by calculation the corresponding RS, even if the stresses are non-uniform along the depth (just for "thick" parts). A small hole is drilled in the center of a strain-gage, also known as rosette, which measures the relieved strains at the surface of the material (Ajovalasit et al., 2010). It is considered a semi-destructive method because many times it does not affect the structural integrity or usefulness of the part, owing to the very small hole dimensions (ASTM, 2013; Micro-Measurements, 2010).

This technique differentiates from other ones in several aspects. Any trained technician or someone with help of a guidebook can perform the tests properly. It is a very versatile method, as it can be performed on laboratory or on site, and is suitable for different sizes and shapes (Micro-Measurements, 2010). It is cost effective and standardized (Salmi & Atzeni, 2017). Although not the best in terms of accuracy, it presents reliable results if properly executed, and most important, allows to understand the RS variations until a certain depth. It is widely applied in industry to measure the RS (Ajovalasit et al., 2010).

The hole-drilling method accuracy can be affected by the mechanical properties of the material to be tested, strain-gage location and installation, drill alignment, boring process and data acquisition instrumentation (Micro-Measurements, 2010). The sensitivity of the measure decreases after a certain depth and gradually decreases. As an incremental drilling method, small depth increments are beneficial for the accuracy and the absence of noise. Also, high speed air drilling and automatic systems are recommended (Ajovalasit et al., 2010).

The material tested must have isotropic characteristics, also the Young's modulus and Poisson's ration must be well known. When possible, the required material properties must be experimentally determined to obtain more accurate results, mainly for non-standard materials. The surface place where the measure will be performed must be flat and away from geometric or material discontinuities. Moreover, the drill must be perfectly centered with the rosette. The rosette can have diverse configurations, usually with 3 (Type A and B) or 6 (Type C) individual strain-gages, as exemplified on the Figure 21. The selection of the rosette depends on the material, size, location and required thermal stability. The rosette type will influence the hole dimensions and the sensitivity of the strain measures (ASTM, 2013).

The rosette must be fixed on the part surface with a cyanoacrylate-based adhesive. To guarantee a perfect bonding, and thereby perfect measurements, the surface must be

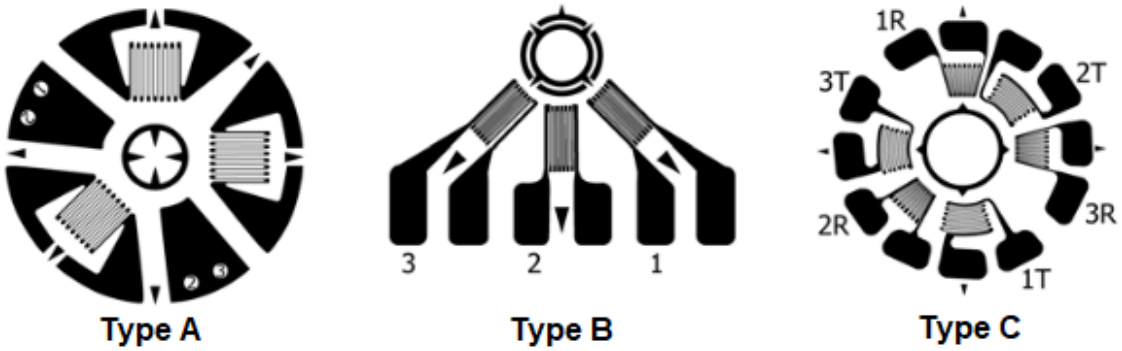

Figure 21 – Standardized rosette configurations for the hole-drilling strain-gage method (ASTM, 2013)

properly prepared previously. Oxides, paint and rust must be removed, and rough surface must be avoided. Although the surface abrasion techniques should be avoided in order not to change the surface RS condition, they can be slightly used to improve the roughness of the surface (Ajovalasit et al., 2010; Micro-Measurements, 2010).

In order to centralize the drill with the rosette, systems incorporating microscopes or optical systems exist (Ajovalasit et al., 2010). The drill selection must be done carefully. Carbide "inverted cone" dental burs or small endmills, with a taper angle lower than 5°, are recommended by the ASTM E837 standard for most of the materials (ASTM, 2013). The fillet radius produced at the bottom of the hole may have significant influence on the measures. Larger radius may result in higher detrimental effects. Also, it is recommended to not perform holes next to others, the minimum distance is six times the diameter of the drill (Ajovalasit et al., 2010).

A counterclockwise type B rosette was used. A schematic view of this type of rosette is shown in Figure 22. From left to right can be identified the individual strain-gages A, B and C. The maximum stress (σ_{max}), minimum stress (σ_{min}) and the direction (β) are also represented. σ_{max} is the maximum principal stress, which correspond to the higher tensile stress or in case of compressive stresses, the lower compressive stress. Similarly, σ_{min}, the minimum principal stress, corresponds to the lower tensile stress or higher compressive stress. β is the angle that permits to identify the direction of σ_{max}, which is always determined from the center alignment of the strain-gage A. β can vary from -90° to 0° if the maximum principal stress is directed clockwise to the strain-gage A or from 0° to 90° if it is directed counterclockwise (ASTM, 2013; SINT Technology, n.d.-b).

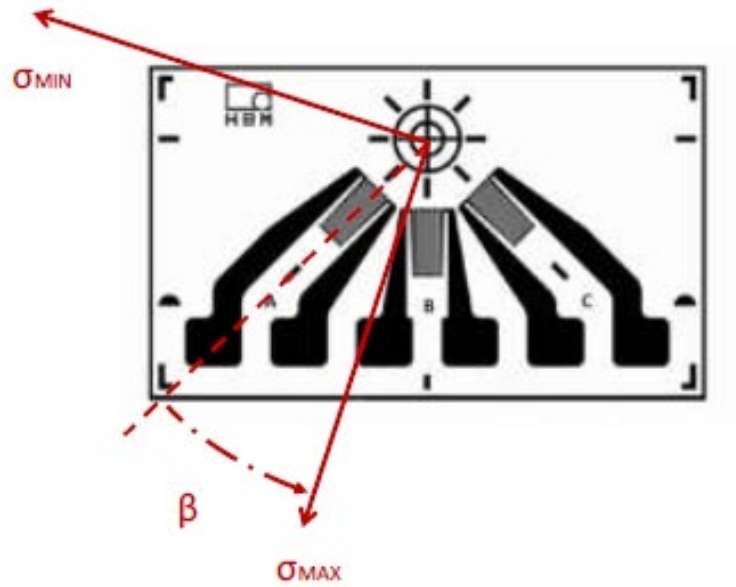

Figure 22 – Scheme of a counterclockwise type B rosette for hole-drilling strain-gage method

MATERIALS AND METHODS

3 MATERIALS AND METHODS

3.1 POWDER - FEEDSTOCK

The powder utilized in the LPBF process to produce the specimens analyzed in this work was the EOS NickelAlloy IN718 powder from EOS GmbH (Germany). The expected chemical composition of parts built with this material, in accordance with the ASTM F3055 (2014) standard, is presented in Table 5. ASTM F3055 (2014) standard covers the specifications for LPBF of IN718 (UNS N07718) parts.

Table 5 – Chemical composition of parts built with powder EOS NickelAlloy IN718 (EOS, 2014)

Material	Weight [%]
Ni	50.00 – 55.00
Cr	17.00 – 21.00
Nb	4.75 – 5.50
Mo	2.80 – 3.30
Ti	0.65 – 1.15
Al	0.20 – 0.80
Co	≤ 1.00
Cu	≤ 0.30
C	≤ 0.08
Si, Mn	≤ 0.35 (each)
P, S	≤ 0.015 (each)
B	≤ 0.006
Fe	balance

Using optimized process parameters, a minimum density of 8.15 g/cm^3 and a relative density of approximately 100% is achievable (EOS, 2014). The theoretical density of IN718 material is of 8.19 g/cm^3. EOS GmbH (Germany) is a company experienced in manufacturing and selling a variety of AM systems. In addition, they developed powders fully dedicated to use in AM systems and commercialize them.

In the EOS NickelAlloy IN718 data sheet, typical mechanical properties of parts produced by LPBF with that powder are presented under different conditions (as-built and after heat treatments) and dependent on the part orientation (H for scanning direction, horizontal, and V for build direction, vertical). The properties were obtained from parts built with optimized process parameters and EOS GmbH (Germany) AM machines, these values are not enough to use as a basis for projecting new parts (EOS, 2014). Table 6 summarizes these properties at room temperature (20°C). The different heat treatments are the following: HT1, SA plus DA per AMS 5662 (SAE, 2016); and HT2, SA, per AMS

5664 (SAE, 2017), plus DA at 760°C for 10h, FC to 650°C in 2h, and hold at this temperature for 8h, followed by AC.

Table 6 – Typical mechanical properties of parts manufactured using EOS GmbH (Germany) technology, powder and machines (EOS, 2014)

Property	Orientation	As-built	HT1	HT2
Young's modulus [GPa]	H	160 ± 20	-	-
	V	-	170 ± 20	170 ± 20
Yield strength [MPa] (Rp 0.2%)	H	780 ± 50	-	-
	V	634 ± 50	1150 ± 100	1240 ± 100
Tensile strength [MPa]	H	1060 ± 50	-	-
	V	980 ± 50	1400 ± 100	1380 ± 100
Elongation at break [%]	H	27 ± 5	-	-
	V	31 ± 5	15 ± 3	18 ± 5
Hardness	-	30 HRC 287 HB	47 HRC 446 HB	43 HRC 400 HB

The IN718 powder utilized in this work was analyzed by Mostafa et al. (2017). With an average particle size of 30 µm, EOS NickelAlloy IN718 powder particles have a spherical-like shape, as observed in the image obtained by Scanning Electron Microscopy (SEM) shown in Figure 23.a. A few powder particles have an irregular shape, owing to the powder manufacturing process, gas atomization, as also reported by Parimi et al. (2014). During the gas atomization process, partially melted small particles, designated as "satellites", get attached to the larger ones forming these irregular shapes, as shown in detail in Figure 23.b. In addition to, by X-Ray Diffraction (XRD) analysis of a powder particle cross-section, Mostafa et al. (2017) reported that ɣ' phase, carbides and Laves phase were not found.

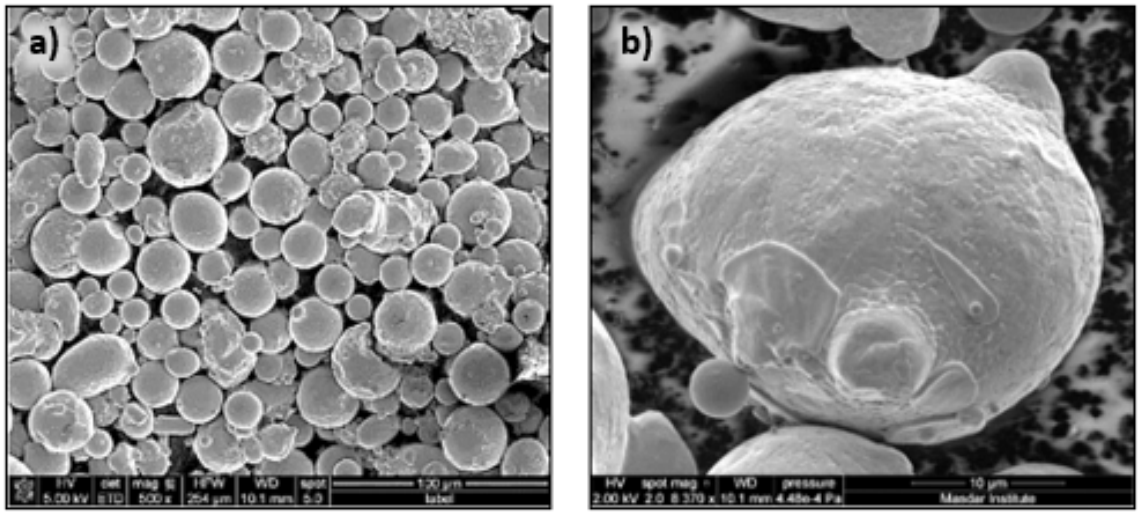

Figure 23 - SEM images of the EOS NickelAlloy IN718 powder: a) range of particles size and typical shape; and b) magnified particle with irregular shape (Mostafa et al., 2017)

3.2 LASER POWDER BED FUSION EQUIPMENT

The LPBF machine utilized to produce the specimens was a Mlab Cusing R from Concept Laser GmbH (Germany) (2018), as the one shown in Figure 24, equipped with a 100 W Fiber laser (continuous wave). This machine is capable of building fully dense parts with great surface finish with both reactive and non-reactive materials. It has a modular structure to allow flexibility in the build sizes and quick material changes. The available build envelops are 50 x 50 x 80 mm, 70 x 70 x 80 and 90 x 90 x 80 (x, y, z). Moreover, it comes with a semi-automatic sieving station to facilitate powder reusability ("GE Additive machines," n.d.).

Figure 24 – Mlab Cusing R machine from Concept Laser GmbH (Germany) ("GE Additive machines," n.d.)

The Mladb Cusing R machine can produce a layer thickness of 15 – 30 µm with a maximum scanning speed of 7 m/s. Depending on the material, the production rate can vary between 1 to 5 cm^3 per hour. The inert gas utilized can be Nitrogen or Argon, and the gas consumption during the building process is approximately 0.6 – 0.8 l/min. The room temperature must be between 15 and 35°C during the operation for quality assurance (Concept Laser, 2018).

A constant flow of Argon was used to protect the build atmosphere and no chamber or substrate preheating was adopted. Right after removing the substrate from the machine no post treatments were performed on the substrate or specimens.

3.3 SCANNING STRATEGY

The scanning strategy adopted consists of rotating the scan vectors 67° between layers and "striping" with 5 mm stripe width (see Figure 20 to observe the difference to other scan strategies). Figure 25 illustrates the scan strategy: N is the first layer and N + 1 the subsequent, rotated 67°; the yellow lines represent the "striping", the distance between each yellow line correspond to the stripe width; the blue arrows represent the scan

vectors, which are continuous in a zigzag movement till the end of the stripe; and, the red arrows correspond to the scanning direction along the stripes, after finishing the first stripe the laser moves to the start of the next stripe.

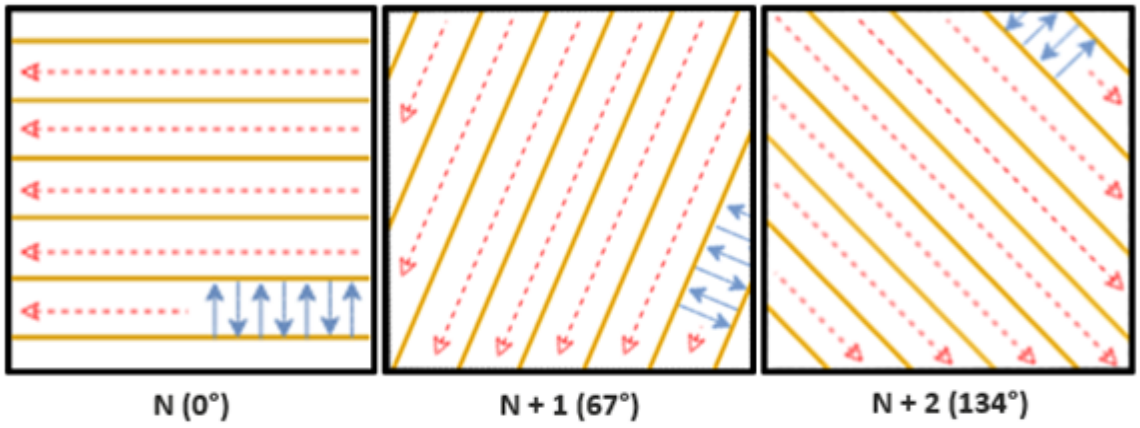

Figure 25 – Illustration of the scan strategy adopted: 67° rotation and "striping" (rough example)

3.4 ADDITIONAL EQUIPMENTS AND METHODS

In this subsection are reported the additional equipments and respective methods required to achieve the results presented in this work.

3.4.1 WIRE ELECTRICAL DISCHARGE MACHINE

The specimens were removed from the substrate by wire electrical discharge machining (W-EDM). The equipment used was a CNC Wire Cut EDM DK7732 from Suzhou Baoma Numerical Control Equipment (China). This machine uses molybdenum wire and has a precision of 0.015 mm. The fixing table can travel 320 mm (x-axis) and 400 (y-axis) and can withstand a maximum load of 400 Kg. The wire speed can range from 5 to 11 m/min achieving a maximum cutting speed of 150 mm^2/min ("CNC Wire Cut EDM," n.d.).

3.4.2 ANALYTICAL BALANCE

A high precision analytical balance from ORMA (Italy) was used to measure the specimens weight for the optimal process parameters selection. It has a sensitivity of 0.0001g (0.1 mg) and a pan size with a diameter of 80 mm ("ANALYTICAL BCA SERIES," n.d.).

3.4.3 HOT MOUNTING PRESS

In order to help the handling of small specimens, those were mounted in a transparent acrylic resin. The equipment used to mount the specimens was an IPA 30 hot mounting press from Remet (Italy). It has a mounting diameter of 30 mm and reaches a

temperature of 200°C ("IPA 30/40," n.d.). A hot resin powder ("Transparent Clear Acrylic resin," n.d.) from PRESI (France) was used as the mounting material.

3.4.4 POLISHING

A semi-automatic polishing machine was used to polish the surfaces of the specimens. Sandpaper with different grits and diamond paste were used. During the polishing with sandpaper a constant flow of tap water was used to cooldown the specimens and remove particles.

Specimens for the Archimedes' method were polished with sandpaper from 320, 500, 800 to 2000-grit. For micrograph-based method, same sandpaper grits were used plus a 4000-grit sandpaper and diamond paste with 3 µm and 1 µm. Specimens for the RS analysis were manually and slowly polished with 200 and 400-grit sandpaper.

3.4.5 FURNACE

The heat treatments were carried out in a P330 Horizontal Tube Furnace from Nabertherm (Germany). It reaches a temperature of 1500°C and has a temperature control accuracy of ±1°C. The maximum capacity is 79 mm in diameter and 1070 mm in length ("Nabertherm RHTC," n.d.).

3.4.6 CUTTING MACHINE

Some specimens were sectioned after the RS measurements for microstructure analysis. The cut was made in an IsoMet 4000 Linear Precision Saw from Buehler (Germany). It enables cuts with minimal specimen deformation and low kerf loss. The feed rate can vary from 1.2 to 19 mm/min and the rotation speed from 200 to 5000 rpm ("IsoMet™ 4000," n.d.). As a cutting tool was used a resinoid cut-off wheels type AO from PRESI (France) with a diameter of 125 mm and a thickness of 0.5 mm ("Resinoid cut-off wheels," n.d.).

3.4.7 SCANNING ELECTRON MICROSCOPE

The magnified images for microstructure analysis were obtained on a Phenom XL Desktop SEM from Thermo Fisher Scientific (USA). It is a compact desktop equipment that allows analysis of specimens with dimensions up to 100 x 100 x 65 mm. The light optical magnification has a range of 3 – 16x, the electron optical magnification of 80 – 100000x and a maximum digital zoom of 12x. The resolution is of 14 nm or lower. This equipment also comprises energy-dispersive X-Ray spectroscopy (EDS) and Electron backscatter diffraction (EBSD) analysis methods ("Phenom XL," n.d.).

3.4.8 HOLE-DRILLING STRAIN-GAGE METHOD EQUIPMENT

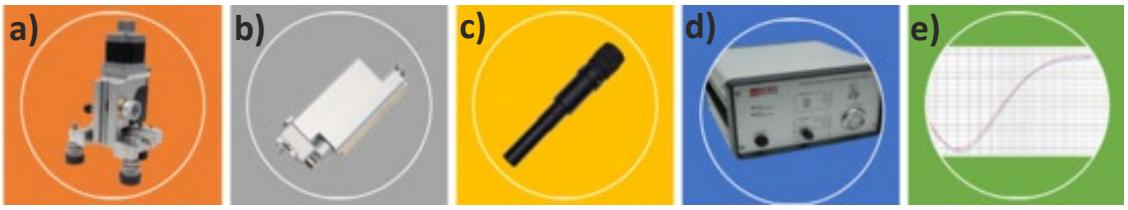

Figure 26 – Technology provided by SINT Technology (Italy): a) mechanical device; b) drill slider; c) centering device; d) electronic device; and e) residual stresses software ("Restan MTS3000," n.d.)

SINT Technology (Italy) offers a dedicated system to automatically perform this method, the MTS3000 – RESTAN (Residual Stress Analyzer). As shown in Figure 26, it comprises the mechanical device with the drilling slider, which holds the drill and the centering device, the accessories, such as the electronic device and strain gage amplifiers, and useful software.

SINT RSM software was used to automatically perform the tests, as it controls the drill movements and acquire the data. SINT EVAL software was used to process the data and evaluate the RS, it allows to choose different calculation methods to transform the measured strain values into RS values (SINT Technology, n.d.-a). This technology for hole-drilling strain-gage method from SINT Technology (Italy) was used to carry out the RS tests on the specimens.

THESIS DEVELOPMENT

4.1 OPTIMAL PROCESS PARAMETERS SELECTION

4.2 RESIDUAL STRESS ANALYSIS

4 THESIS DEVELOPMENT

4.1 OPTIMAL PROCESS PARAMETERS SELECTION

It was the first time, in-house, using IN718 material on the Mlab Cusing R machine, thereby it was needed to select the optimal process parameters. The methodology to choose the best process parameters was based, firstly, on the internal porosity of the specimens and the existence of cracks. Then, in cases of similar lowest porosity percentages, factors such as low VED and pores dimensions and shape were taken in consideration.

A total of 18 cubic specimens (1 cm^3) were built with different process parameters combinations. From the volumetric energy density equation *(2.3)*, the laser power and layer thickness were kept constant to all the specimens, 95 W and 20 µm, respectively. Only scanning speed and hatching distance were varied, resulting on different VED. Scanning speeds on a range of 100 to 800 mm/s and hatching distances from 0.05 to 0.15 mm were considered. The process parameters for every specimen are presented in Table 7.

Table 7 - Process parameters of each specimen for optimal process parameters selection

Spec.	P [W]	t [mm]	v [mm/s]	h [mm]	VED [J/mm³]
1	95	0.02	100	0.15	317
2	95	0.02	200	0.09	264
3	95	0.02	200	0.11	216
4	95	0.02	200	0.13	183
5	95	0.02	200	0.15	158
6	95	0.02	400	0.05	238
7	95	0.02	400	0.07	170
8	95	0.02	400	0.09	132
9	95	0.02	400	0.11	108
10	95	0.02	400	0.13	91
11	95	0.02	400	0.15	79
12	95	0.02	600	0.05	158
13	95	0.02	600	0.07	113
14	95	0.02	600	0.09	88
15	95	0.02	600	0.11	72
16	95	0.02	800	0.05	119
17	95	0.02	800	0.07	85
18	95	0.02	800	0.09	66

The porosity percentages were determined by two distinct methods, discussed on the bibliographic work (subchapter 2.4.2). Those are the Archimedes' and micrograph-based methods.

4.1.1 ARCHIMEDES' METHOD RESULTS

ASTM B311 (2017) standard was used to determine the specimens density by the Archimedes' method. This standard is recommended for materials with less than 2% porosity, which is suitable for LPBF-ed parts (nearly 100% density). After cutting the samples by W-EDM the surfaces were polished to reduce the roughness and avoid adhesion of air bubbles.

In Figure 27.a is shown the analytical balance used. For all specimens, three measures were performed in air and in water (Figure 27.b), then the average mass in air (m_a) and mass in water (m_w) values were calculated. Using the equation *(2.1)* the volumetric mass density (ρ) for each specimen was calculated, the value used for density of water in accordance with the room temperate (20°C) was 0.9982 g/cm^3 (Annex 1). Then, the porosity was determined by the equation *(*4.1*)*, using 8.15 g/cm^3 for the IN718 density (ρ_{IN718}) (EOS, 2014).

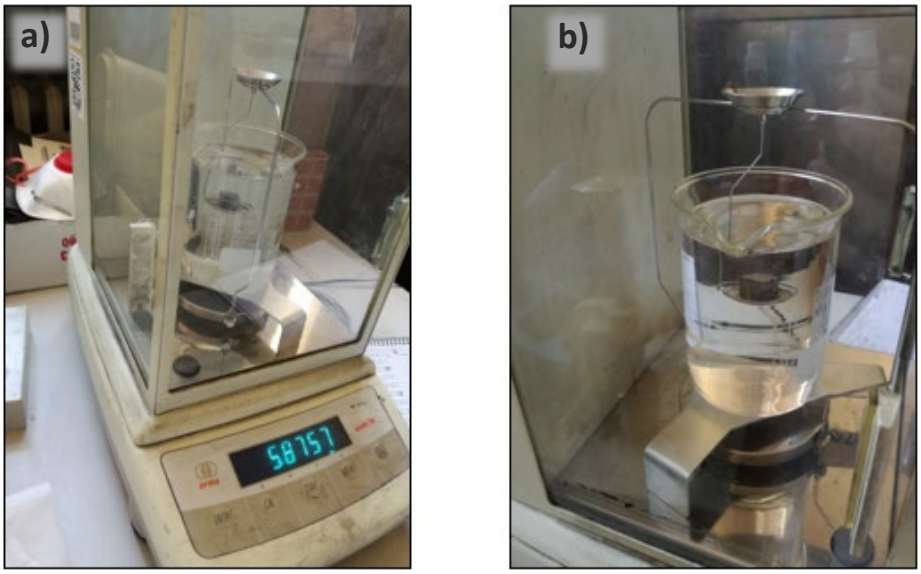

Figure 27 – Archimedes' method mass measurement: a) analytical balance; and, b) measurement in water

$$Porosity\ \% = 1 - \frac{\rho}{\rho_{IN718}} \qquad (4.1)$$

The average mass measurements (in air and in water), volumetric mass density and porosity percentage calculated are presented in Table 8 for each specimen. In Annex 2 are shown the values corresponding to every single measurement (three measurements per specimen).

Table 8 – Archimedes' method: average mass (m_a) in air and mass in water (m_w), volumetric mass density (ρ) and porosity percentage for every specimen

Spec.	m_a [g]	m_w [g]	ρ [g/cm³]	Porosity [%]
1	6.623	5.758	7.693	5.61%
2	6.647	5.791	7.764	4.74%
3	6.725	5.863	7.796	4.34%
4	6.853	5.988	7.948	2.48%
5	6.543	5.706	7.846	3.73%
6	6.823	5.966	7.981	2.08%
7	6.847	5.995	8.043	1.31%
8	6.722	5.878	7.978	2.11%
9	6.724	5.886	8.044	1.30%
10	6.743	5.902	8.041	1.34%
11	6.729	5.893	8.067	1.01%
12	6.748	5.914	8.052	1.20%
13	6.798	5.961	8.119	0.37%
14	6.795	5.957	8.108	0.52%
15	6.737	5.906	8.126	0.30%
16	6.818	5.975	8.117	0.40%
17	6.811	5.972	8.098	0.64%
18	6.760	5.923	8.094	0.68%

4.1.2 MICROGRAPH-BASED METHOD RESULTS

Despite the fact it is not a standardized method, the micrograph-based method is very intuitive. After performing the Archimedes' method all the specimens were cut in half (sectioned) by W-EDM along the build direction (vertically). Then, the cross-sections of all specimens were polished.

After performing the polishing, the cross-sections were observed on an optical microscope at a 100x magnification. At this magnification, the open pores (sectioned pores) on the surface are clearly observable. Also, cracks, dirt and scratches are detectable, those must be ignored when analyzing the porosity (cracks must be taken in consideration for the final conclusions). One surface per specimen was analyzed, collecting ten images at different locations for every specimen. Figure 28.a illustrates the arbitrated scheme for collecting the ten images at the cross-section, the arrow indicates the build direction.

As an example, Figure 28.b shows the image acquired from the optical microscope of the specimen number 13 at the position one, where are observed the pores of different

sizes and the tracks of dirt resultant from the polishing orientation. All the optical microscopy images acquired for each specimen are available in Annex 3.

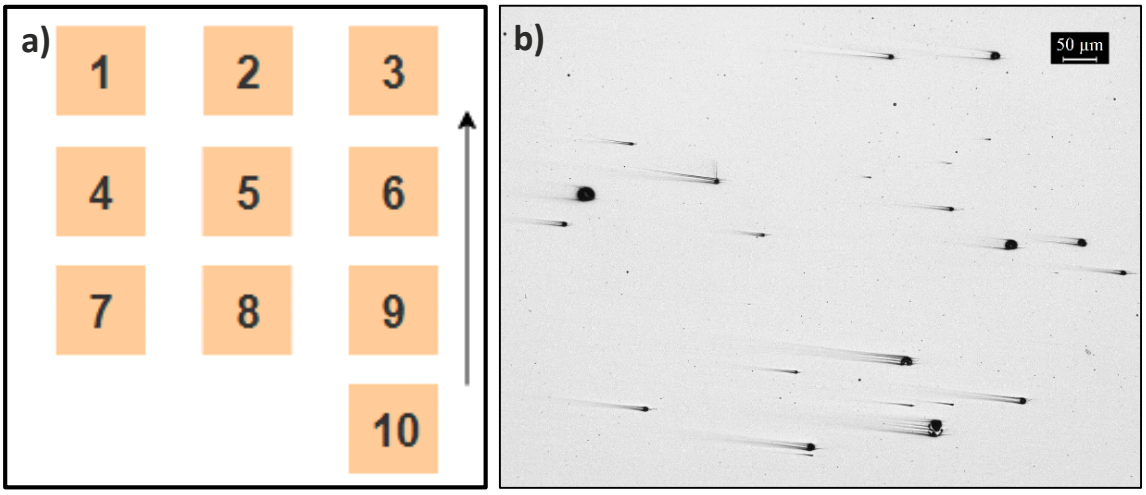

Figure 28 – Micrograph-based method: a) scheme for optical microscopy images collecting; and, b) image acquired from specimen 13 cross-section at the position one

An open source image processing software named ImageJ was used to process the acquired images. Image thresholding (see Figure 29.a) was applied to turn all the images black and white and remove the tracks of dirt (see Figure 29.b). These and other imperfections detected as noun pores were removed posteriorly in order to keep only as black color the area corresponding to porosity.

Then, yet with the aid of the image software, the percentage of the black fulfilled area was determined for each single image, which corresponds to the percentage of porosity present on that image. All the single values obtained are displayed in Annex 4. Table 9 presents the average porosity and the standard deviation for all the 18 specimens after the ten measurements per specimen. As complementary information, it was also measured the largest dimension of the largest pore of every specimen and determined the characteristic shape of the pores, also presented in Table 9.

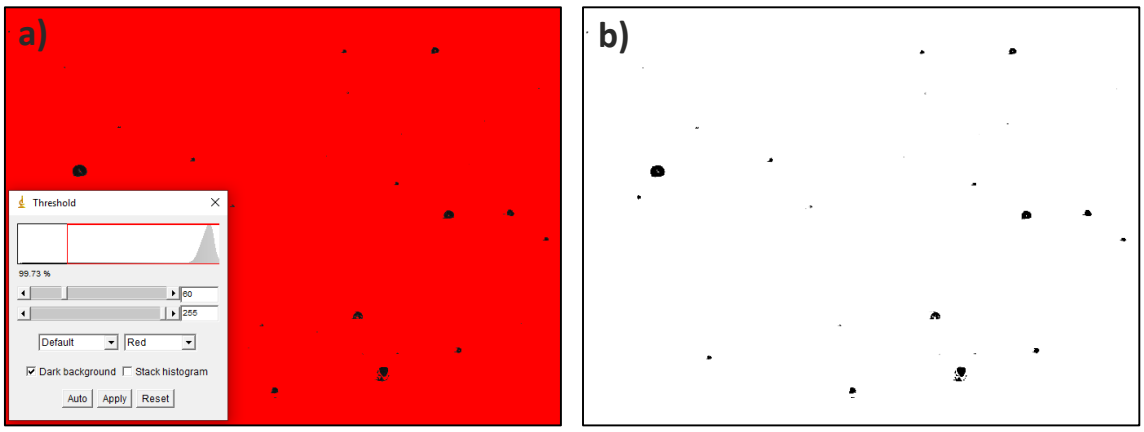

Figure 29 – Micrograph-based method: a) image thresholding; and, b) processed image with black spots corresponding to porosity

Table 9 – Micrograph-based method: average porosity, standard deviation, largest pore dimension and typical shape

Spec.	Porosity [%]	SD [%]	Largest pore [mm]	Shape
1	7.013	0.610	108.09	Irregular
2	4.672	0.966	86.32	Irregular
3	4.179	0.813	75.67	Irregular
4	3.988	0.911	80.29	Irregular
5	4.845	0.857	82.01	Irregular
6	3.446	0.454	68.91	Spherical-like*
7	2.420	0.508	58.74	Spherical-like*
8	2.528	0.432	58.59	Spherical-like*
9	1.777	0.392	58.33	Spherical-like*
10	1.466	0.207	51.93	Spherical-like*
11	5.711	1.306	82.37	Irregular
12	0.410	0.226	62.24	Spherical-like
13	0.254	0.152	36.14	Spherical-like**
14	0.263	0.136	52.38	Spherical-like
15	0.284	0.103	53.49	Spherical-like**
16	0.139	0.073	37.17	Spherical-like
17	0.174	0.130	38.83	Spherical-like
18	0.223	0.133	40.25	Spherical-like

* A few irregular shaped pores also observed

** A few powder particles were observed (powder particles not melted during the building process)

4.1.3 DISCUSSION

To choose the optimal process parameters, two distinct methods were used to determine the porosity percentage of 18 specimens build with different combinations of process parameters. Also, the influence on the porosity of the process parameters that were modified between the combinations (scanning speed, hatching distance and VED) were studied.

A big crack was observed on the cross-section of the specimen 12 (see Figure 30.a), thereby this is a reason to not consider this set of parameters. However, it was considered for the study of the parameters influence on the porosity, avoiding the area adjacent to the crack.

The graph of Figure 31 compares the porosity values determined by the Archimedes' and micrograph-based methods. A significant discrepancy in the porosity percentage was observed in the specimen 11, however, after observing all the ten images acquired from specimen 11 cross-section they are all similar to the one shown in Figure 30.b,

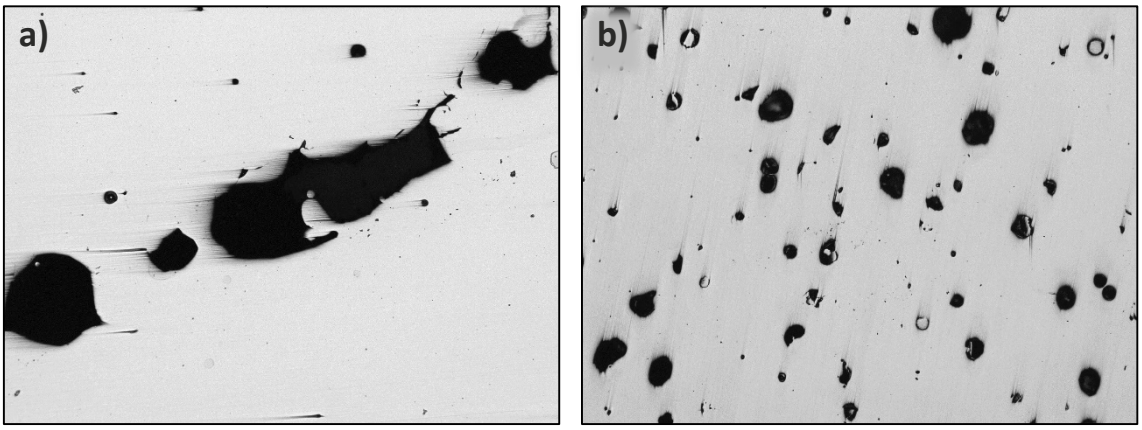

Figure 30 – Optical microscopy images: a) specimen 12, big crack detected; and, b) specimen 11, distribution of large pores observed

indicating high internal porosity (Archimedes' method failed to determine the porosity percentage on this specimen).

Was also observed that for higher porosity percentages, the Archimedes' method tends to show lower values than the other method. For values near 100% density, the opposite was observed at a smaller scale. These discrepancies may be related to the fact that the micrograph-based method is a very localized method, this is, if the cross section or the acquired images were at different locations the results could be different. However, this method allows to have a visual conclusion of the real porosity condition.

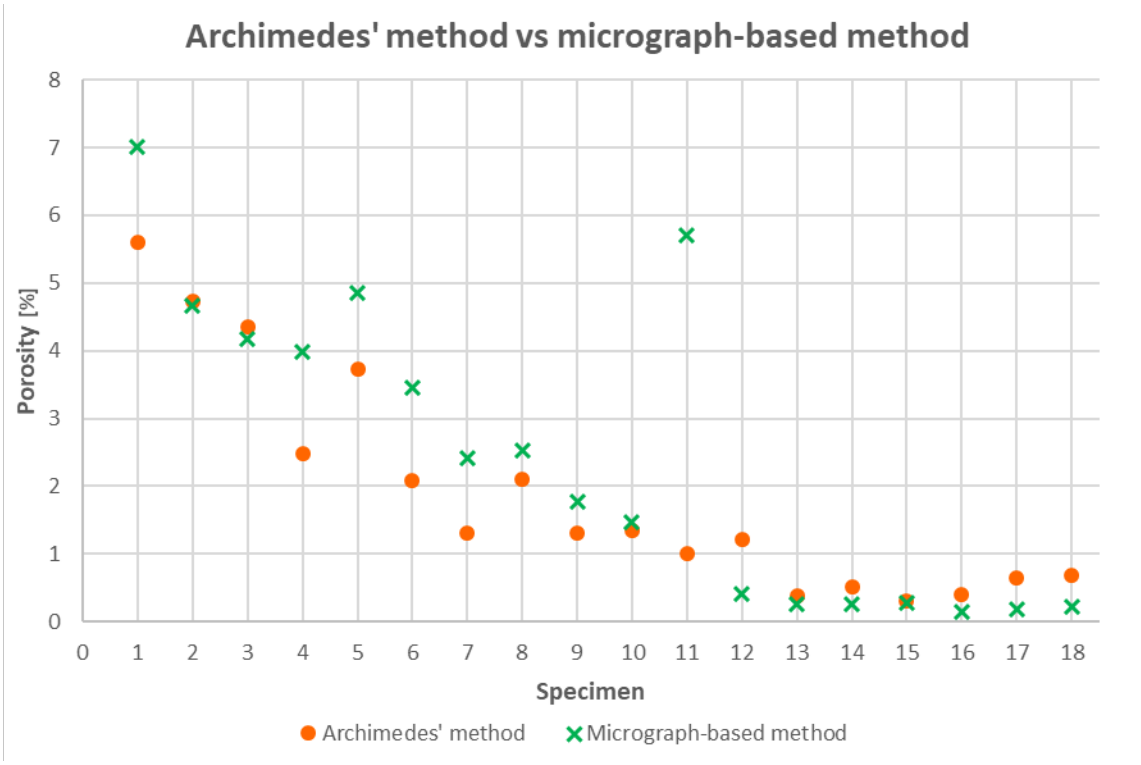

Figure 31 – Graph of the porosity percentage determined by the Archimedes' and micrograph-based methods

As for lower porosity specimens (specimens 12 to 18) the micrograph-based method determined lower percentage values than the Archimedes' method (see Table 9 and Table 8, respectively), the micrograph-based method results were taken into consideration to choose the specimen with lowest porosity.

From Figure 31 graph, the specimen with lower porosity is the 16, with 0.139% porosity and 0.073% standard deviation (lowest among all). Also, from Table 9 can be concluded that the dimension of the largest pore of the specimen 16 is among the smallest ones between all the specimens, with 37.17 mm and the pores are typically spherical-like shaped. Thereby, gathering all these conclusions, the set of process parameters selected as optimal was the one from specimen 16. This set of parameters corresponds to a laser power of 95 W, a layer thickness of 20 µm, a scanning speed of 800 mm/s and a hatching distance of 0.05 mm.

To study the effect of the process parameters on the porosity of LPBF-ed IN718 specimens a few graphs were made, the porosity percentages used correspond to the micrograph-based method. VED is obtained by four parameters that can be varied independently, thereby the VED effect on the porosity can be resultant from any of the individual parameters and not of the VED itself.

From Figure 32 graph it can be observed that higher VED resulted on high porosity. However, it can also be related to the scanning speed parameter, as increasing the scanning speed originated lower porosity. It was noticed that for 100, 200, 400 and 600 mm/s scanning speeds the porosity values decreased gradually, respectively, and for

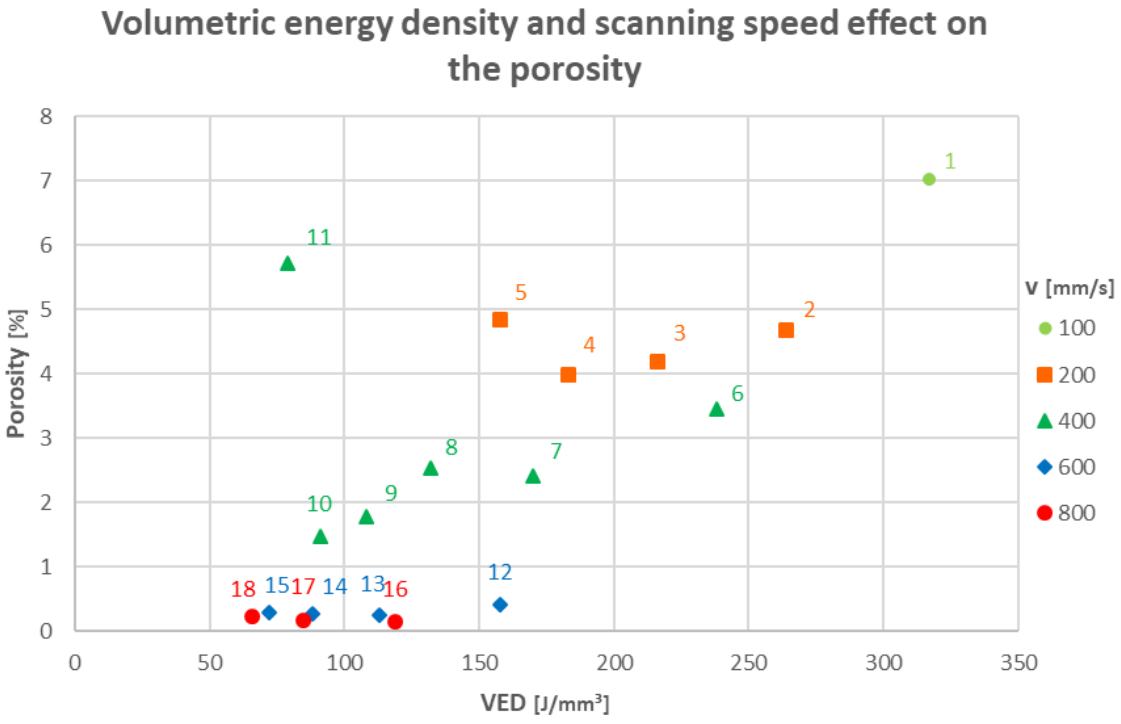

Figure 32 – Graph of the volumetric energy density and scanning speed effect on the porosity

600 and 800 mm/s speeds the difference in the porosity percentage is not significant (see also Figure 33). For scanning speeds of 600 and 800 mm/s, the measured porosity corresponds to the commonly reported values for LPBF processes, nearly 100% density.

From this work it was not possible to state the effect of the VED on the porosity. In Figure 32 graph, only specimens built with a scanning speed of 400 mm/s had a porosity descendent trend with the decreasing of the VED (specimen 11 out of this trend).

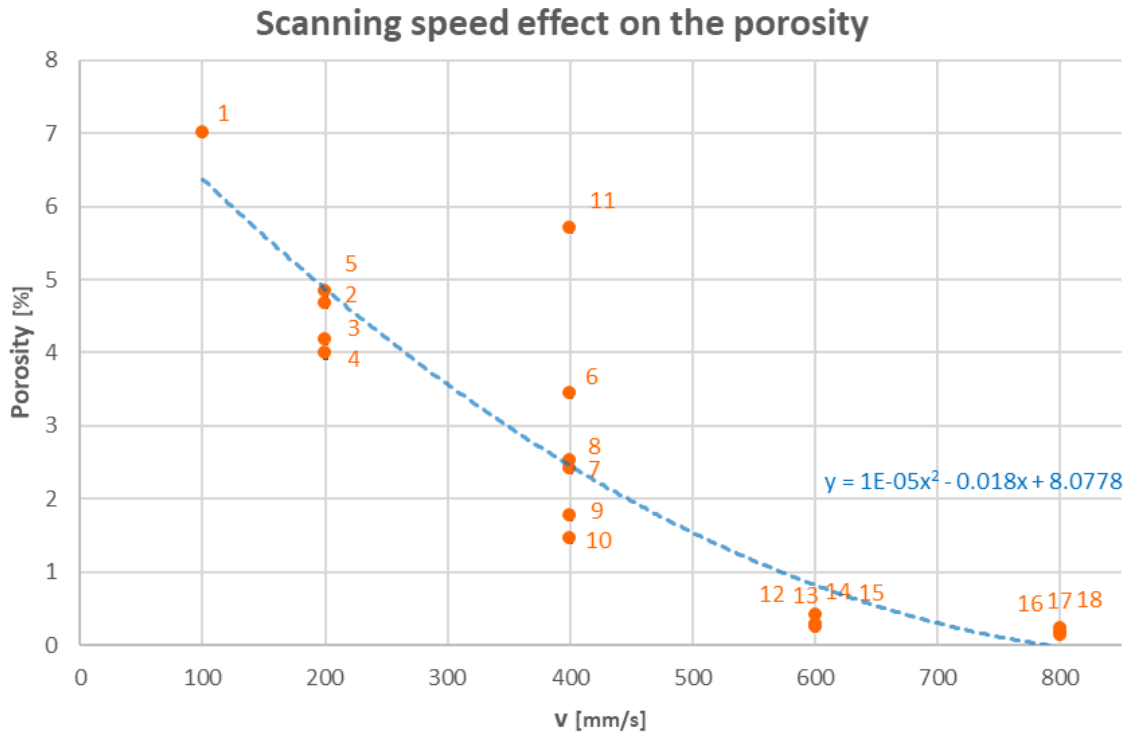

Figure 33 – Graph of the scanning speed effect on the porosity (polynomial trend line)

The effect of the hatching distance on the porosity is shown in Figure 34. Analyzing the scanning speeds 200 and 400 mm/s it was observed that from 0.05 to 0.13 mm hatching distance the porosity follows a descending trend. For a hatching distance of 0.15 mm, were obtained the highest porosity percentages independently of the scanning speed. This may suggest that the optimal hatching distance is for the conditions present in this work is 0.13 mm, however, only two specimens were produced with this hatching distance.

Up until now no reasons were noted to explain the large porosity of the specimen 11 that is substantially distinct from the others built with 400 mm/s scanning speed (see the points marked with triangles in Figure 34). One possible explanation is the 0.15 mm hatching distance, which may be excessive in order to complement with the other parameters. The optimal hatching distance depends on the laser beam diameter, for example, if the hatching distance is excessive the heat of the laser beam will not be able

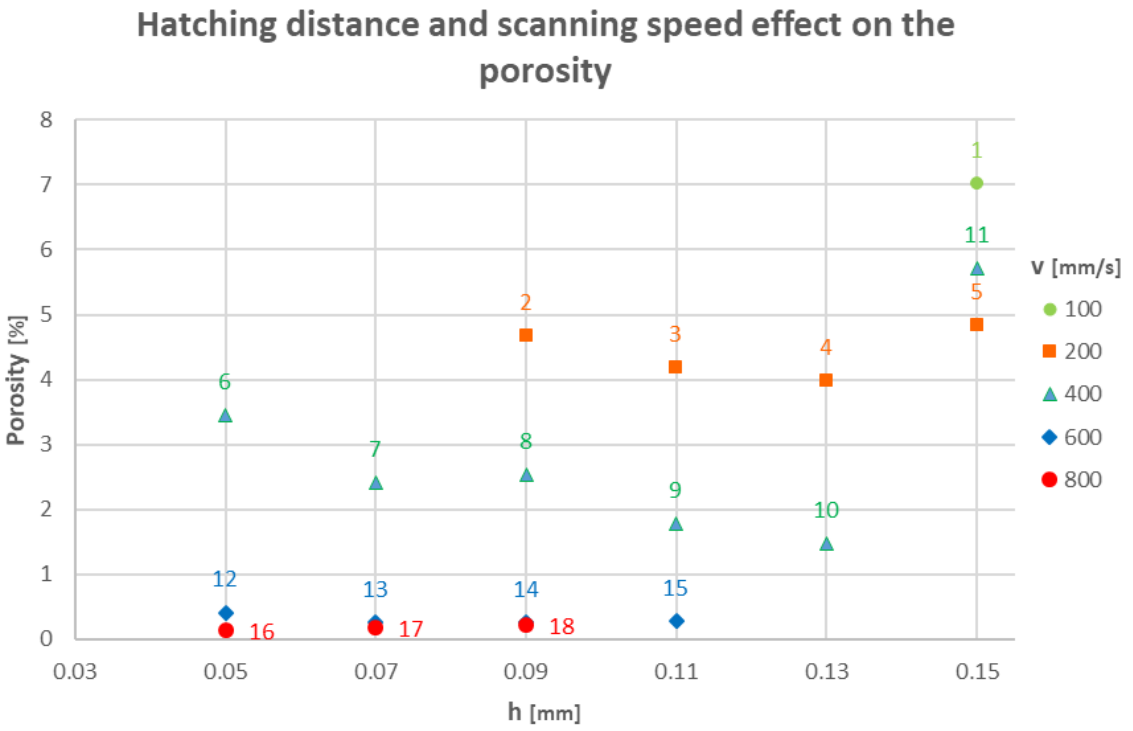

Figure 34 – Graph of the hatching distance and scanning speed effect on the porosity

to reach the previous adjacent melted track and lack of fusion or great porosity is susceptible to occur at the melting pool boundaries.

The dimension of the largest pore was also analyzed. In Figure 35.a graph it is seen that the specimens with larger pores also have higher porosity, which was expected as large pores represents a higher area free of material and, although in the graph only is presented the dimension of the largest pore, usually, other similar pores with identical dimension were found at random locations.

It was also noticed from Figure 35.a graph that the typical shape of the pores is related with the dimension. For specimens with higher dimension of the largest pore, a lot of irregular shaped pores were found and of great size. A few irregular pores and an abundance of spherical-like shaped pores were found in specimens with medium dimensions of the largest pore around 60 µm and slightly significant porosity. For specimens with lower dimension of the largest pore, the predominance of the pores was spherical-like and the quantity decreased greatly.

In the graph of Figure 35.b is shown the influence of the scanning speed on the formation of the pores. From that graph it was noticed a trend. With the increase of the scanning speed the dimension of the largest pore tends to decrease. It is also observed from a different perspective the relation between the dimension of the largest pore and the typical pore shape.

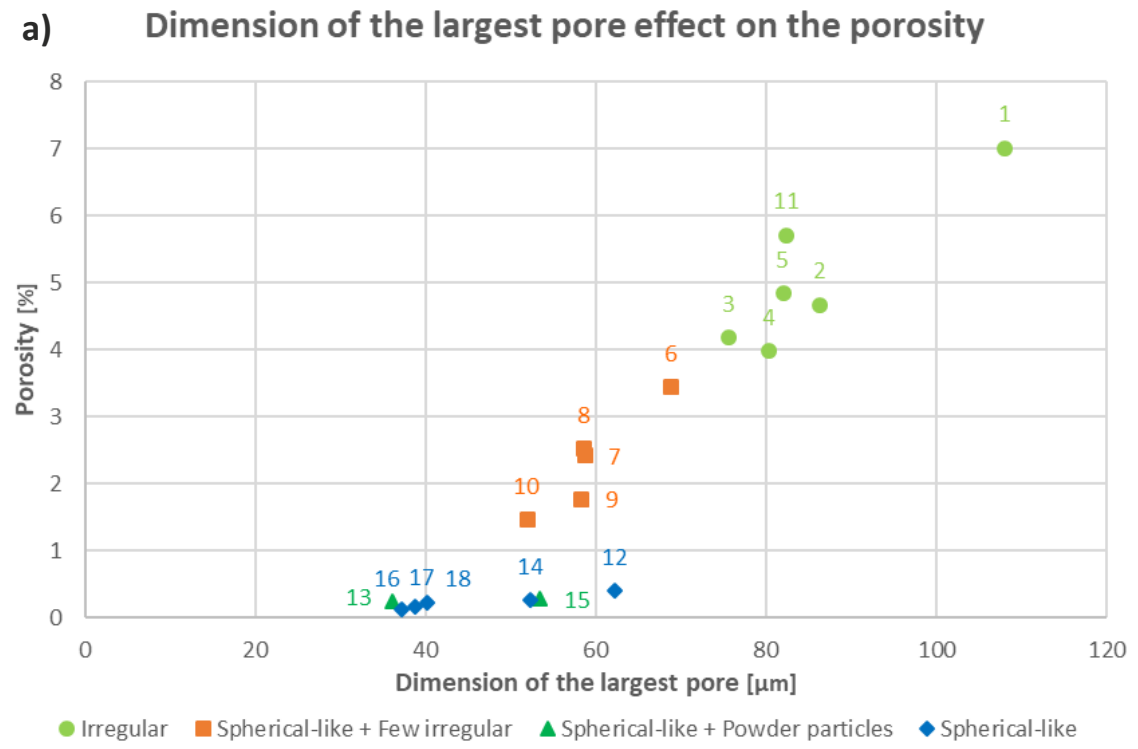

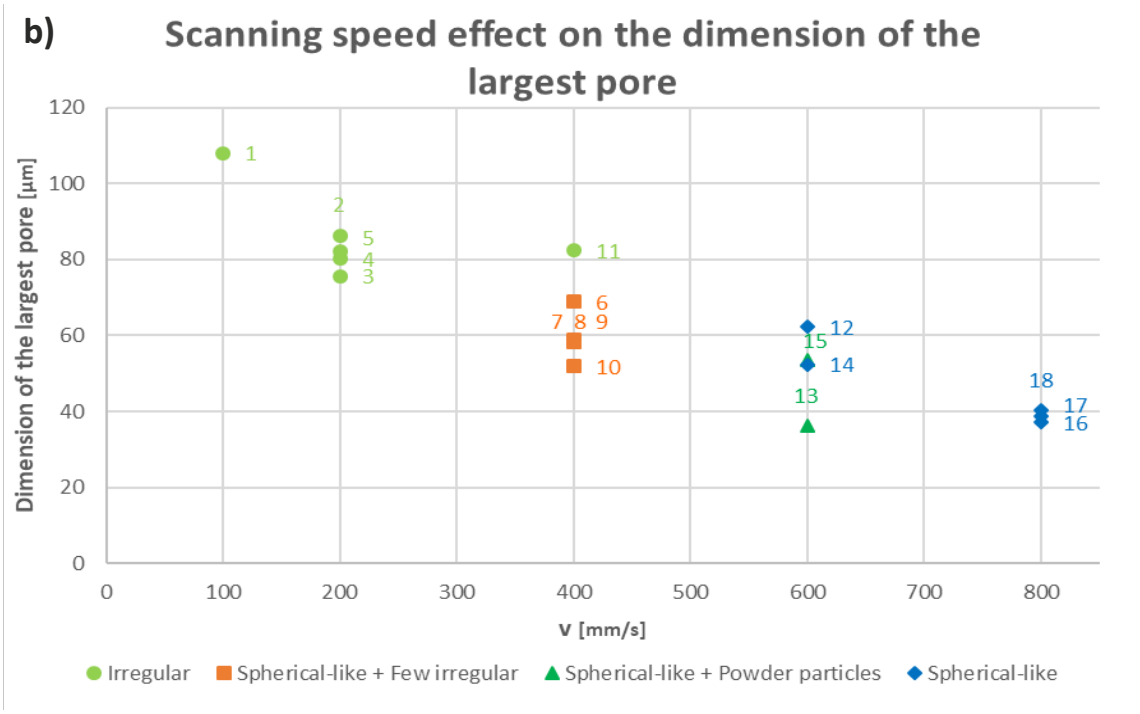

Figure 35 – Graphs of the: a) dimension of the largest pore and typical pore shape effect on the porosity; and, b) scanning speed and typical pore shape effect on the dimension of the largest pore

To summarize, specimens built with a scanning speed of 400 mm/s presented high porosity (above 1%), an increasing of the porosity was observed with the decrease of the scanning speed. With 600 and 800 mm/s scanning speeds specimens with nearly 100% density were built.

Increasing the hatching distance from 0.05 to 0.13 mm resulted on lesser porosity for lower scanning speeds. Regardless of increasing the hatching distance resulted in greater porosity percentages, the increase to 0.15 mm originated in higher porosity, above the values for the hatching distance of 0.05 mm. For higher scanning speeds (600 and 800 mm/s) the effect of the hatching distance was insignificant.

In specimens with larger pores, it was observed that the typical pore shape is irregular, and spherical-like for specimens with nearly 100% density. The increase of the scanning speed decreased the pore size. Larger pores were found in specimens with higher porosity. Figure 36 represents an image mapping with one image from each specimen, there is visible the effect of the scanning speed and hatching distance on pore distribution, size and shape. Laser power and layer thickness were not studied.

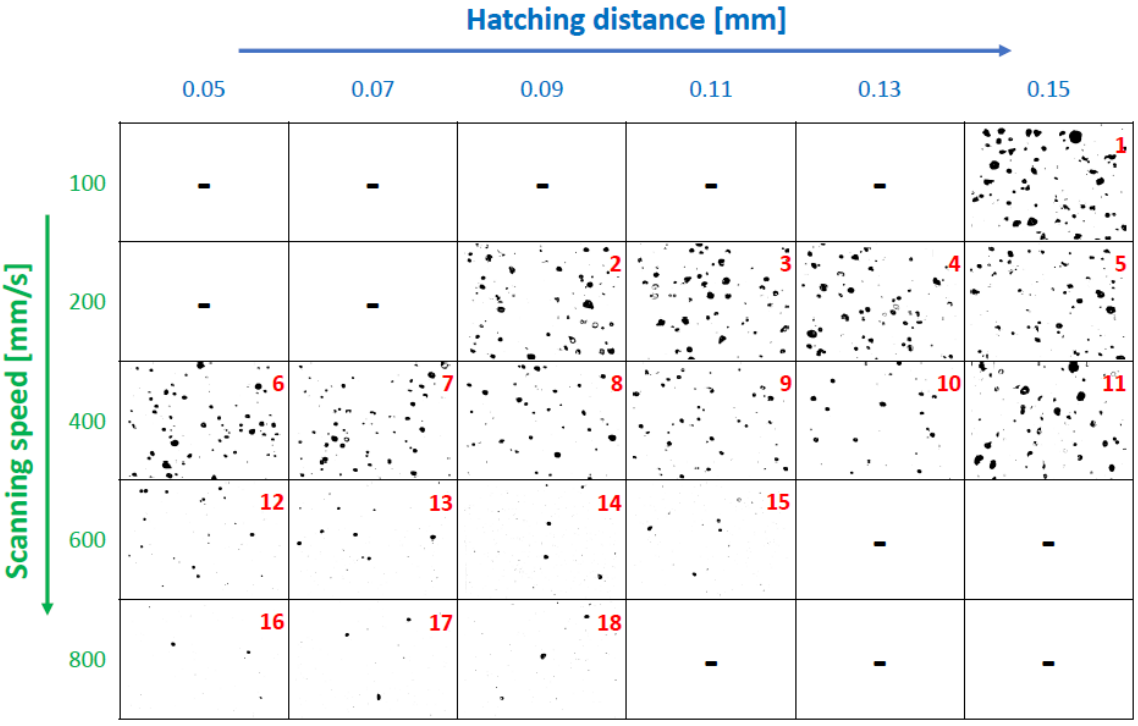

Figure 36 – Image mapping of the scanning speed and hatching distance effect on pores distribution, size and shape (magnified image in Annex 5)

4.2 RESIDUAL STRESS ANALYSIS

A total of 9 cuboids with 20 x 20 x 15 mm were built in the LPBF machine to study the residual stresses in as-built and heat-treated conditions (3 specimens for each condition). All the specimens were built on the same substrate (see Figure 37.a) with the following process parameters: 95 W laser power, 20 µm layer thickness, 800 mm/s scanning speed and 0.05 mm hatching distance.

No post-process treatments were performed before marking and removing the specimens from the substrate by W-EDM. The identification of the specimens in

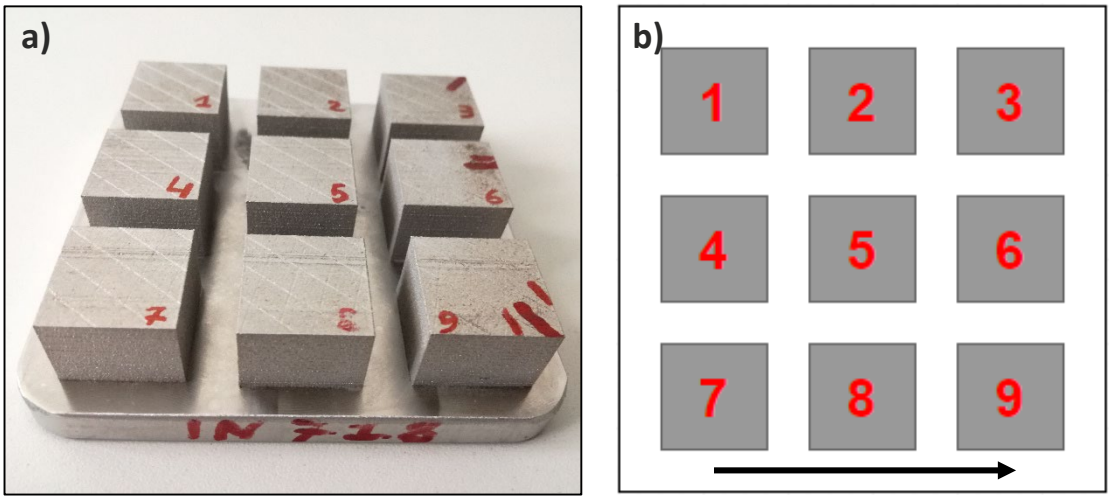

Figure 37 – Specimens for residual stress analysis: a) aggregate (substrate plus specimens) after removed from LPBF machine; and b) illustration of the identification of the specimens (condition: 1 – 3, as-built; 4 – 6, solution annealing; and, 7 – 9, solution annealing plus double aging) and the respective localization on the substrate (the arrow identifies the re-coater travel direction)

accordance with the localization of them on the substrate is illustrated in Figure 37.b (the arrow identifies the re-coater travel direction). In Figure 37, specimens: 1, 2 and 3 correspond to the as-built condition; 4, 5 and 6 to SA heat-treated; and 7, 8 and 9 to SA plus DA heat-treated. The heat treatment is described in the next subchapter.

The specimens were prepared, and then the RS measurements were performed by the hole-drilling strain-gage method on top and lateral surfaces for every specimen. After performing the RS measurements, one specimen of each condition was sectioned and then the microstructure was analyzed by SEM.

The microstructure was analyzed mainly on the borders of the hole resultant from the RS measurements. Apart from the identification and distribution of the phases present in the different conditions, the microstructure can also provide relevant information about changes in the RS profile, as RS magnitude and direction can vary along the depth of the measurement.

4.2.1 HEAT TREATMENT DESCRIPTION

Usually, the mechanical properties of IN718 parts are enhanced by performing a SA plus DA heat treatment (Zhou et al., 2019). Standardized heat treatments exist and ASTM F3055 (2014) standard recommends using the same as for wrought IN718. Figure 38 represents the time-temperature profile of the SA plus DA heat treatment.

SA was performed at 1065°C for 1h followed by AC, per AMS 5664 (SAE, 2017). DA was performed at a temperature of 720°C for 8h followed by FC for 2h to a temperature of 620°C, maintained at that temperature for 8h and then AC, per AMS 5662 (SAE, 2016).

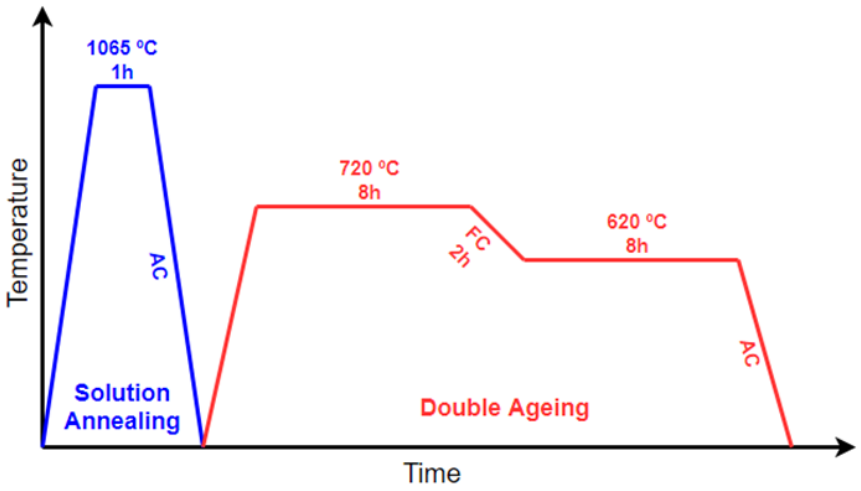

Figure 38 – Time-temperature profile of the solution annealing plus double aging heat treatment

4.2.2 PROCEDURE FOR THE RESIDUAL STRESS MEASUREMENT

The residual stresses were measured by the hole-drilling strain-gage method. This method is standardized by the ASTM E837 (2013) standard. In this subchapter is detailed the full procedure for carrying the RS measurements by the hole-drilling strain-gage method, which is approached in the subchapter 2.5.

The positions on the specimen where the measurements were performed, top (drilling along the build direction) and lateral (drilling perpendicular to the build direction and plane of the re-coater travel direction), are illustrated in Figure 39.a as rosettes and the drilling target (the arrow indicates the build direction). The drilling was performed at a distance of 4.5 mm from the border, the minimum by the standard. It was not done at the center of the surface to allow a new measurement in the same specimen if required.

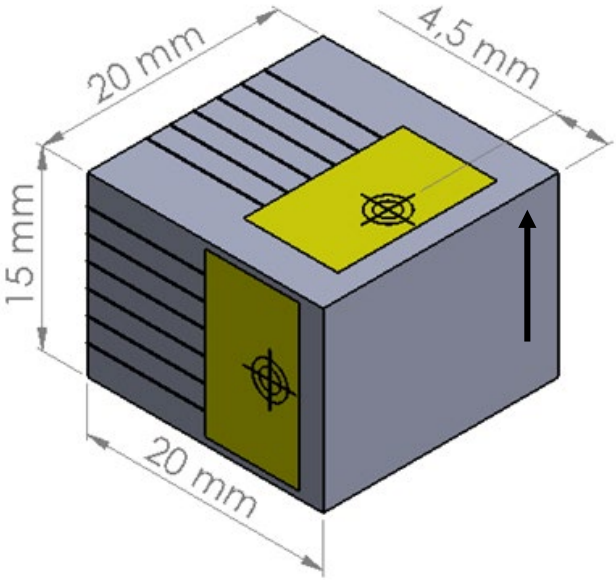

Figure 39 – Illustration of the rosette positioning for measurements (the arrow represents the build direction)

To perform the RS measurements was used the equipment MTS3000 – RESTAN (see Figure 40.a) and the software o RSM from SINT Technology (Italy). The rosette K-RY61-1.5/120R from HBM (Germany) was used, shown in Figure 40.b, it is suitable for near borders measurements and allows non-uniform RS measures up to 1 mm depth. It has an external size of 8 x 13.5 mm and it is recommended to use drills with a diameter between 1.8 to 2.1 mm ("K-RY61-1.5/120R," n.d.). It is a counter-clockwise type B rosette in accordance with the ASTM E837 (2013) standard.

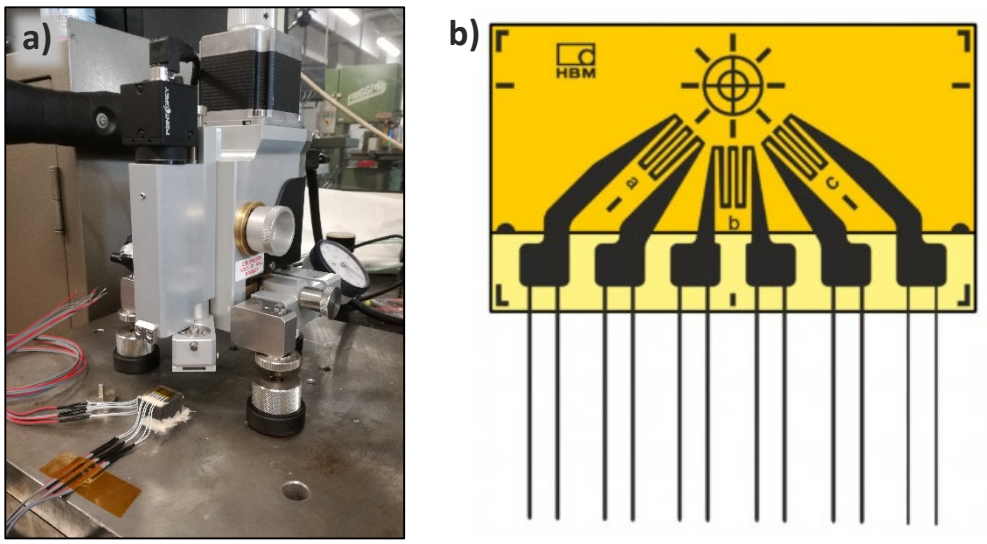

Figure 40 – Hole-drilling strain-gage method: a) MTS3000 – RESTAN equipment; and b) K-RY61-1.5/120R rosette ("K-RY61-1.5/120R," n.d.)

Previously to the start of the measurements the specimens were prepared and cleaned in order to install the rosettes on the surfaces. The top and lateral surfaces were manually and slowly polished to remove the high roughness resultant from the LPBF process. The opposite surfaces were also polished to guarantee a good pinning of the specimens on the positioning base.

The surfaces for rosette application were then cleaned with a RMS1 spray solvent from HBM (Germany) to remove any dirt and promote a good bonding of the rosette on the surface. The rosettes were attached to the surface with a Z70 glue from HBM (Germany). A X60 cold curing adhesive from HBM (Germany) was used to glue the rosette wires on the specimen, to prevent wire fracture by unexpected pulls. Figure 41.a shows one specimen after the application of the rosettes. Next, the specimen was mounted on the positioning base, using the X60 adhesive, with the surface to be drilled facing upwards, as shown in Figure 41.b, and the wires connected to the amplifying device.

The test setup of the SINT RSM software consisted of inputting the material (IN718) properties, selection of the rosette and inputting of the gage factors given by the rosette manufacturer, and definition of the drilling parameters (see Figure 42). A carbide "inverted cone" bur (drill) with 1.8 mm diameter was used with a feed rate of 0.1 mm/min. A hole with 1.2 mm depth was made sequentially in 48 drilling steps of 25 µm.

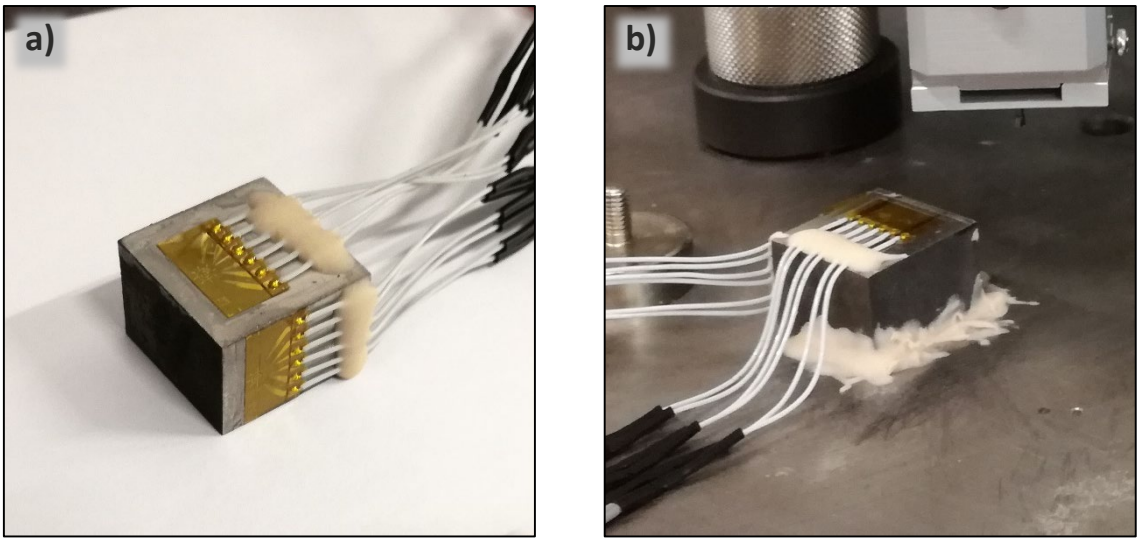

Figure 41 – Hole-drilling strain-gage method: a) specimen after application of the rosettes; and b) specimen mounted on the positioning base

It is crucial to verify the perpendicularity of the equipment with the positioning base. As well, the verification of the drill condition must be done previously to every measurement. The equipment is equipped with an optical system connected to a computer to center the drill with the rosette. After accomplishing the drill centering, the zero setting was performed, it is, determining the starting depth for the measurements. The zero setting is done by an electrical system, when the rotating drill removes the protective tape of the rosette and touches the metal, an electrical signal is emitted, then the software stops the drill and sets the zero position.

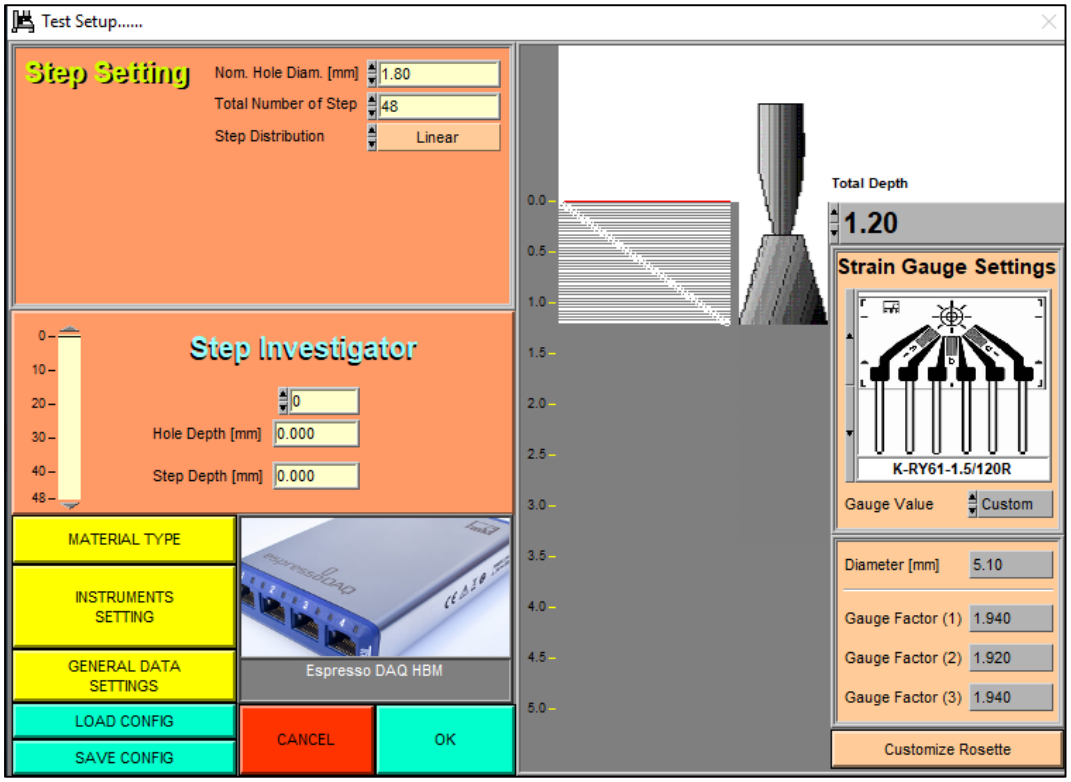

Figure 42 – Test setup on the SINT RSM software from SINT Technology (Italy)

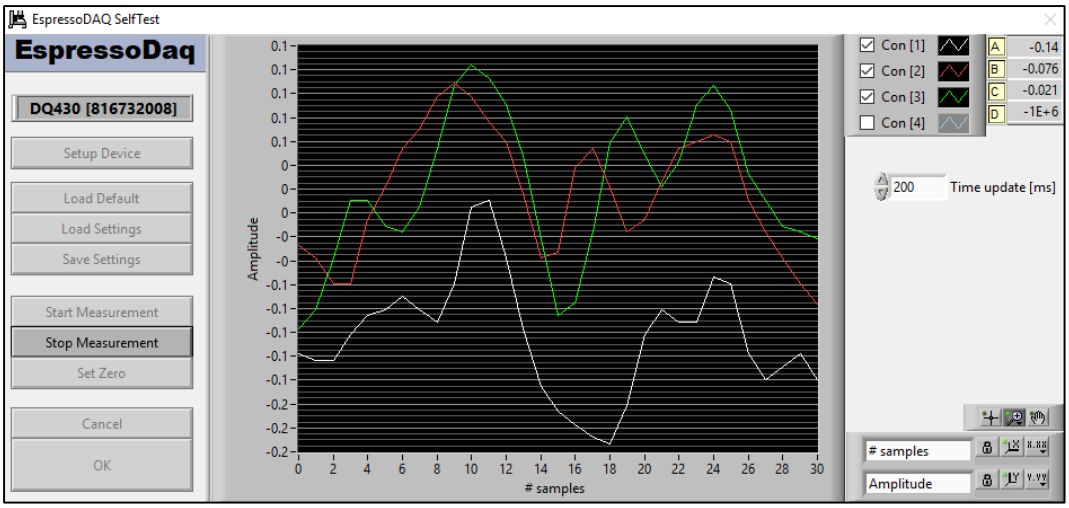

Figure 43 – Tare of the strain signal on the SINT RSM software from SINT Technology (Italy)

Then, the hole-drilling strain-gage method is ready to be started. When starting the measurement, the strain signals must be tared to zero. As shown in Figure 43 the signal cannot be tared exactly to zero as there are always small oscillations, however, when the oscillation is small, as in Figure 43, it has no significant impact on the final results and the measurement must be started.

In Figure 44 is presented the window of the software that is available during the measuring process, which is automatic along all the 48 drilling steps. There is shown the test status to know in which step the process currently is and the information about the measured strain, which will be later converted in RS values.

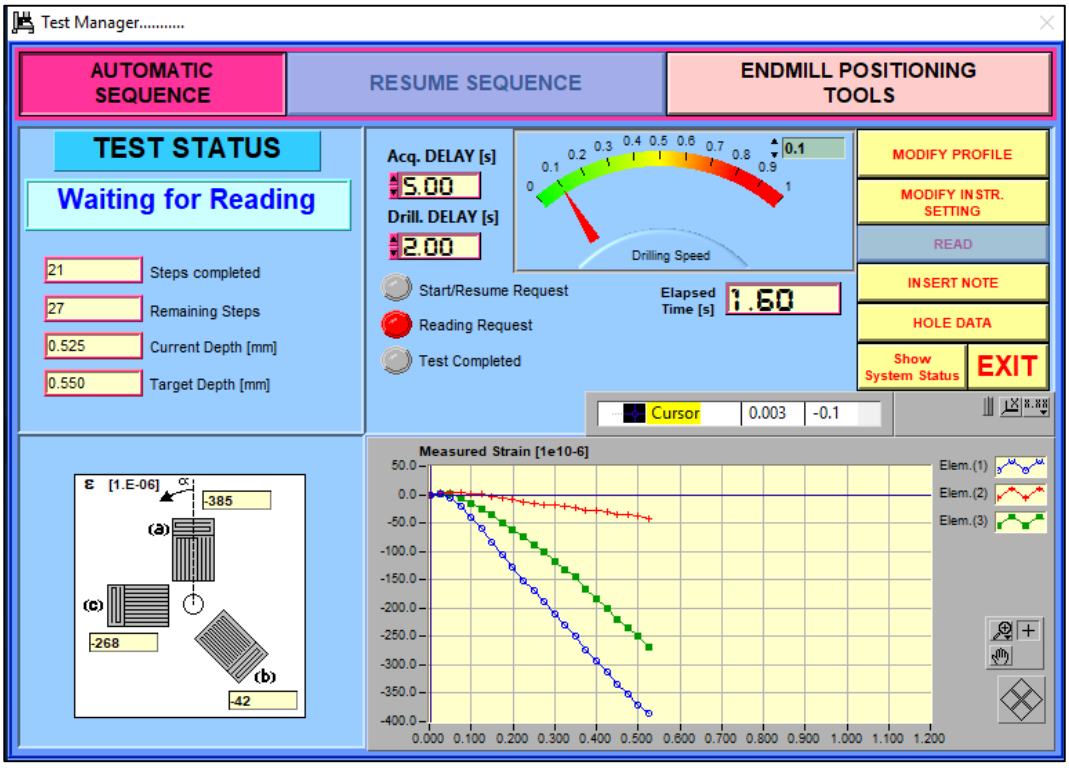

Figure 44 – Test manager on the SINT RSM software from SINT Technology (Italy)

Just after finishing the strain measurements, with the aid of the optical system previously used to center the drill with the rosette, the diameter and the eccentricity of the produced hole was determined. Those parameters of the hole are taken in consideration when calculating the RS from the strain measured.

To calculate and get the RS profiles the SINT EVAL software from SINT Technology (Italy) was used. The data acquired with the SINT RSM was loaded to the SINT EVAL. The calculation method selected was the extended non-uniform, present on the hole-drilling strain-gage method standard, ASTM E837 (2013). It is destined to calculate non-uniform RS and is suitable for measurements performed in "thick" specimens. The calculations were made to a depth of 1 mm in 20 calculation steps with a linear distribution of calculation steps.

As it is the extended method, the software determined calibration constants to increase the precision of the calculated RS. Moreover, small strain measuring errors can result in large RS calculation errors owing to the large number of depth steps (48 drilling steps), thereby, Tikhonov regularization was used. After setting up all the calculation parameters, reports were acquired containing the RS magnitudes and direction, which are presented in next subchapter.

4.2.3 RESULTS

The strains were measured, by the hole-drilling strain-gage method, on the specimen surfaces and then the RS calculated as detailed in the previous subchapter. From Figure 45 to Figure 50 are shown graphs of the depth profiles of the calculated RS magnitudes and direction for all the conditions (as-built, solution annealing and solution annealing plus double aging) and surfaces (top and lateral). All the values used to build these graphs are available in table format in Annex 6.

In order to simplify the identification of the samples and the reading of the results the following codification was adopted for the graphs captions: results corresponding to the measurements made on the top surface (T); results corresponding to the measurements made on the lateral surface (L); number of the specimen regarding the Figure 37 (1 to 9), which corresponds to a specific specimen condition (see Figure 37 caption); values corresponding to the maximum principal stress (max); and, values corresponding to the minimum principal stress (min).

Graphs from Figure 45 show the RS magnitude and direction values obtained in the as-built condition on top surface. The RS magnitude profile (Figure 45.a) is similar for all of the 3 specimens. At immediately near the surface the RS magnitude is relatively low (higher value is 153 MPa for specimen 1) when compared with deeper values. From 0.1 mm and deeper, the values are around 400 MPa and above. A slight increasing trend was observed after the depth of 0.4 mm. Also, σ_{max} and σ_{min} have an identical trend and

have very close values. The RS direction graph (Figure 45.b) shows a few deviations among all the 3 specimens. Nevertheless, almost all the RS direction values are between 0° and 90° for all of the specimens. The scattered point in the graph corresponding to the specimen 1 at near 0.6 mm depth is relatively close to the positive 90° angle, thereby, it is not out of the trend (90° and -90° correspond to the same orientation).

Figure 46 shows the graphs for the same condition, but for the lateral measurements. In Figure 46.a graph the same behavior was noticed at immediately near surface RS magnitude values. However, higher values were obtained for deeper distance, between 600 and 900 MPa from 0.1 to 0.6 mm depth. After 0.6 mm depth a slightly decreasing

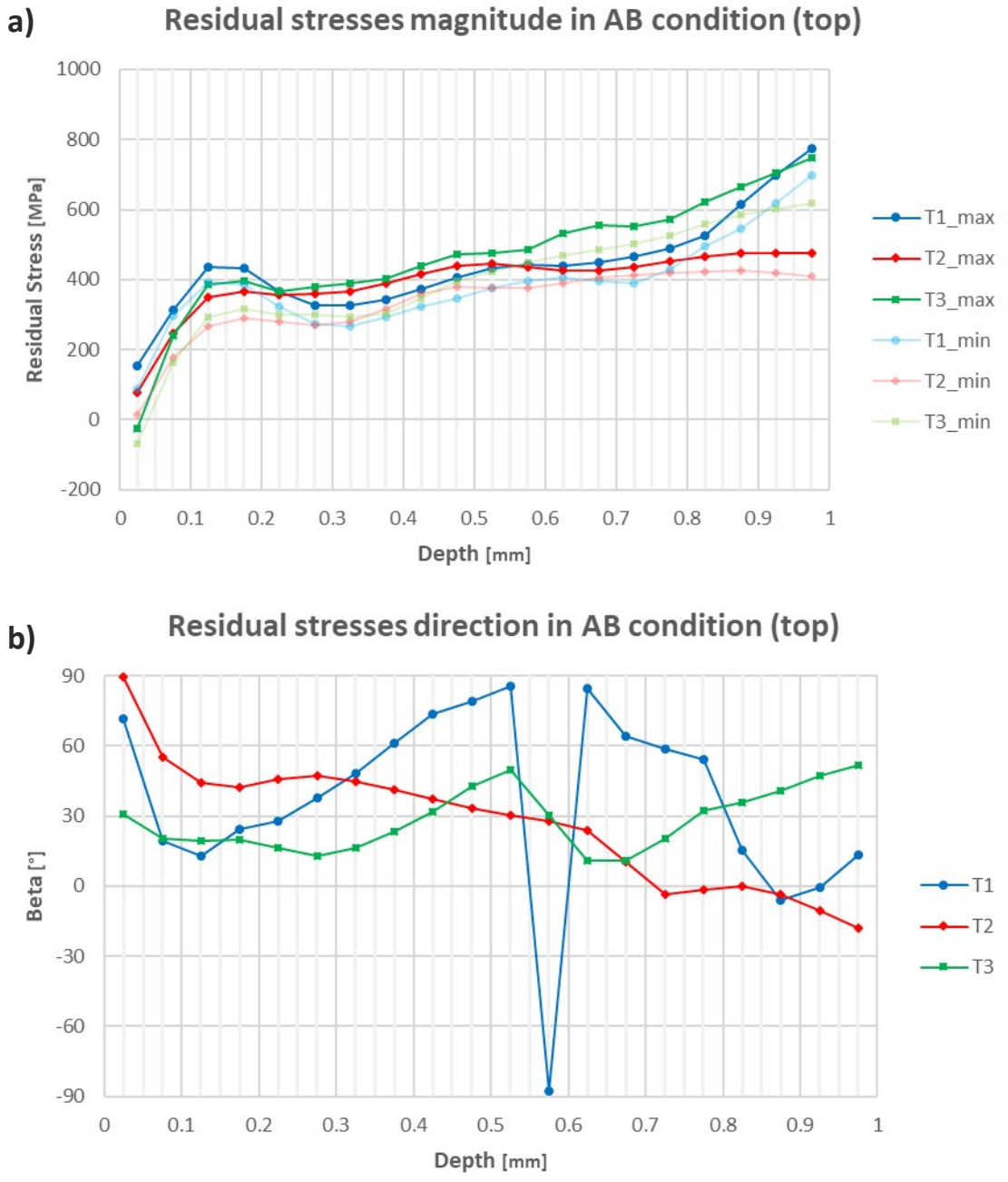

Figure 45 - Residual stresses in as-built condition (top): a) magnitude; and b) direction

trend was observed, with values between 400 and 600 MPa for specimens 1 and 2. Also, a few oscillations were identified for all the specimens, these oscillations are of 200 MPa magnitude. For example, specimen 2 has near 900 MPa at 0.125 mm and decreases to 720 MPa at 0.275 mm, increasing one more time at 0.375 mm to around 850 MPa.

In this case, a significant difference of the σ_{max} and σ_{min} was noticed, with σ_{min} not exceeding 308 MPa (specimen 1) and being around the 200 MPa. Owing to that wide difference between maximum and minimum values, the RS direction graph (Figure 46.b) shows a steady decreasing trend. That big contrast between maximum and minimum stress values means high anisotropy in the RS distribution.

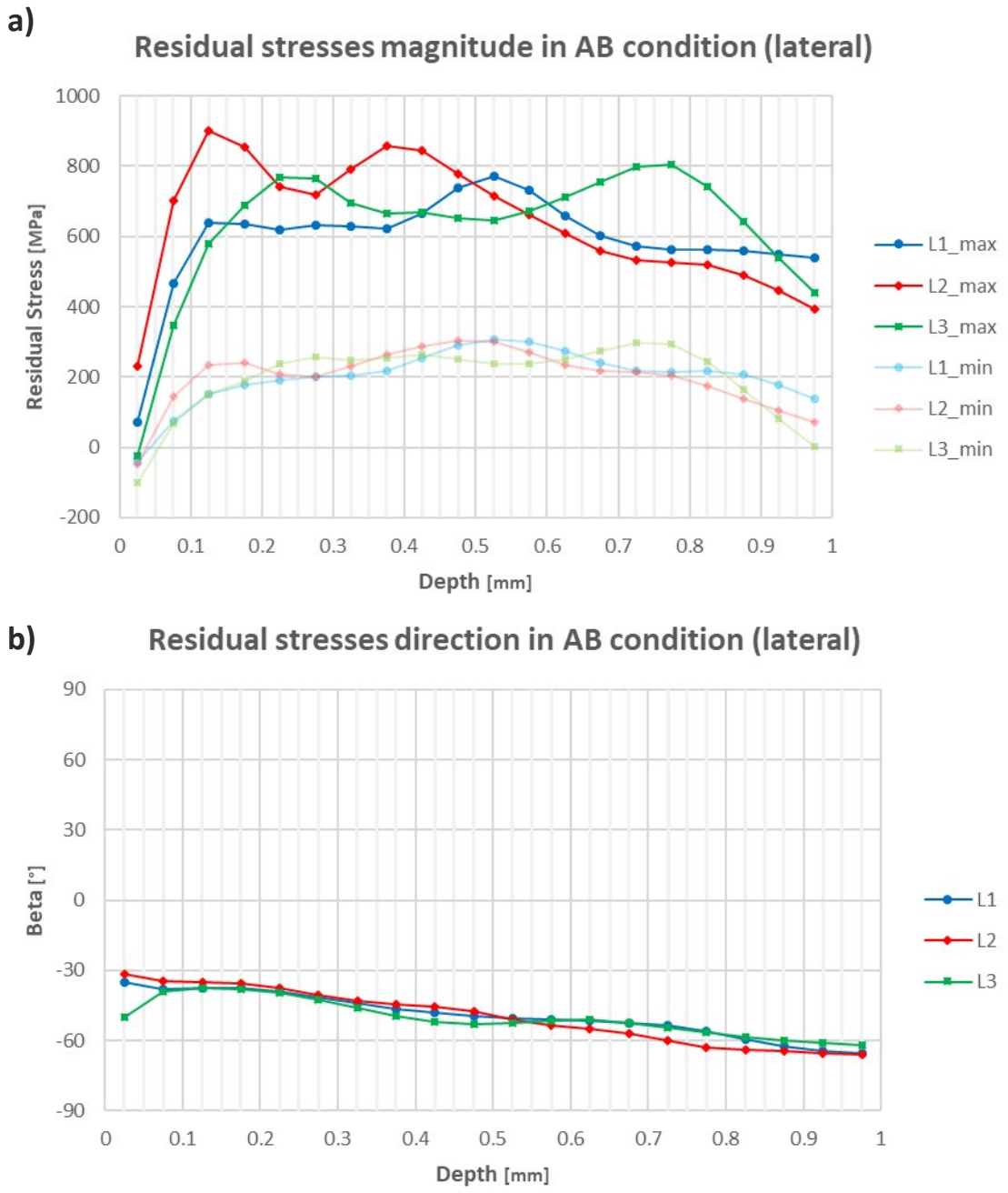

Figure 46 - Residual stresses in as-built condition (lateral): a) magnitude; and b) direction

Graphs related to the SA condition are presented in Figure 47 and Figure 48 for top and lateral surfaces, respectively. From as-built to SA condition a marked decrease in the RS magnitude was observed.

In Figure 47.a the values for all the specimens are very similar until 0.6 mm depth. At immediately near the surface, compressive stresses were measured, from around 100 (σ_{max}) to 306 MPa (σ_{min}). After 0.2 mm depth the values stabilize between 50 and 100 MPa. After 0.6 mm depth a discrepancy among all the specimens was noticed, with specimen 4 and 6 presenting odd magnitude values. Specimen 4 raises to tensile stresses of almost 800 MPa. Specimen 6 decreases to compressive stresses of 100 MPa and

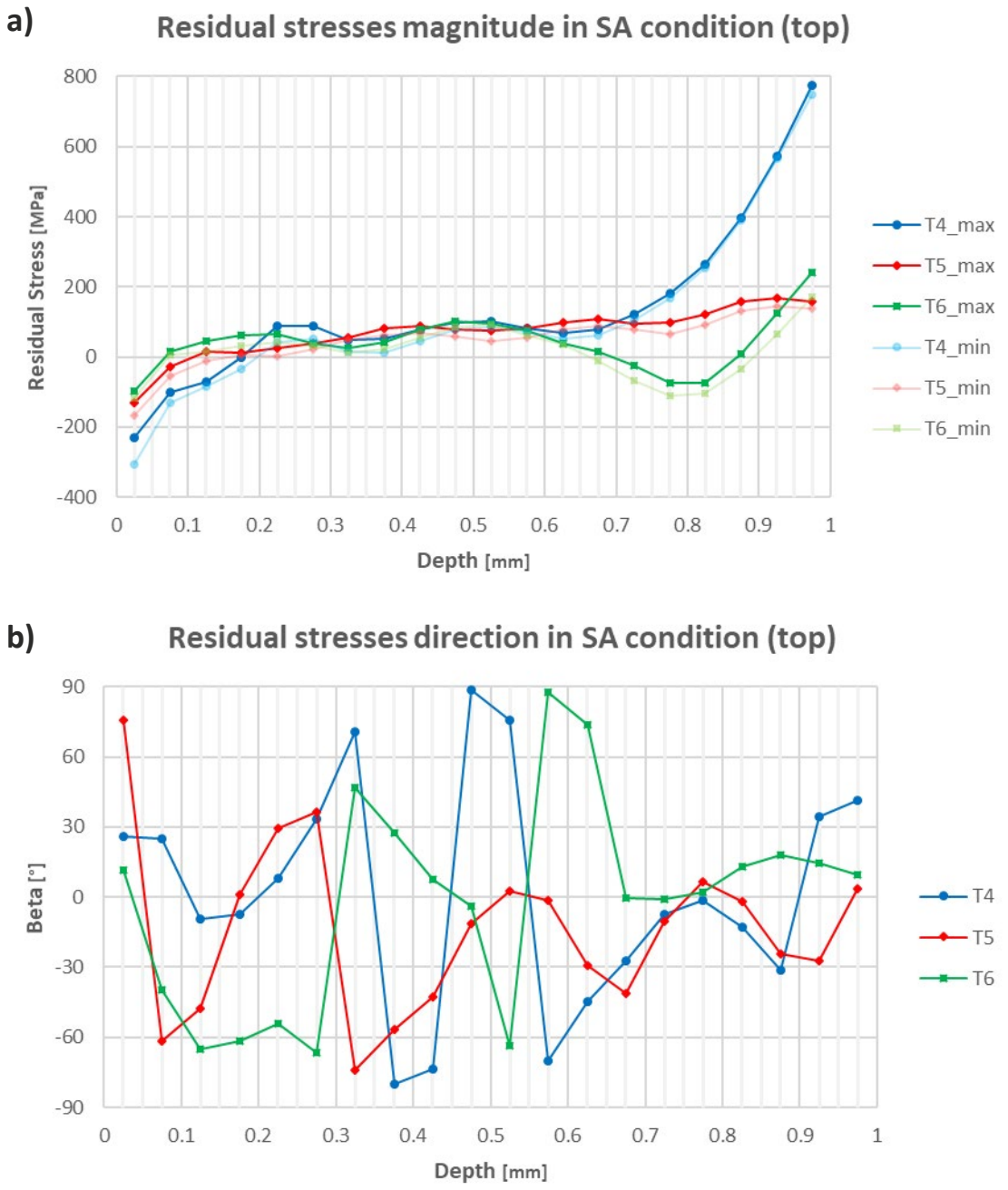

Figure 47 - Residual stresses in solution annealing condition (top): a) magnitude; and b) direction

abruptly rises to over 200 MPa tensile stresses. About RS direction, no results could be determined (Figure 47.b) owing to the large deviation of the results, same happened to SA plus DA top (Figure 49.b).

Compressive stresses at immediately near the surface were also observed in the lateral measurements (Figure 48.a). Although relatively low magnitudes were obtained when comparing with the as-built condition lateral, the existence of oscillations remained. The majority of the values are between 50 and 150 MPa. For specimen 4, with the oscillations it reaches the 200 MPa. Compressive stresses at middle depth were noticed

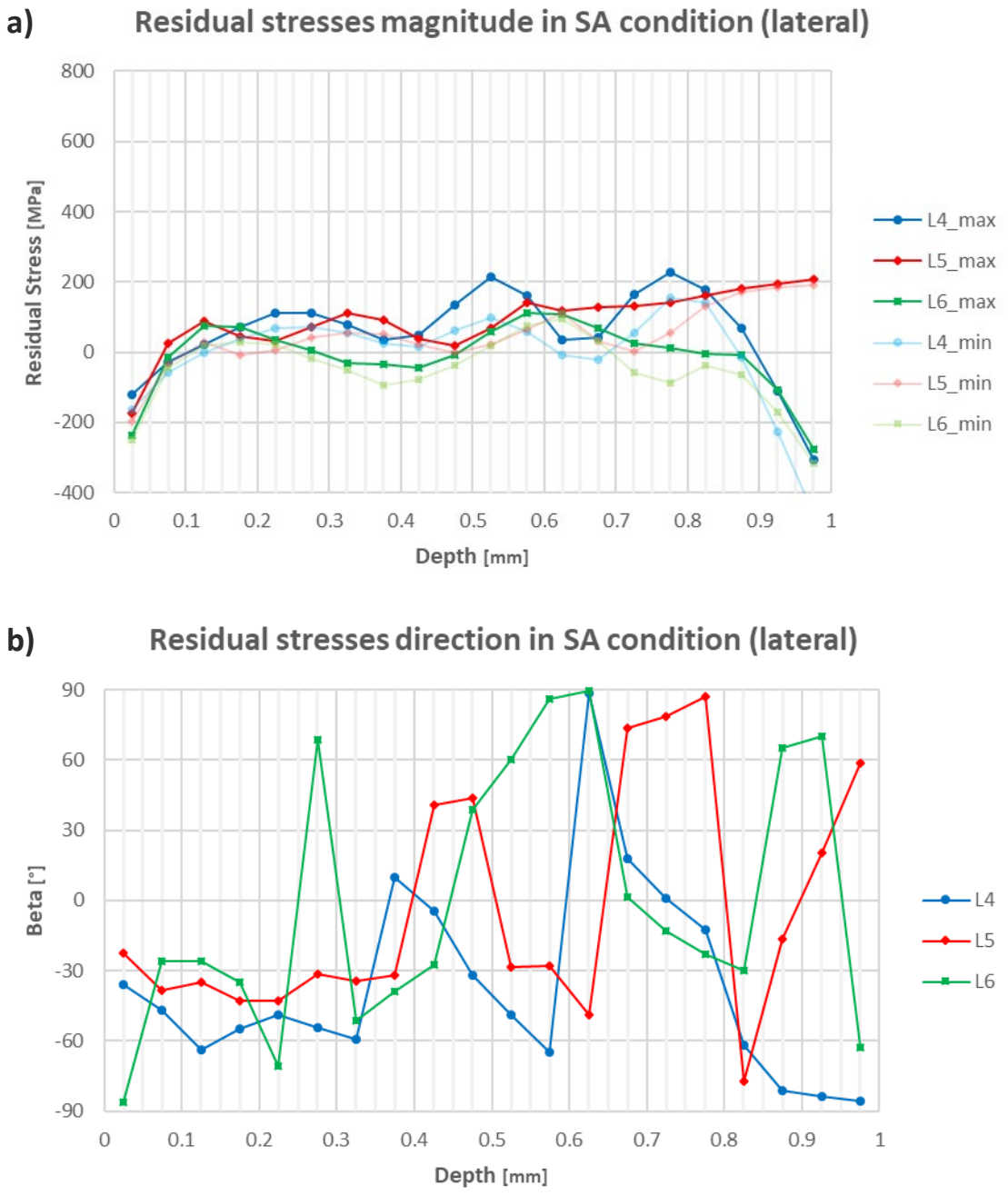

Figure 48 - Residual stresses in solution annealing condition (lateral): a) magnitude; and b) direction

for specimen 6. Again, at greater depth oddly behavior was observed, specimens 4 and 6 decreased to around 400 MPa compressive stress.

About RS direction of the lateral measurements, only a small group of values at near the surface can be considered (Figure 48.b), angle values between -30° and -60°.

For the SA plus DA condition specimens, the RS magnitude decreased even more, as can be seen in Figure 49.a for top and Figure 50.a for lateral measurements. Once again, compressive stresses of relevant magnitude (above 170 MPa for top measurement of specimen 8) were observed at immediately near the surface for both top and lateral. In

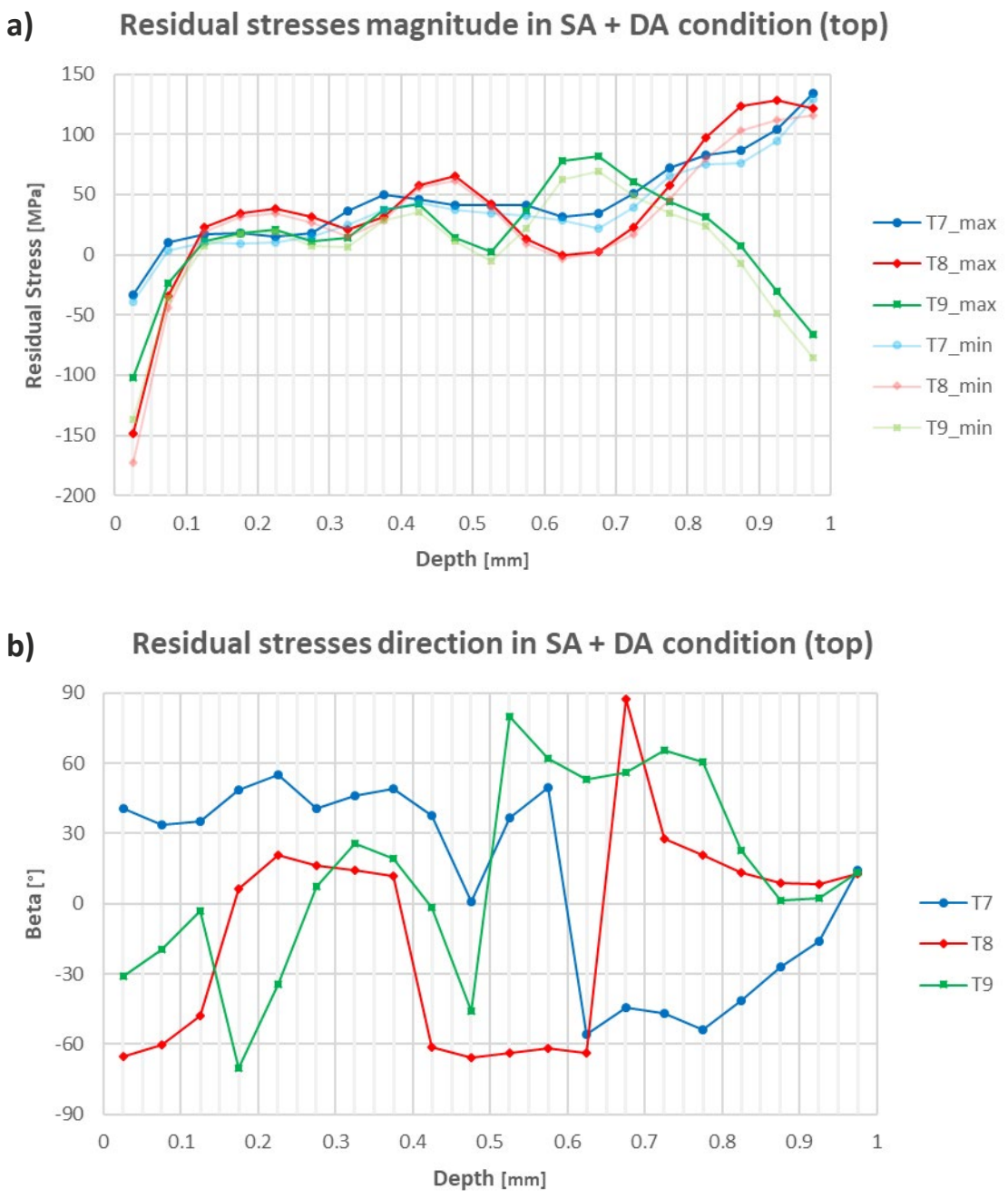

Figure 49 - Residual stresses in solution annealing plus double aging condition (top): a) magnitude; and b) direction

Figure 49.a, up to 0.4 mm depth the RS values are between 10 and 50 MPa, then, deeper than that, oscillations were recorded. With that oscillations specimens 8 and 9 show no RS at a specific depth. At 1 mm depth all the specimens show odd magnitude values.

The SA plus DA lateral RS magnitude (Figure 50.a) shows lower oscillation magnitudes than the top measurements and all the specimens have identical values. A slightly increasing trend was observed. However, the values are around 50 MPa and do not go above 112 MPa (tensile stress). A compressive stress of 132 MPa was noted for specimen 7, but it has a large deviation compared with the others two.

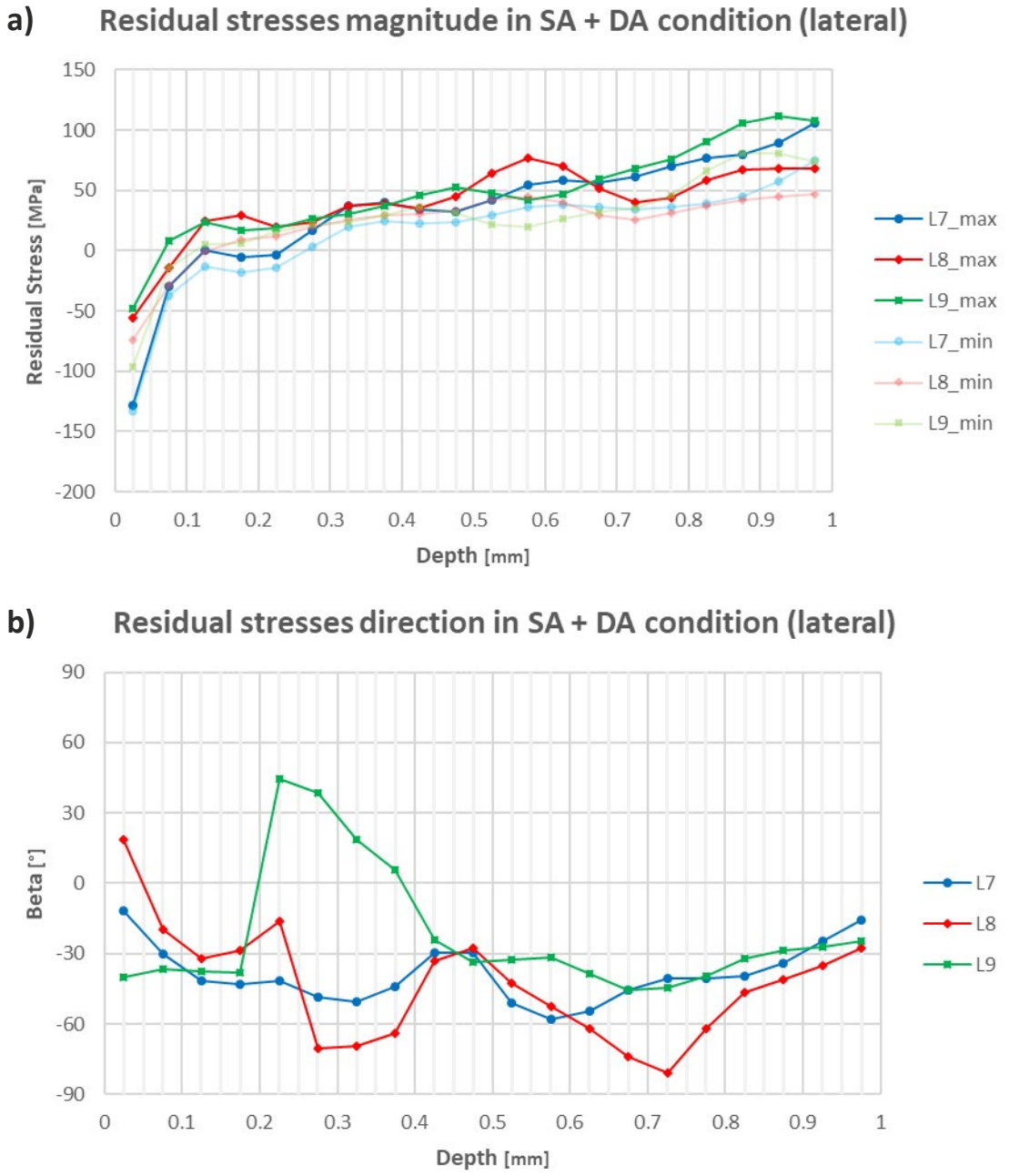

Figure 50 - Residual stresses in solution annealing plus double aging condition (lateral): a) magnitude; and b) direction

Related to the RS direction, shown in Figure 50.b graph, results can be drawn despite the fact that a few values vary oddly. The same that was observed in Figure 46.b and Figure 48.b (only for the near surface values) graphs corresponding to the lateral measurements in the as-built and solution annealing condition, respectively, was noticed here. The majority of the direction values are between -30° and -60°.
The average and standard deviation of the three results for every condition is presented in Figure 51.a and Figure 51.b, for top and lateral measurements, respectively. Most of the observations pointed out previously related to the individual graphs are maintained.

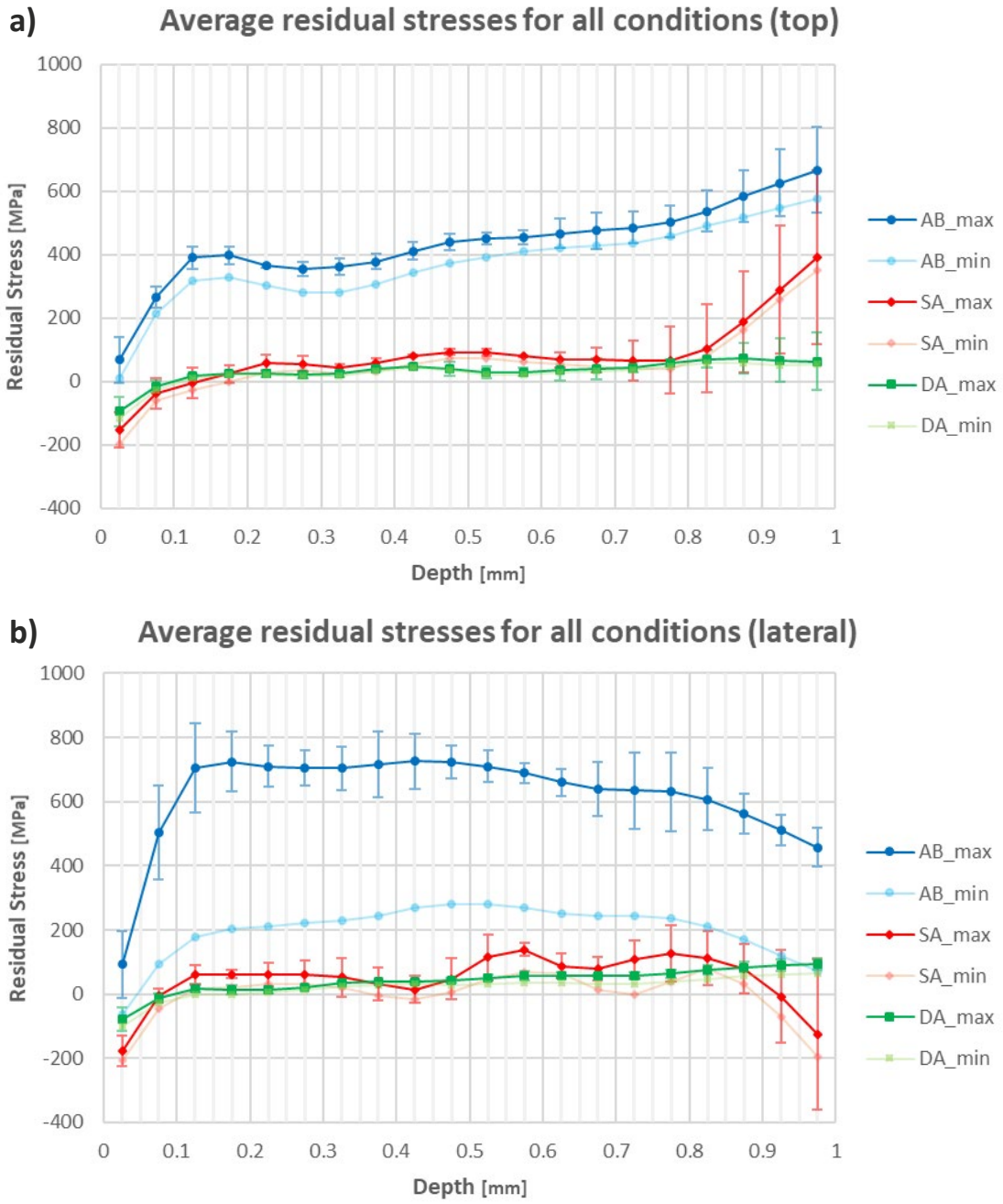

Figure 51 – Residual stresses average magnitude and standard deviation for all conditions: a) top; and b) lateral

It can be noticed in Figure 51.a that, for top measurements the RS values have an increasing trend both for as-built and SA condition. For lateral measurements (Figure 51.b) the inverse trend is observed. However, for SA specimens the standard deviation starts to gradually increase to odd values after a certain depth. The SA plus DA specimens shows a plain trend along almost all the depth, only at immediately near the surface there is an increasing trend due to the existence of compressive stresses that turn into tensile stresses.

4.2.4 DISCUSSION (WITH MICROSTRUCTURE ANALYSIS)

For the as-built condition the RS magnitude is higher for the lateral measurements (average of 600 – 800 Mpa) than the top (average of 400 MPa). Also, it was observed that for lateral surface exist RS distribution anisotropy.

The uniform distribution of the RS on the top surface (horizontally distributed) is mainly related to the scanning strategy. With the 67° rotation between the layers, the melt pools cross each other layer after layer, it is, they are not built always in the same direction and overlapped. This way there is no tendency for the RS accumulation in a determined pattern.

However, for the lateral surface the scanning strategy has no influence all over the surface because the layer-by-layer principle. The β direction of -30° to -60° corresponds to the build direction for the lateral measurements, this means that the RS average of 600 – 800 MPa are along the build direction (vertically). Thereby, the minimum stresses of 200 – 300 MPa are on the horizontal plane, along the layer boundary.

This outcome is attributed to the layer-by-layer principle, when scanning a new layer on top of a much cooler one, previously built, the new deposited material undergoes a bending effect, which puts the boundaries of the previous layers in a tensile state. Layer by layer, the RS are accumulated in the vertical direction, this contributes to the release of the RS present in the horizontal direction.

The bending effect has more impact in the RS near the boundaries than in the interior of the material, that can be the reason for the decreasing trend in the RS magnitude of the lateral measurements. Notwithstanding, the RS test method decreases its accuracy as deeper the measurements are, which could be the reason for the increasing trend in the top measurements to odd values at final depth.

The microstructure in the as-built condition is shown in Figure 52. Figure 52.a shows the “fish-scale” feature, typical of the LPBF process, resulting from the melt pools and layer-by-layer principle. Owing to the rotating scanning strategy, the size and shape of the arcs are non-uniform, actually, near the bottom of Figure 52.a it is seen a melt pool that was cut longitudinally (delimited by the red lines). Figure 52.b image was taken in the

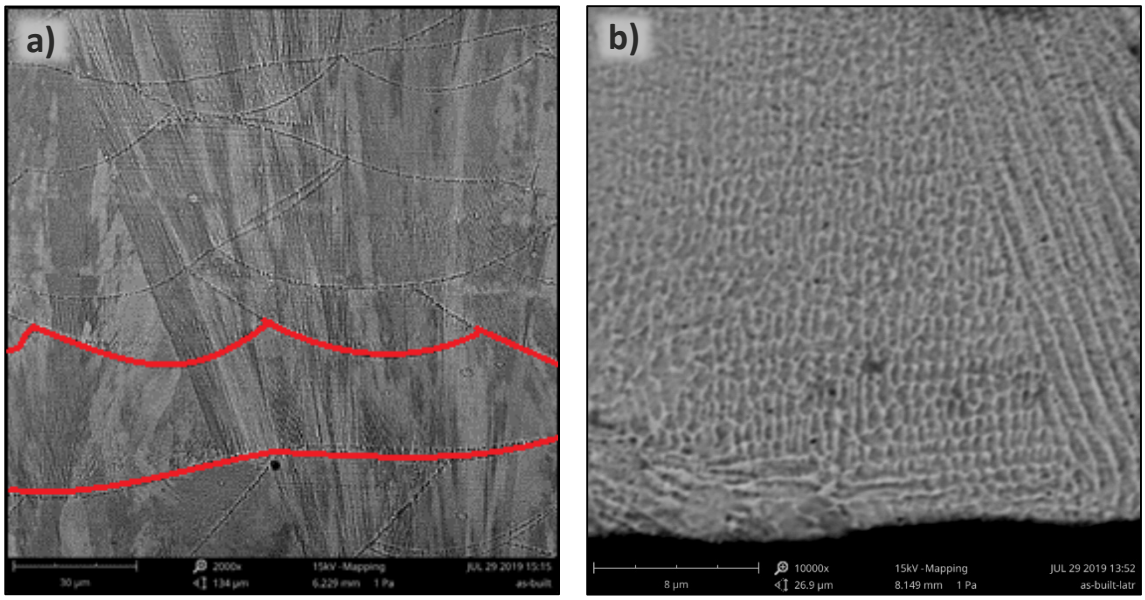

Figure 52 – Microstructure analysis of an as-built specimen: a) “fish-scale” feature; and b) fine columnar dendrites

boundary of the lateral hole (black irregular shape in the bottom of the image is part of the hole), there can be observed the fine columnar dendrites along the build direction.

The RS magnitude from the as-built condition to the SA condition decreased significantly, to RS values of 50 – 100 MPa on the top surface and 50 – 200 MPa on the lateral surface. After performing the SA heat treatment, it is expected that the Laves phase and carbides get dissolved, which are detrimental to the mechanical properties of the material (Cao et al., 2018; Tucho et al., 2017; X. Wang et al., 2017). Moreover, the SA was performed at 1065°C, thus greatly contributing to the RS relief.

RS magnitude oscillations were observed, mainly for the lateral measurements. The specimen 4 is the one showing larger oscillations (two peaks overtaking 200 MPa) and odd values at final deep, thereby, it was the specimen chosen for the microstructure

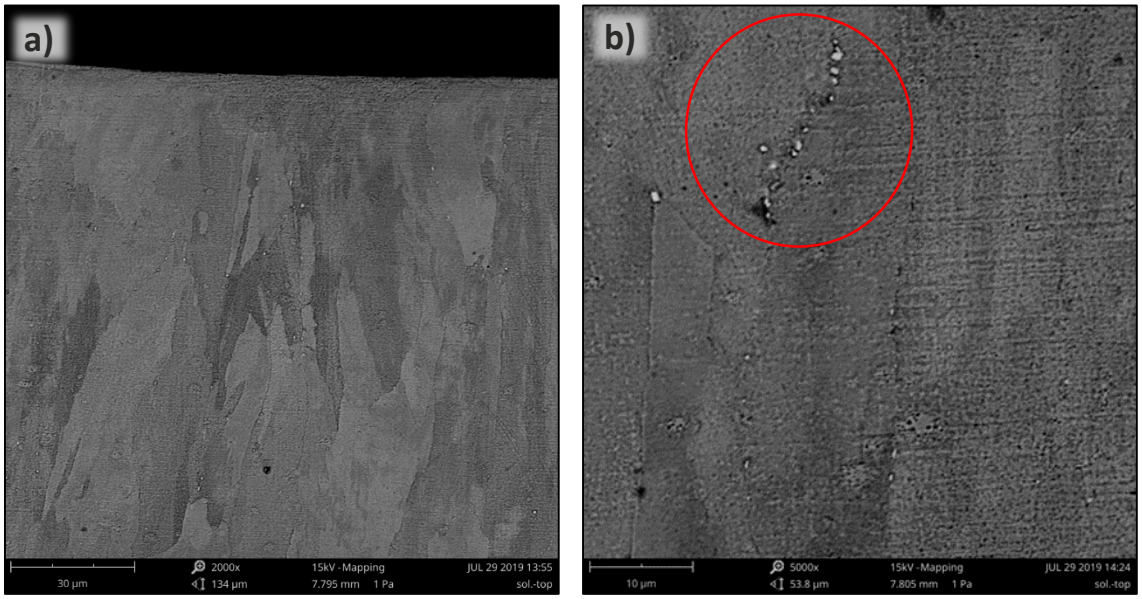

Figure 53 – Microstructure analysis of a SA specimen: a) grain growth; and b) series of carbides

analysis. Figure 53 shows the microstructure of that SA specimen. Comparing Figure 52.a (as-built) and Figure 53.a (SA) it can observed that grain growth occurred.

Figure 53.b shows a series of carbides (inside the red circle) found near the top hole. Other series of carbides of different sizes and randomly distributed were found near the holes, both top and lateral, at grain boundaries. These carbides may be generated by the segregations within the grain boundaries, therefore, areas with higher segregation concentrations can be subjected to more significant carbides precipitations. This phenomenon could be the reason for the oscillations in terms of RS magnitude. Also, it could have contributed to the odd values at the final depth. Those carbides were expected to be dissolved with the SA heat treatment.

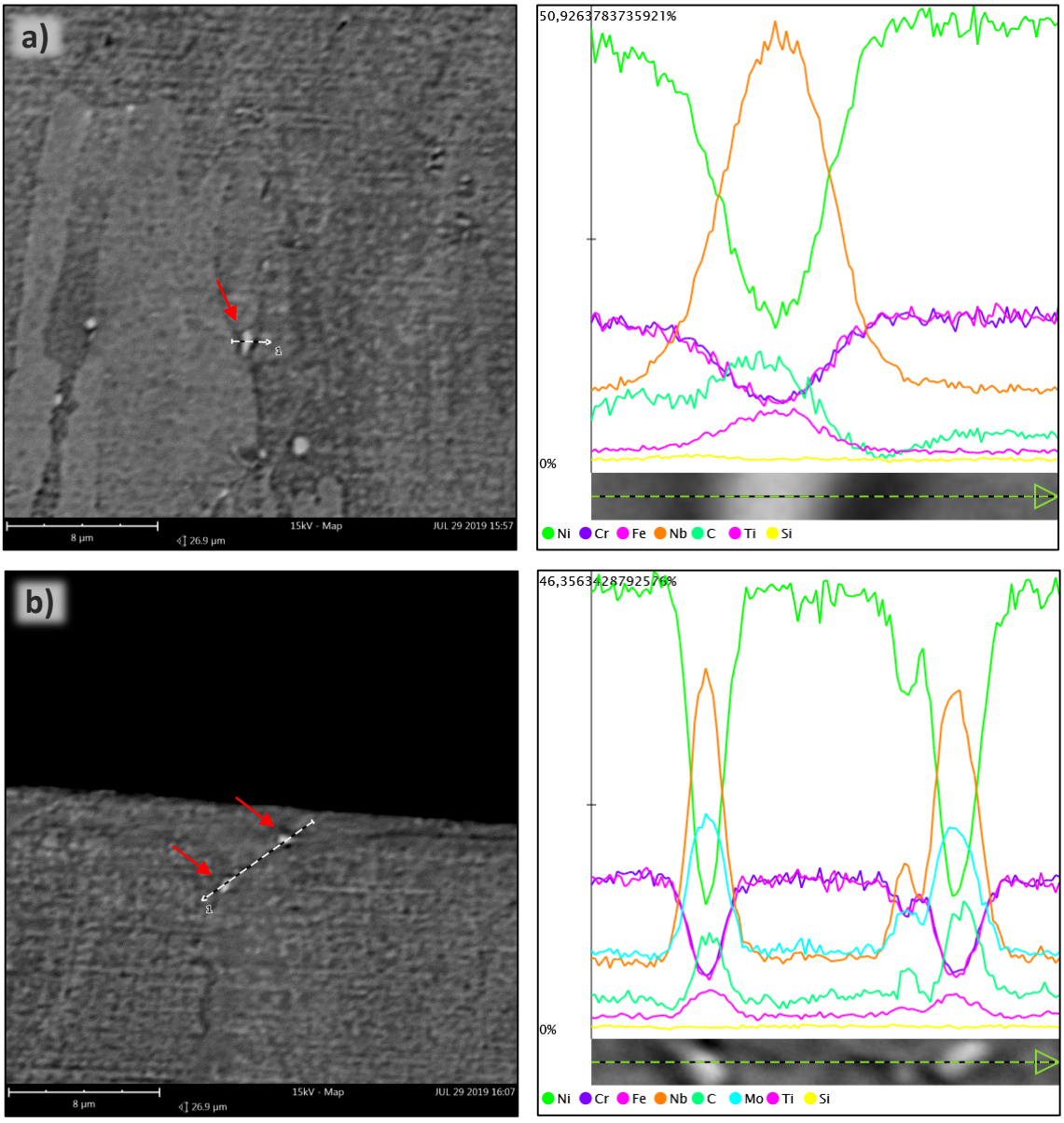

Figure 54 – Particle composition analysis of a SA specimen: a) Nb carbide; and b) two similar unidentified carbides

Carbides enriched in Nb, Mo and Ti were detected. Those carbides are pointed out with a red arrow in Figure 54.a and Figure 54.b. On the right-side images is presented the respective chemical composition of the carbides detected.

Regarding to SA plus DA specimens, a slight decrease of the RS magnitude was observed, to values between 10 and 50 MPa. However, large oscillations were noticed again and odd values at the final depth (mainly for top measurements). After performing the particle composition analysis, carbides of the same type detected in the SA specimens were found (see arrows in Figure 55.a). Also, needle-like Delta phase was detected at the grain boundaries (see arrow in Figure 55.b), which must have precipitated during the SA heat treatment.

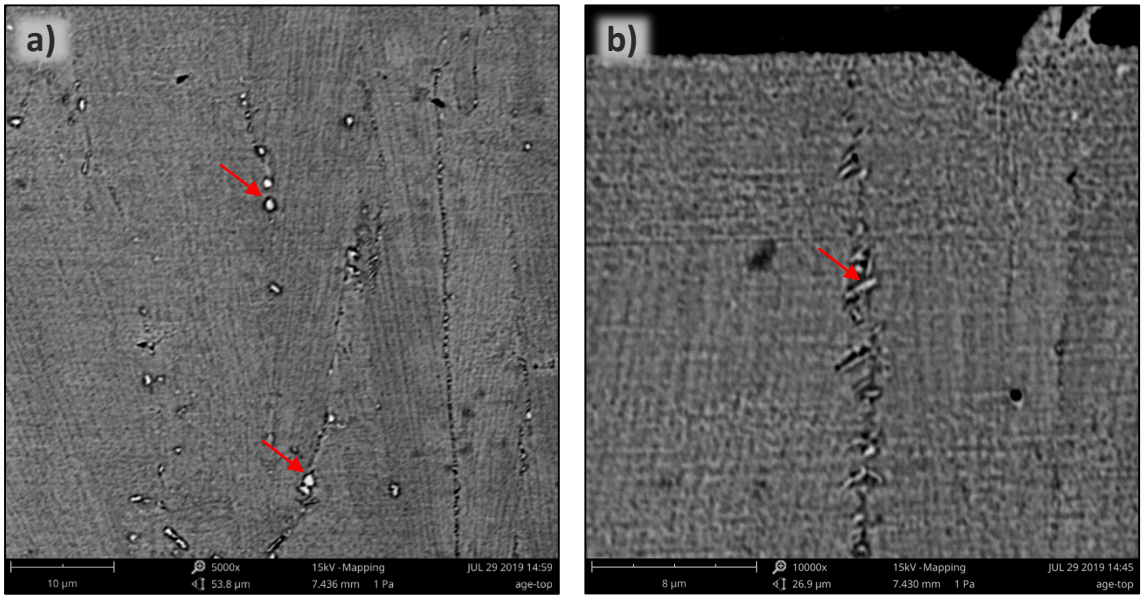

Figure 55 – Microstructure analysis of a SA plus DA specimen: a) unidentified carbides; and b) needle-like δ phase

A common observation from the SA and SA plus DA specimens is the compressive RS at immediately near the surface of all the six specimens, both top and lateral measurements. As in as-built specimens at the same depth the RS are tensile stresses, the compressive stresses are certainly related to the heat treatment.

When large parts are cooling after a high temperature heat treatment, it is normal to be generated compressive RS at near the surface, owing to the exterior fast cooling and the interior remaining hot for longer time. However, it was not inferred if the specimens are large enough to occur this effect. Those compressive stresses at near the surface will contribute positively to the fatigue life of the parts (Vrancken, 2016).

For SA plus DA lateral measurements, the anisotropy of the RS distribution observed in the as-built specimens is still present (vertically preferred). However, the difference between σ_{max} and σ_{min} is so small and the RS are very low, thereby, the anisotropy in the lateral surface of SA plus DA specimens is insignificant.

CONCLUSIONS

4.1 CONCLUSIONS

4.2 PROPOSALS OF FUTURE WORKS

5 CONCLUSIONS AND PROPOSALS OF FUTURE WORKS

5.1 CONCLUSIONS

Overall, it may be said that the purpose of this work was accomplished, study of the RS evolution of LPBF-ed IN718 parts before and after heat treatment, through the previously defined goals. Those consisted, firstly, in the selection of optimal LPBF process parameters for IN718 material and the study of the individual parameters influence in the porosity of LPBF-ed IN718 parts, and then in analyzing and discussing the RS evolution of LPBF-ed IN718 specimens in as-built condition and after heat treatment.

To summarize, 18 specimens were built for the selection of the optimal parameters, all with different combinations of LPBF process parameters. After determining the porosity for all the specimens by the Archimedes' method and a micrograph-based method, the analysis of the results come out with the selection of the following process parameters: P = 95 W, t = 20 µm, v = 800 mm/s and h = 0.05 mm, which built a specimen with nearly 100% density (0.139% average porosity).

From the study of the individual parameters, it was concluded that increasing the scanning speed is favorable for the porosity reduction. The highest scanning speed studied (800 mm/s) resulted in the lowest porosity percentages. For lower scanning speeds (200 and 400 mm/s) the optimal hatching distance was observed to be 0.13 mm. For these scanning speeds, lowering the hatching distances down to 0.05 mm resulted in an increasing trend in the porosity, nonetheless, the highest hatching distance (0.15 mm) resulted in the highest porosity percentages. The hatching distance effect on the porosity is less relevant for higher scanning speeds (at least for hatching distances lower than 0.13 mm). For scanning speeds of 600 and 800 mm/s no hatching distance trends were observed. Laser power and layer thickness were kept constant for all the 18 specimens, thereby, no conclusions about these two parameters can be drawn.

The pore size and shape were also analyzed. The porosity percentage is related to the pore size, larger pores were found in the specimens with higher porosity. Also was concluded that the pore size is connected with the pore shape, an abundance of irregular pores was observed in specimens with larger pores, and spherical-like pores were observed in specimens with smaller pores accompanied by a great decrease in the porosity. Moreover, as scanning speed is related to the porosity, the dimension of the largest pores decreased with the scanning speed increase.

The RS evolution analysis was carried out with 9 specimens, in top and lateral surfaces. Were prepared three groups (different conditions) with 3 specimens each: as-built; after

SA (1065°C); and the other after complete standard heat treatment (SA plus DA). The RS were calculated from the strains measured by the hole-drilling strain-gage method.

For the as-built condition, uniformly distributed RS of approximately 400 MPa were found at the top surface. On the lateral surface the RS showed anisotropic distribution, in the range of 600 to 800 MPa in the build direction (vertically) and 200 to 300 MPa in the horizontal. This anisotropy was attributed to the layer-by-layer approach of depositing hot material in much colder previous built layers.

Regarding the specimens in the SA condition, the RS magnitude decreased greatly to values of 50 to 100 MPa on the top surface and 50 – 200 MPa on the lateral surface. It was attributed to the high temperature of the heat treatment, 1065°C, which relieved the plastic strains and promoted slight grain growth, visually observed. The microstructure analysis revealed series of carbide presence, distributed randomly, at the grain boundaries. This was attributed to be the reason for the oscillations noticed in the RS magnitude at different depths. The detected carbides were enriched in Ni, Mo and Ti.

Lastly, the SA plus DA specimens showed RS values of 10 – 50 MPa at middle depth. The oscillations were again observed, and similar carbides were detected again. Also, needle-like Delta phase particles were identified at the grain boundaries. Both heat-treated set of specimens showed compressive RS at immediately near the surface. It can be related to the heat treatment and the cooling after removing from the furnace, as the exterior cools faster than the interior. Those compressive stresses are beneficial for the fatigue life of the parts.

5.2 PROPOSALS OF FUTURE WORKS

As this work has been finished a few topics are suggested for future works. In the literature review has been stated that the individual process parameters can have different behaviors depending on the material being used and the majority of the works related to this topic are carried out with other materials than IN718. Thereby, it would be interesting to study the influence of the LPBF process parameters on parts fabricated with the IN718 powder. A few suggestions are:

- Study the laser power and the layer thickness influence on the porosity, as they have been kept constant for all combinations of process parameters;
- Study the effect of scanning speeds higher than 800 mm/s, as this scanning speed was determined to be the optimal and no higher speeds were used;
- Address different methodologies and techniques in order to try to verify if there is a relation between the VED and the porosity.

Very few works exist about the RS evaluation of LPBF-ed IN718 parts. Moreover, the works that exist only measure surface RS. No works related to the hole-drilling strain-

gage method applied to LPBF-ed IN718 were found. A few suggestions of future works regarding the RS evaluation are:

- Study the RS evolution of different heat treatments and using different temperatures, for example, SA at 980°C or water quenching instead of air cooling;
- Study the carbides detected in the heat-treated condition that contributed to the RS oscillation;
- Carry out a study to confirm or determine the cause of the compressive RS at immediately near the surface.

REFERENCES AND OTHER SOURCES OF INFORMATION

5.1 BOOKS, SCIENTIFIC PAPERS, INTERNATIONAL STANDARDS AND WEBSITES

6 REFERENCES AND OTHER SOURCES OF INFORMATION

6.1 BOOKS, SCIENTIFIC PAPERS, INTERNATIONAL STANDARDS AND WEBSITES

"Aerospace: RUAG." (n.d.). Aerospace: RUAG - Additive Manufacturing of Satellite Components. Retrieved May 6, 2019, from EOS website: https://www.eos.info/case_studies/additive-manufacturing-of-antenna-bracket-for-satellite

Ahmad, B., Veen, S. O. Van Der, Fitzpatrick, M. E., & Guo, H. (2018). Residual Stress Evaluation in Selective-Laser-Melting Additively Manufactured Titanium (Ti-6Al-4V) and Inconel 718 using the Contour Method and Numerical Simulation. *Additive Manufacturing*, *22*, 571–582. https://doi.org/10.1016/j.addma.2018.06.002

Ajovalasit, A., Scafidi, M., Zuccarello, B., Beghini, M., Bertini, L., Santus, C., … Bertelli, L. (2010). *The Hole-Drilling Strain Gauge Method for the Measurement of Uniform or Non-Uniform Residual Stresses*.

Alabort, E., Barba, D., & Reed, R. C. (2019). Design of Metallic Bone by Additive Manufacturing. *Scripta Materialia*, *164*, 110–114. https://doi.org/10.1016/j.scriptamat.2019.01.022

Ålgårdh, J., Strondl, A., Karlsson, S., Farre, S., Joshi, S., Andersson, J., … Ågren, J. (2017). *State-of-the-Art for Additive Manufacturing of Metals*. Retrieved from http://www.metalliskamaterial.se/globalassets/3-forskning/rapporter/2016-03898---state-of-the-art-for-additive-manufacturing-of-metals-2_1.pdf

Allaire, G., Dapogny, C., Faure, A., & Michailidis, G. (2017). Shape Optimization of a Layer by Layer Mechanical Constraint for Additive Manufacturing. *Comptes Rendus Mathematique*, *355*(6), 699–717. https://doi.org/10.1016/j.crma.2017.04.008

Amato, K. N., Gaytan, S. M., Murr, L. E., Martinez, E., Shindo, P. W., Hernandez, J., … Medina, F. (2012). Microstructures and Mechanical Behavior of Inconel 718 Fabricated by Selective Laser Melting. *Acta Materialia*, *60*(5), 2229–2239. https://doi.org/10.1016/j.actamat.2011.12.032

"ANALYTICAL BCA SERIES." (n.d.). ANALYTICAL BCA SERIES. Retrieved October 28, 2019, from ORMA website: http://www.ormascientific.com/portfolio-articoli/analytical-bca-series/?lang=en

"Applications for metal AM." (n.d.). Applications for Metal Additive Manufacturing Technology. Retrieved May 6, 2019, from METAL AM website: https://www.metal-am.com/introduction-to-metal-additive-manufacturing-and-3d-printing/applications-for-additive-manufacturing-technology/

"Arcam History." (n.d.). Arcam History. Retrieved May 6, 2019, from Arcam EBM website: http://www.arcam.com/company/about-arcam/history/

ASTM. (2013). Standard Test Method for Determining Residual Stresses by the Hole-Drilling Strain-Gage Method (E837-13a). *ASTM International*. Retrieved from https://www.astm.org/Standards/E837.htm

ASTM. (2014). Standard Specification for Additive Manufacturing Nickel Alloy (UNS N07718) with Powder Bed Fusion (ASTM F3055-14a). *ASTM International*. Retrieved from https://www.astm.org/Standards/F3055.htm

ASTM. (2017). Standard Test Method for Density of Powder Metallurgy (PM) Materials Containing Less Than Two Percent Porosity (ASTM B311-17). *ASTM International*. Retrieved from https://www.astm.org/Standards/B311.htm

Badiru, A. B., Valencia, V. V., & Liu, D. (2017). Additive Manufacturing Handbook - Product Development for the Defense Industry - 16.2 Powder Bed Fusion. *CRC Press*, 263–274. Retrieved from https://app.knovel.com/hotlink/pdf/id:kt011MFQL4/additive-manufacturing/powder-bed-fusion

Bai, Y., & Williams, C. B. (2015). An Exploration of Binder Jetting of Copper. *Rapid Prototyping Journal*, *21*(2), 177–185. https://doi.org/10.1108/RPJ-12-2014-0180

Bandyopadhyay, A., & Traxel, K. D. (2018). Invited Review Article: Metal-Additive Manufacturing - Modeling Strategies for Application-Optimized Designs. *Additive*

Manufacturing, *22*, 758–774. https://doi.org/10.1016/j.addma.2018.06.024
Bartlett, J. L., & Li, X. (2019). An Overview of Residual Stresses in Metal Powder Bed Fusion. *Additive Manufacturing*, *27*, 131–149. https://doi.org/10.1016/j.addma.2019.02.020
Bhatt, P. M., Kabir, A. M., Peralta, M., Bruck, H. A., & Gupta, S. K. (2019). A Robotic Cell for Performing Sheet Lamination-Based Additive Manufacturing. *Additive Manufacturing*, *27*, 278–289. https://doi.org/10.1016/j.addma.2019.02.002
Bourell, D., Kruth, J. P., Leu, M., Levy, G., Rosen, D., Beese, A. M., & Clare, A. (2017). Materials for Additive Manufacturing. *CIRP Annals - Manufacturing Technology*, *66*(2), 659–681. https://doi.org/10.1016/j.cirp.2017.05.009
Braian, M., Jönsson, D., Kevci, M., & Wennerberg, A. (2018). Geometrical Accuracy of Metallic Objects Produced with Additive or Subtractive Manufacturing: A Comparative in Vitro Study. *Dental Materials*, *34*(7), 978–993. https://doi.org/10.1016/j.dental.2018.03.009
Burton, H. E., Eisenstein, N. M., Lawless, B. M., Jamshidi, P., Segarra, M. A., Addison, O., … Cox, S. C. (2019). The Design of Additively Manufactured Lattices to Increase the Functionality of Medical Implants. *Materials Science and Engineering C*, *94*, 901–908. https://doi.org/10.1016/j.msec.2018.10.052
Cao, G. H., Sun, T. Y., Wang, C. H., Li, X., Liu, M., Zhang, Z. X., … Russell, A. M. (2018). Investigations of γ ′ , γ ″ and δ Precipitates in Heat-Treated Inconel 718 Alloy Fabricated by Selective Laser Melting. *Materials Characterization*, *136*, 398–406. https://doi.org/10.1016/j.matchar.2018.01.006
Casavola, C., Campanelli, S. L., & Pappalettere, C. (2009). Preliminary Investigation on Distribution of Residual Stress Generated by the Selective Laser Melting Process. *The Journal of Strain Analysis for Engineering Design*, *44*(1), 93–104. https://doi.org/10.1243/03093247JSA464
Chlebus, E., Gruber, K., Kuźnicka, B., Kurzac, J., & Kurzynowski, T. (2015). Effect of Heat Treatment on the Microstructure and Mechanical Properties of Inconel 718 Processed by Selective Laser Melting. *Materials Science and Engineering A*, *639*, 647–655. https://doi.org/10.1016/j.msea.2015.05.035
Chow, S.-C. (2018). *Evaluation of Laser Powder Bed Fusion (LPBF) Fabricated A356 (Al7SiMg) Components Through Finite Element Analysis* (Master's Thesis, McGill University, Department of Mining and Materials Engineering). Retrieved from http://digitool.library.mcgill.ca/webclient/StreamGate?folder_id=0&dvs=1547135990710~414
"CNC Wire Cut EDM." (n.d.). CNC Wire Cut EDM DK7732. Retrieved October 28, 2019, from Suzhou Baoma Numerical Control Equipment website: https://www.bmedm.com/economical-type1/729.html
Concept Laser. (2018). *Mlab Cusing R: Metal Laser Melting System (datasheet)*. Retrieved from https://www.concept-laser.de/en/products/machines.html
Cottam, R., & Wang, J. (2014). Characterization of Microstructure and Residual Stress in a 3D H13 Tool Steel Component Produced by Additive Manufacturing. *Materials Research Society*, *29*(17), 1978–1986. https://doi.org/10.1557/jmr.2014.190
DebRoy, T., Wei, H. L., Zuback, J. S., Mukherjee, T., Elmer, J. W., Milewski, J. O., … Zhang, W. (2018). Additive Manufacturing of Metallic Components – Process, Structure and Properties. *Progress in Materials Science*, *92*, 112–224. https://doi.org/10.1016/j.pmatsci.2017.10.001
Deng, D., Peng, R. L., Brodin, H., & Moverare, J. (2018). Microstructure and Mechanical Properties of Inconel 718 Produced by Selective Laser Melting: Sample Orientation Dependence and Effects of Post Heat Treatments. *Materials Science and Engineering A*, *713*, 294–306. https://doi.org/10.1016/j.msea.2017.12.043
DuPont, J. N., Lippold, J. C., & Kiser, S. D. (2009). *Welding Metallurgy and Weldability of Nickel-Base Alloys - 1. Introduction*. Retrieved from https://app.knovel.com/hotlink/pdf/id:kt00CR5SB5/welding-metallurgy-weldability/introduction
EOS. (2014). NickelAlloy IN718 (datasheet). Retrieved November 20, 2019, from https://www.eos.info/eos-nickelalloy-in718-nickel-alloy-for-aerospace-and-industry-d64f5c43276f3673

Ford, S., & Despeisse, M. (2016). Additive Manufacturing and Dustainability: An Exploratory Study of the Advantages and Challenges. *Journal of Cleaner Production*, *137*, 1573–1587. https://doi.org/10.1016/j.jclepro.2016.04.150

Fujii, H. T., Shimizu, S., Sato, Y. S., & Kokawa, H. (2016). High-Strain-Rate Deformation in Ultrasonic Additive Manufacturing. *Scripta Materialia*, *135*, 125–129. https://doi.org/10.1016/j.scriptamat.2016.12.030

Galati, M., & Iuliano, L. (2018). A Literature Review of Powder-Based Electron Beam Melting Focusing on Numerical Simulations. *Additive Manufacturing*, *19*, 1–20. https://doi.org/10.1016/j.addma.2017.11.001

"GE Additive machines." (n.d.). GE Additive machines - Direct Metal Laser Melting (DMLM) machines. Retrieved October 28, 2019, from GE Additive website: https://www.ge.com/additive/additive-manufacturing/machines/dmlm-machines/mlab-r

"GE Reveals How." (2017). GE Reveals How Greg Morris Created the 3D Printed Nozzle for the LEAP Jet Engine. Retrieved May 6, 2019, from 3D Printing Media Network website: https://www.3dprintingmedia.network/ge-reveals-greg-morris-created-3d-printed-nozzle-leap-jet-engine/

Ghosh, S., & Choi, J. (2007). Deposition Pattern Based Thermal Stresses in Single-Layer Laser Aided Direct Material Deposition Process. *Journal of Manufacturing Science and Engineering*, *129*, 319–332. https://doi.org/10.1115/1.2401620

Gibson, I., & Khorasani, A. M. (2019). Metallic Additive Manufacturing: Design, Process, and Post-Processing. *Metals*, *9*(2), 137:1–137:2. https://doi.org/10.3390/met9020137

Gibson, I., Rosen, D. W., & Stucker, B. (2010). *Additive Manufacturing Technologies - Rapid Prototyping to Direct Digital Manufacturing*. https://doi.org/10.1007/978-1-4419-1120-9

Goehrke, S. (2018). Additive Manufacturing is Driving the Future of the Automotive Industry. Retrieved May 7, 2019, from Forbes website: https://www.forbes.com/sites/sarahgoehrke/2018/12/05/additive-manufacturing-is-driving-the-future-of-the-automotive-industry/#61d8d24775cc

Hehr, A., & Dapino, M. J. (2017). Dynamics of Ultrasonic Additive Manufacturing. *Ultrasonics*, *73*, 49–66. https://doi.org/10.1016/j.ultras.2016.08.009

Herzog, D., Seyda, V., Wycisk, E., & Emmelmann, C. (2016). Additive Manufacturing of Metals. *Acta Materialia*, *117*, 371–392. https://doi.org/10.1016/j.actamat.2016.07.019

Holland, S., Wang, X., Fang, X. Y., Guo, Y. B., Yan, F., & Li, L. (2018). Grain Boundary Network Evolution in Inconel 718 from Selective Laser Melting to Heat Treatment. *Materials Science and Engineering A*, *725*, 406–418. https://doi.org/10.1016/j.msea.2018.04.045

"IPA 30/40." (n.d.). IPA 30/40. Retrieved August 13, 2019, from Remet website: http://www.remet.it/?p=2077&lang=en

ISO/ASTM. (2015). Standard Terminology for Additive Manufacturing Technologies - General Principles - Terminology (ISO/ASTM 52900:2015(E)). *ISO/ASTM International*. Retrieved from https://www.iso.org/standard/69669.html

"IsoMet™ 4000." (n.d.). IsoMet™ 4000 & 5000 Linear Precision Saws. Retrieved October 28, 2019, from Buehler website: https://www.buehler.com/Brochures/English/Sectioning/IsoMet4000_5000.pdf

Jia, Q., & Gu, D. (2014). Selective Laser Melting Additive Manufacturing of Inconel 718 Superalloy Parts: Densification, Microstructure and Properties. *Journal of Alloys and Compounds*, *585*, 713–721. https://doi.org/10.1016/j.jallcom.2013.09.171

"K-RY61-1.5/120R." (n.d.). K-RY61-1.5/120R. Retrieved August 23, 2019, from SINT Technology website: https://www.mts3000.com/product/k-ry61-1-5-120r/

Khodabakhshi, F., & Gerlich, A. P. (2018). Potentials and Strategies of Solid-State Additive Friction-Stir Manufacturing Technology: A Critical Review. *Journal of Manufacturing Processes*, *36*, 77–92. https://doi.org/10.1016/j.jmapro.2018.09.030

"Learn how LENS systems." (n.d.). Learn How LENS Systems Enable the Repair of Blisks and Other Aircraft Engine Components - Blisk Repair. Retrieved May 6, 2019, from

Optomec website: https://www.optomec.com/3d-printed-metals/lens-emerging-applications/blisk-repair/

Levy, A., Miriyev, A., Sridharan, N., Han, T., Tuval, E., Babu, S. S., … Frage, N. (2018). Ultrasonic Additive Manufacturing of Steel: Method, Post-processing Treatments and Properties. *Journal of Materials Processing Technology*, *256*, 183–189. https://doi.org/10.1016/j.jmatprotec.2018.02.001

Li, J., Zhao, Z., Bai, P., Qu, H., Liu, B., Li, L., … Guo, Z. (2019). Microstructural Evolution and Mechanical Properties of IN718 Alloy Fabricated by Selective Laser Melting Following Different Heat Treatments. *Journal of Alloys and Compounds*, *772*, 861–870. https://doi.org/10.1016/j.jallcom.2018.09.200

Li, N., Huang, S., Zhang, G., Qin, R., Liu, W., Xiong, H., … Blackburn, J. (2019). Progress in Additive Manufacturing on New Materials: A Review. *Journal of Materials Science and Technology*, *35*(2), 242–269. https://doi.org/10.1016/j.jmst.2018.09.002

Li, X., Shi, J. J., Wang, C. H., Cao, G. H., Russell, A. M., Zhou, Z. J., … Chen, G. F. (2018). Effect of Heat Treatment on Microstructure Evolution of Inconel 718 Alloy Fabricated by Selective Laser Melting. *Journal of Alloys and Compounds*, *764*, 639–649. https://doi.org/10.1016/j.jallcom.2018.06.112

Liu, F., Mao, Z., Zhang, P., Zhang, D. Z., Jiang, J., & Ma, Z. (2018). Functionally Graded Porous Scaffolds in Multiple Patterns: New Design Method, Physical and Mechanical Properties. *Materials and Design*, *160*, 849–860. https://doi.org/10.1016/j.matdes.2018.09.053

Liu, Y., Yang, Y., & Wang, D. (2016). A Study on the Residual Stress During Selective Laser Melting (SLM) of Metallic Powder. *The International Journal of Advanced Manufacturing Technology*, *87*(1–4), 647–656. https://doi.org/10.1007/s00170-016-8466-y

Livescu, V., Knapp, C. M., Gray, G. T., Martinez, R. M., Morrow, B. M., & Ndefru, B. G. (2018). Additively Manufactured Tantalum Microstructures. *Materialia*, *1*, 15–24. https://doi.org/10.1016/j.mtla.2018.06.007

"Major 3D Printing investments." (2018). Major 3D Printing Investments Made by Large Companies in 2018. Retrieved August 29, 2019, from Beamler website: https://www.beamler.com/major-3d-printing-investments-large-companies/

McCue, T. J. (2018). Wohlers Report 2018: 3D Printer Industry Tops $7 Billion. Retrieved August 29, 2019, from Forbes website: https://www.forbes.com/sites/tjmccue/2018/06/04/wohlers-report-2018-3d-printer-industry-rises-21-percent-to-over-7-billion/#7fb82e3c2d1a

McCue, T. J. (2019). Significant 3D Printing Forecast Surges to $35.6 Billion. Retrieved August 29, 2019, from Forbes website: https://www.forbes.com/sites/tjmccue/2019/03/27/wohlers-report-2019-forecasts-35-6-billion-in-3d-printing-industry-growth-by-2024/#85600fc7d8a6

Micro-Measurements. (2010). *Measurement of Residual Stresses by the Hole-Drilling Strain-Gage Method (Tech Note TN-503, doc. no. 11053)*. Retrieved from https://intertechnology.com/Vishay/pdfs/TechNotes_TechTips/TN-503.pdf

Mostafa, A., Picazo Rubio, I., Brailovski, V., Jahazi, M., & Medraj, M. (2017). Structure, Texture and Phases in 3D Printed IN718 Alloy Subjected to Homogenization and HIP Treatments. *Metals*, *7*(8), 315. https://doi.org/10.3390/met7080315

Mostafaei, A., De Vecchis, P. R., Buckenmeyer, M. J., Wasule, S. R., Brown, B. N., & Chmielus, M. (2019). Microstructural Evolution and Resulting Properties of Differently Sintered and Heat-Treated Binder Jet 3D Printed Stellite 6. *Materials Science and Engineering: C*, *102*, 276–288. https://doi.org/10.1016/j.msec.2019.04.011

Mostafaei, A., Stevens, E. L., Ference, J. J., Schmidt, D. E., & Chmielus, M. (2018). Binder Jetting of a Complex-Shaped Metal Partial Fenture Framework. *Additive Manufacturing*, *21*, 63–68. https://doi.org/10.1016/j.addma.2018.02.014

Moussaoui, K., Rubio, W., Mousseigne, M., Sultan, T., & Rezai, F. (2018). Effects of Selective Laser Melting Additive Manufacturing Parameters of Inconel 718 on Porosity, Microstructure and Mechanical Properties. *Materials Science and Engineering A*, *735*, 182–190. https://doi.org/10.1016/j.msea.2018.08.037

"Nabertherm RHTC." (n.d.). Nabertherm RHTC 80-710/15/P330 Horizontal Tube

Furnace. Retrieved October 28, 2019, from https://www.coleparmer.in/i/nabertherm-rhtc-80-710-15-p330-horizontal-tube-furnace-42-1-8-tube-length-1500-c-208-240-vac/3333436

Nadammal, N., Cabeza, S., Mishurova, T., Thiede, T., Kromm, A., Seyfert, C., … Bruno, G. (2017). Effect of Hatch Length on the Development of Microstructure, Texture and Residual Stresses in Selective Laser Melted Superalloy Inconel 718. *Materials & Design*, *134*, 139–150. https://doi.org/10.1016/j.matdes.2017.08.049

"New manufacturing milestone." (2018). New Manufacturing Milestone: 30,000 Additive Fuel Nozzles. Retrieved May 6, 2019, from GE Additive website: https://www.ge.com/additive/blog/new-manufacturing-milestone-30000-additive-fuel-nozzles

Ngo, T. D., Kashani, A., Imbalzano, G., Nguyen, K. T. Q., & Hui, D. (2018). Additive Manufacturing (3D Printing): A Review of Materials, Methods, Applications and Challenges. *Composites Part B*, *143*, 172–196. https://doi.org/10.1016/j.compositesb.2018.02.012

Niaki, M. K., Torabi, S. A., & Nonino, F. (2019). Why Manufacturers Adopt Additive Manufacturing Technologies: The Role of Sustainability. *Journal of Cleaner Production*, *222*, 381–392. https://doi.org/10.1016/j.jclepro.2019.03.019

"Norsk Titanium to Deliver." (2017). Norsk Titanium to Deliver the World's First FAA-Approved, 3D-Printed, Structural Titanium Components to Boeing. Retrieved May 6, 2019, from Additive Manufacturing website: http://additivemanufacturing.com/2017/04/10/norsk-titanium-to-deliver-the-worlds-first-faa-approved-3d-printed-structural-titanium-components-to-boeing/

O'Brien, A., & Sinnes, K. (2015). *Welding Handbook, Volume 5 - Materials and Applications, Part 2 - 10.3.8 Ultrasonic Additive Manufacturing* (9th ed.). Retrieved from https://app.knovel.com/hotlink/pdf/id:kt00CQO8G2/welding-handbook-volume/ultrasonicadditive-%0Amanufacturing

Parimi, L. L., Ravi, G., Clark, D., & Attallah, M. M. (2014). Microstructural and Texture Development in Direct Laser Fabricated IN718. *Materials Characterization*, *89*, 102–111. https://doi.org/10.1016/j.matchar.2013.12.012

"Phenom XL." (n.d.). Phenom XL Desktop SEM. Retrieved from THermo Fisher Scientific website: https://www.phenom-world.com/desktop-scanning-electron-microscopes/phenom-xl

Plessis, A., Sperling, P., Beerlink, A., Tshabalala, L., Hoosain, S., Mathe, N., & Roux, S. G. (2018). Standard Method for MicroCT-Based Additive Manufacturing Quality Control 2: Density Measurement. *MethodsX*, *5*, 1117–1123. https://doi.org/10.1016/j.mex.2018.09.006

"Politecnico at a glance." (2019). Politecnico at a Glance. Retrieved August 28, 2019, from Politecnico di Torino website: https://www.polito.it/ateneo/colpodocchio/?lang=en

Popovich, V. A., Borisov, E. V., Popovich, A. A., Sufiiarov, V. S., Masaylo, D. V., & Alzina, L. (2017). Impact of Heat Treatment on Mechanical Behaviour of Inconel 718 Processed with Tailored Microstructure by Selective Laser Melting. *Materials and Design*, *131*, 12–22. https://doi.org/10.1016/j.matdes.2017.05.065

Prakash, K. S., Nancharaih, T., & Rao, V. V. S. (2018). Additive Manufacturing Techniques in Manufacturing - An Overview. *Materials Today: Proceedings*, *5*(2), 3873–3882. https://doi.org/10.1016/j.matpr.2017.11.642

Qin, Y., Wen, P., Guo, H., Xia, D., Zheng, Y., Jauer, L., … Henrich, J. (2019). Additive Manufacturing of Biodegradable Metals: Current Research Status and Future Perspectives. *Acta Biomaterialia*. https://doi.org/10.1016/j.actbio.2019.04.046

Qiu, C., Kindi, M. Al, Aladawi, A. S., & Hatmi, I. Al. (2018). A Comprehensive Study on Microstructure and Tensile Behaviour of a Selectively Laser Melted Stainless Steel. *Scientific Reports*, *8*(1), 1–16. https://doi.org/10.1038/s41598-018-26136-7

"Resinoid cut-off wheels." (n.d.). Resinoid cut-off wheels Type AO ⌀ 125 x 0,5 x 12,7 mm. Retrieved October 28, 2019, from PRESI website: https://www.presi.com/en/product/boite-de-10-disques-de-tronconnage-resinoides-standards-type-ao-o-125-mm/

"Restan MTS3000." (n.d.). Restan MTS3000. Retrieved August 6, 2019, from SINT

Technology website: https://www.mts3000.com/typical-configurations/
SAE. (2016). Nickel Alloy, Corrosion and Heat Resistant, Bars, Forgings, and Rings 52.5Ni 19Cr 3.0Mo 5.1Cb 0.90Ti 0.50Al 18Fe, Consumable Electrode or Vacuum Induction Melted 1775°F (968°C) Solution Heat Treated, Precipitation Hardenable (AMS5662). *SAE International*. Retrieved from https://www.sae.org/standards/content/ams5662/
SAE. (2017). Nickel Alloy, Corrosion and Heat Resistant, Bars, Forgings, and Rings, 52.5Ni - 19Cr - 3.0Mo - 5.1Cb - 0.90Ti - 0.50Al - 18Fe, Consumable Electrode or Vacuum Induction Melted, 1950 °F (1066 °C) Solution Heat Treated, Precipitation Hardenable (AMS5664). *SAE International*. Retrieved from https://www.sae.org/standards/content/ams5664/
Salmi, A., & Atzeni, E. (2017). History of Residual Stresses During the Production Phases of AlSi10Mg Parts Processed by Powder Bed Additive Manufacturing Technology. *Virtual and Physical Prototyping*, *12*(2), 153–160. https://doi.org/10.1080/17452759.2017.1310439
Schmidt, M., Merklein, M., Bourell, D., Dimitrov, D., Hausotte, T., Wegener, K., … Levy, G. N. (2017). Laser Based Additive Manufacturing in Industry and Academia. *CIRP Annals - Manufacturing Technology*, *66*(2), 561–583. https://doi.org/10.1016/j.cirp.2017.05.011
Sharma, A., Bandari, V., Ito, K., Kohama, K., Ramji, R. M., & Himasekhar, H. S. (2017). A New Process for Design and Manufacture of Tailor-Made Functionally Graded Composites Through Friction Stir Additive Manufacturing. *Journal of Manufacturing Processes*, *26*, 122–130. https://doi.org/10.1016/j.jmapro.2017.02.007
Sher, D. (2018). Windows OS Frustum GENERATE Launches to Further Open Up Generative Design for AM. Retrieved April 10, 2019, from 3D Printing Media Network website: https://www.3dprintingmedia.network/windows-os-frustum-generate-launches-to-further-open-up-generative-design-for-am/
SINT Technology. (n.d.-a). *MTS3000 - Restan - Automatic System for Residual Stress Measurement by Hole-Drilling (datasheet)*.
SINT Technology. (n.d.-b). *SINT EVAL - Software for Measuring Residual Stress by the Hole-Drilling Method (manual)*.
Slotwinski, J. A., Garboczi, E. J., & Hebenstreit, K. M. (2014). Porosity Measurements and Analysis for Metal Additive Manufacturing Process Control. *Journal of Research of the National Institute of Standards and Technology Porosity*, *119*, 494–528.
Solberg, K., & Berto, F. (2019). Notch-Defect Interaction in Additively Manufactured Inconel 718. *International Journal of Fatigue*, *122*, 35–45. https://doi.org/10.1016/j.ijfatigue.2018.12.021
Spierings, A. B., & Schneider, M. (2011). Comparison of Density Measurement Techniques for Additive Manufactured Metallic Parts. *Rapid Prototyping Journal*, *5*, 380–386. https://doi.org/10.1108/13552541111156504
Swain, D., Sharma, A., Selvan, S. K., Thomas, B. P., & Philip, J. (2019). Residual Stress Measurement on 3-D Printed Blocks of Using Incremental Drilling Technique. *Procedia Structural Integrity*, *14*, 337–344. https://doi.org/10.1016/j.prostr.2019.05.042
Tao, P., Li, H., Huang, B., Hu, Q., Gong, S., & Xu, Q. (2019). The Crystal Growth, Intercellular Spacing and Microsegregation of Selective Laser Melted Inconel 718 Superalloy. *Vacuum*, *159*, 382–390. https://doi.org/10.1016/j.vacuum.2018.10.074
“The EBAM 300 Series.” (2019). The EBAM® 300 Series Produces the Largest 3D Printed Metal Parts & Prototypes in the Additive Manufacturing Market. Retrieved May 2, 2019, from Sciaky website: http://www.sciaky.com/largest-metal-3d-printer-available
Tofail, S. A. M., Koumoulos, E. P., Bandyopadhyay, A., Bose, S., O’Donoghue, L., & Charitidis, C. (2018). Additive Manufacturing: Scientific and Technological Challenges, Market Uptake and Opportunities. *Materials Today*, *21*(1), 22–37. https://doi.org/10.1016/j.mattod.2017.07.001
“Transparent Clear Acrylic resin.” (n.d.). Transparent Clear Acrylic Resin. Retrieved

August 13, 2019, from PRESI website: https://www.presi.com/en/mounting-resin/173-boite-de-25-kg-de-resine-acrylique-transparente-poudre.html

Trosch, T., Strößner, J., Völkl, R., & Glatzel, U. (2016). Microstructure and Mechanical Properties of Selective Laser Melted Inconel 718 Compared to Forging and Casting. *Materials Letters*, *164*, 428–431. https://doi.org/10.1016/j.matlet.2015.10.136

Tucho, W. M., Cuvillier, P., Sjolyst-Kverneland, A., & Hansen, V. (2017). Microstructure and Hardness Studies of Inconel 718 Manufactured by Selective Laser Melting Before and After Solution Heat Treatment. *Materials Science and Engineering A*, *689*, 220–232. https://doi.org/10.1016/j.msea.2017.02.062

Varotsis, A. B. (n.d.). 3D Printing vs. CNC machining. Retrieved May 2, 2019, from 3D HUBS website: https://www.3dhubs.com/knowledge-base/3d-printing-vs-cnc-machining

Vevers, A., Kromanis, A., Gerins, E., & Ozolins, J. (2018). Additive Manufacturing and Casting Technology Comparison: Mechanical Properties, Productivity and Cost Benchmark. *Latvian Journal of Physics and Technical Sciences*, *55*(2), 56–63. https://doi.org/10.2478/lpts-2018-0013

Vrancken, B. (2016). *Study of Residual Stresses in Selective Laser Melting* (dissertation, Arenberg Doctoral School, Faculty of Engineering Science). Retrieved from https://core.ac.uk/download/pdf/45289375.pdf

Vrancken, B., Cain, V., Knutsen, R., & Humbeeck, J. Van. (2014). Residual Stress via the Contour Method in Compact Tension Specimens Produced via Selective Laser Melting. *Scripta Materialia*, *87*, 29–32. https://doi.org/10.1016/j.scriptamat.2014.05.016

Wang, X., Gong, X., & Chou, K. (2017). Review on Powder-Bed Laser Additive Manufacturing of Inconel 718 Parts. *Journal of Engineering Manufacture*, *231*(11), 1890–1903. https://doi.org/10.1177/0954405415619883

Wang, Z., Guan, K., Gao, M., Li, X., Chen, X., & Zeng, X. (2012). The Microstructure and Mechanical Properties of Deposited-IN718 by Selective Laser Melting. *Journal of Alloys and Compounds*, *513*, 518–523. https://doi.org/10.1016/j.jallcom.2011.10.107

Wohlers, T., Campbell, I., Diegel, O., Kowen, J., & Caffrey, T. (2017). *Wohlers Report 2017*. Fort Collins.

Wohlers, T., & Gornet, T. (2014). Wohlers Report 2017: History of Additive Manufacturing. *Wohlers Associate*.

Wolcott, P. J., Hehr, A., Pawlowski, C., & Dapino, M. J. (2016). Process Improvements and Characterization of Ultrasonic Additive Manufactured Structures. *Journal of Materials Processing Technology*, *233*, 44–52. https://doi.org/10.1016/j.jmatprotec.2016.02.009

"World Premiere for AM." (2018). World Premiere for Additive Manufacturing: STELIA Aerospace Presents a Demonstrator for Metallic Self-Reinforced Fuselage Pannels Manufactured by 3D Impression. Retrieved May 6, 2019, from Additive Manufacturing website: http://additivemanufacturing.com/2018/02/21/world-premiere-for-additive-manufacturing-stelia-aerospace-presents-a-demonstrator-for-metallic-self-reinforced-fuselage-pannels-manufactured-by-3d-impression/

Wu, A. S., Brown, D. W., Kumar, M., Gallegos, G. F., & King, W. E. (2014). An Experimental Investigation into Additive Manufacturing- Induced Residual Stresses in 316L Stainless Steel. *Metallurgical and Materials Transactions A*, *45*(13), 6260–6270. https://doi.org/10.1007/s11661-014-2549-x

Yadroitsev, I., & Yadroitsava, I. (2015). Evaluation of Residual Stress in Stainless Steel 316L and Ti6Al4V Samples Produced by Selective Laser Melting. *Virtual and Physical Prototyping*, *10*(2), 67–76. https://doi.org/10.1080/17452759.2015.1026045

Yan, J., Zhou, Y., Gu, R., Zhang, X., Quach, W., & Yan, M. (2019). A Comprehensive Study of Steel Powders (316L, H13, P20 and 18Ni300) for Their Selective Laser Melting Additive Manufacturing. *Metals*, *9*, 86.

Yi, J. H., Kang, J. W., Wang, T. J., Wang, X., Hu, Y. Y., Feng, T., … Feng, Y. L. (2019). Effect of Laser Energy Density on the Microstructure, Mechanical Properties, and Deformation of Inconel 718 Samples Fabricated by Selective Laser Melting. *Journal of Alloys and Compounds*, *786*, 481–488.

https://doi.org/10.1016/j.jallcom.2019.01.377
Yi, S., Liu, F., Zhang, J., & Xiong, S. (2004). Study of the Key Technologies of LOM for functional metal parts. *Journal of Materials Processing Technology*, *150*(1–2), 175–181. https://doi.org/10.1016/j.jmatprotec.2004.01.035
Yoshino, M., Obikawa, T., & Shinozuka, J. (2000). Rapid Manufacturing System by Sheet Steel Laminating Method. *Transactions of the Japan Society of Mechanical Engineers Series C*, *66*, 667–672. https://doi.org/10.1299/kikaic.66.667
Yu, H., Hayashi, S., Kakehi, K., & Kuo, Y.-L. (2018). Study of Formed Oxides in IN718 Alloy during the Fabrication by Selective Laser Melting and Electron Beam Melting. *Metals*, *9*(1), 19:1–19:15. https://doi.org/10.3390/met9010019
Yuan, L., Ding, S., & Wen, C. (2019). Additive Manufacturing Technology for Porous Metal Implant Applications and Triple Minimal Surface Structures: A Review. *Bioactive Materials*, Vol. 4, pp. 56–70. https://doi.org/10.1016/j.bioactmat.2018.12.003
Zenou, M., & Grainger, L. (2018). 3 - Additive Manufacturing of Metallic Materials. In *Additive Manufacturing* (pp. 53–103). https://doi.org/https://doi.org/10.1016/B978-0-12-812155-9.00003-7
Zhang, D., Feng, Z., Wang, C., Wang, W., Liu, Z., & Niu, W. (2018). Comparison of Microstructures and Mechanical Properties of Inconel 718 Alloy Processed by Selective Laser Melting and Casting. *Materials Science and Engineering A*, *724*(100), 357–367. https://doi.org/10.1016/j.msea.2018.03.073
Zhang, D., Niu, W., Cao, X., & Liu, Z. (2015). Effect of Standard Heat Treatment on the Microstructure and Mechanical Properties of Selective Laser Melting Manufactured Inconel 718 Superalloy. *Materials Science and Engineering A*, *644*, 32–40. https://doi.org/10.1016/j.msea.2015.06.021
Zhao, X., Liu, J., Shi, Y., Wei, Q., Han, C., Song, B., … Wen, S. (2015). Differences in Microstructure and Properties Between Selective Laser Melting and Traditional Manufacturing for Fabrication of Metal Parts: A Review. *Frontiers of Mechanical Engineering*, *10*(2), 111–125. https://doi.org/10.1007/s11465-015-0341-2
Zhao, Z., Yang, X., Li, S., & Li, D. (2019). Interfacial Bonding Features of Friction Stir Additive Manufactured Build for 2195-T8 Aluminum-Lithium Alloy. *Journal of Manufacturing Processes*, *38*, 396–410. https://doi.org/10.1016/j.jmapro.2019.01.042
Zhou, L., Mehta, A., Mcwilliams, B., Cho, K., & Sohn, Y. (2019). Microstructure, Precipitates and Mechanical Properties of Powder Bed Fused Inconel 718 Before and After Heat Treatment. *Journal of Materials Science & Technology*, *35*(6), 1153–1164. https://doi.org/10.1016/j.jmst.2018.12.006
Zuback, J. S., & DebRoy, T. (2018). The Hardness of Additively Manufactured Alloys. *Materials*, *11*(11), 2070:1–2070:41. https://doi.org/10.3390/ma11112070

ANNEXES

7 ANNEXES

7.1 ANNEX 1 – DENSITY OF THE WATER AT DIFFERENT TEMPERATURES

TABLE 3 Density of Air-Free Water[A]

Temperature (°C)	Density (g/cm^3)
18.0	0.9986
18.5	0.9985
19.0	0.9984
19.5	0.9983
20.0	0.9982
20.5	0.9981
21.0	0.9980
21.5	0.9979
22.0	0.9978
22.5	0.9976
23.0	0.9975
23.5	0.9974
24.0	0.9973
24.5	0.9972
25.0	0.9970
25.5	0.9969
26.0	0.9968
26.5	0.9966
27.0	0.9965
27.5	0.9964
28.0	0.9962
28.5	0.9961
29.0	0.9959
29.5	0.9958
30.0	0.9956

[A] *Metrological Handbook 145*, "Quality Assurance for Measurements," National Institute of Standards and Technology, 1990, p. 9.10.

Source: ASTM B311 (2017) standard

7.2 ANNEX 2 – MASS IN AIR AND MASS IN WATER SINGLE MEASUREMENTS AND AVERAGE

Table 10 – Annex 2 - Single measurements and average of mass in air and mass in water (Archimedes' method)

Specimen	m_{a1} [g]	m_{w1} [g]	m_{a2} [g]	m_{w2} [g]	m_{a3} [g]	m_{w3} [g]	m_a [g]	m_w [g]
1	6.623	5.757	6.623	5.756	6.622	5.760	6.623	5.758
2	6.647	5.791	6.647	5.791	6.647	5.790	6.647	5.791
3	6.725	5.861	6.725	5.863	6.725	5.864	6.725	5.863
4	6.853	5.988	6.853	5.988	6.853	5.989	6.853	5.988
5	6.543	5.705	6.543	5.707	6.543	5.707	6.543	5.706
6	6.823	5.965	6.823	5.967	6.823	5.965	6.823	5.966
7	6.847	5.994	6.847	5.995	6.847	5.997	6.847	5.995
8	6.722	5.876	6.722	5.879	6.722	5.880	6.722	5.878
9	6.724	5.885	6.724	5.886	6.725	5.887	6.724	5.886
10	6.743	5.899	6.743	5.903	6.743	5.904	6.743	5.902
11	6.729	5.892	6.729	5.894	6.729	5.894	6.729	5.893
12	6.748	5.921	6.748	5.912	6.748	5.910	6.748	5.914
13	6.796	5.962	6.799	5.960	6.798	5.960	6.798	5.961
14	6.796	5.958	6.795	5.956	6.795	5.957	6.795	5.957
15	6.736	5.906	6.738	5.905	6.738	5.906	6.737	5.906
16	6.818	5.974	6.817	5.975	6.818	5.975	6.818	5.975
17	6.812	5.973	6.811	5.971	6.811	5.973	6.811	5.972
18	6.760	5.923	6.759	5.923	6.760	5.923	6.760	5.923

7.3 ANNEX 3 – OPTICAL MICROSCOPY IMAGES ACQUIRED FOR MICROGRAPH-BASED METHOD

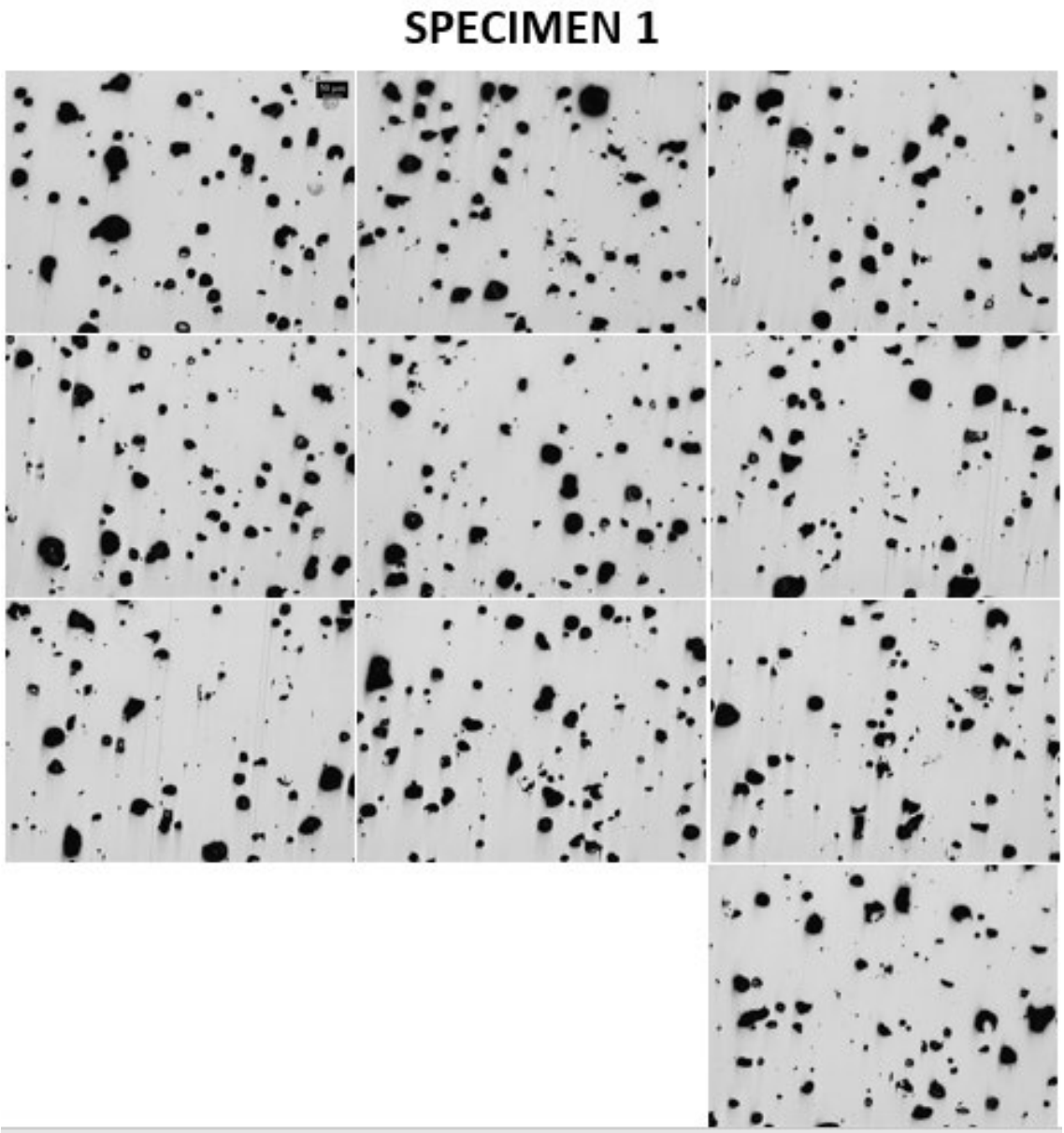

SPECIMEN 2

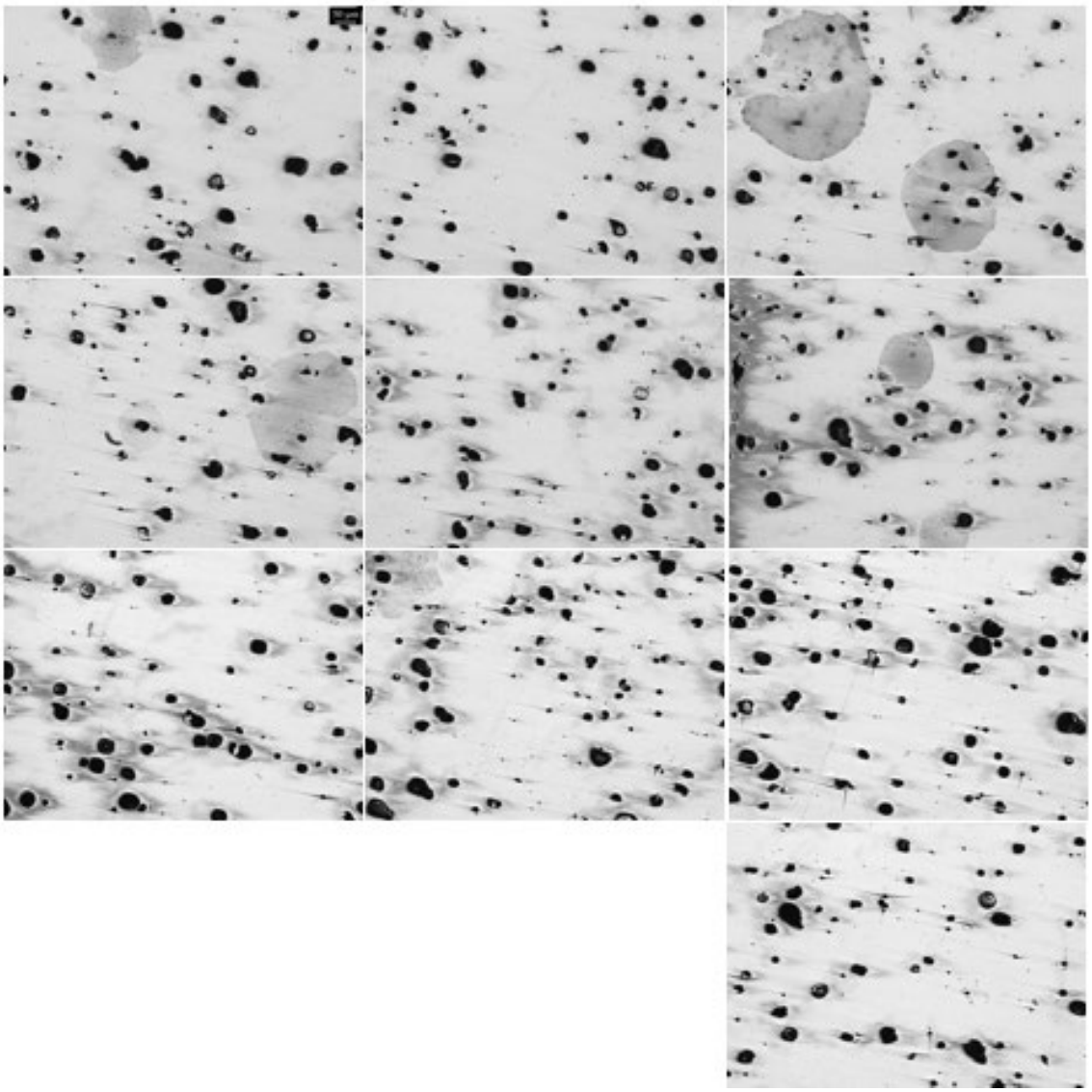

SPECIMEN 3

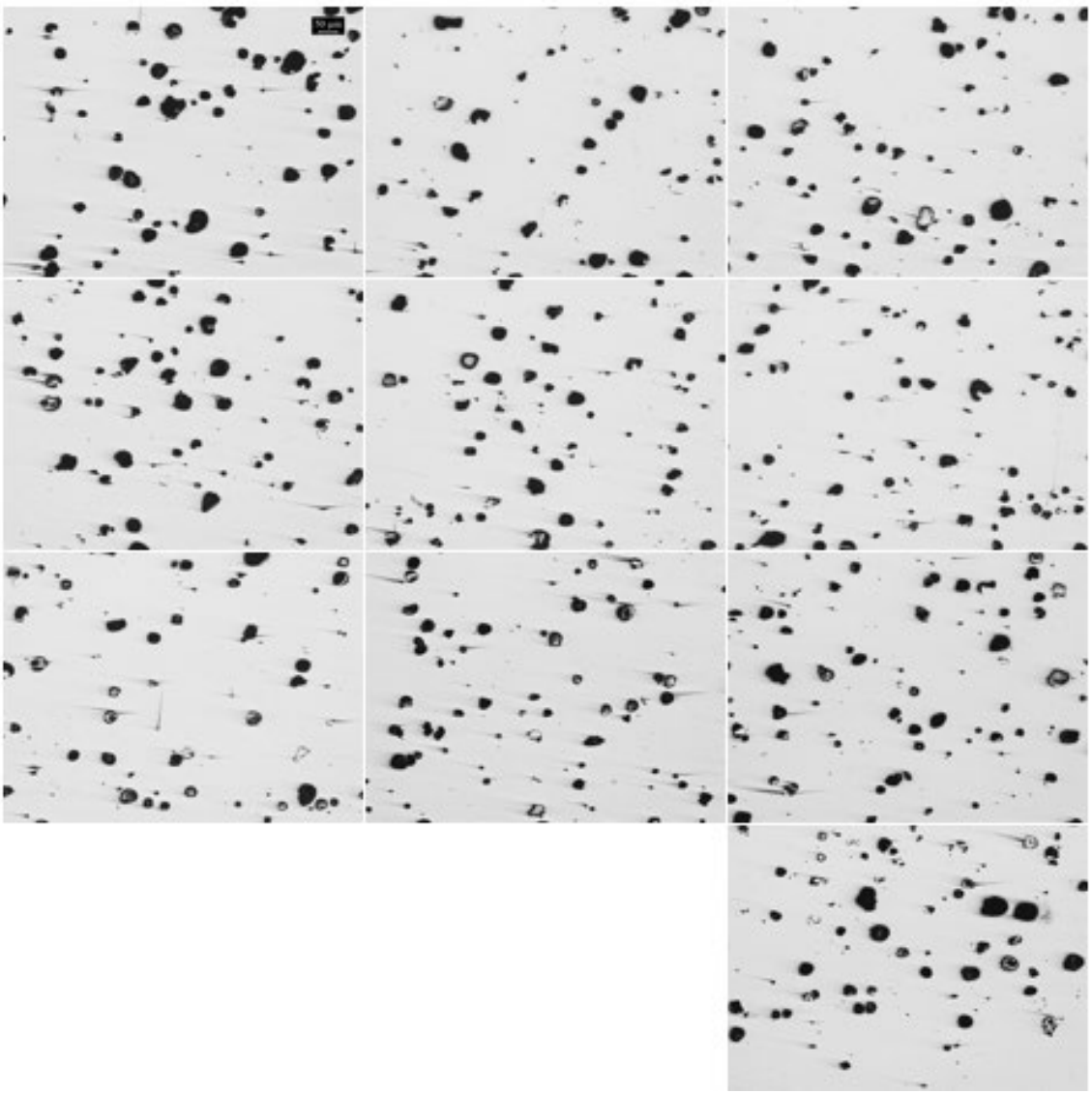

SPECIMEN 4

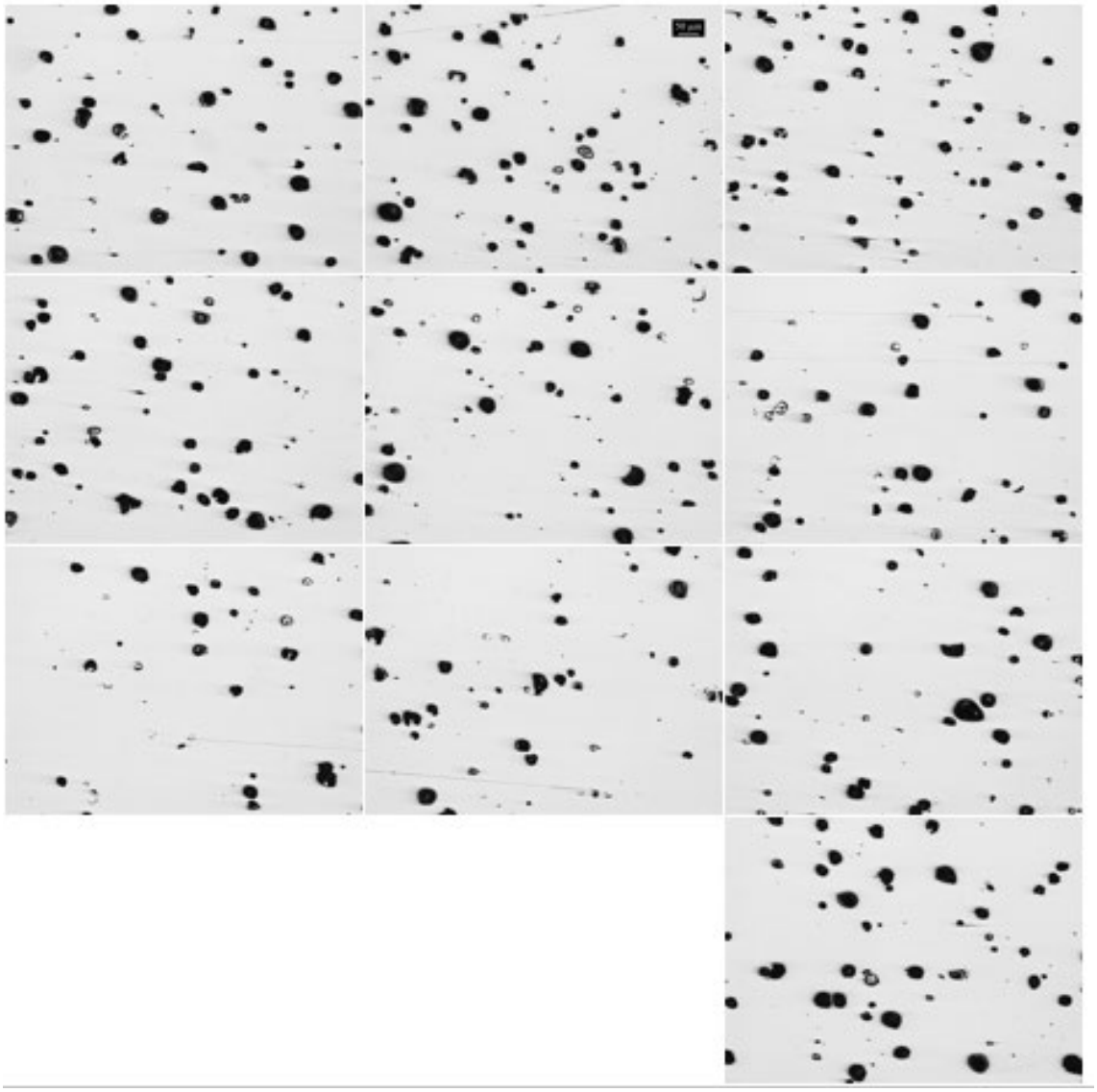

SPECIMEN 5

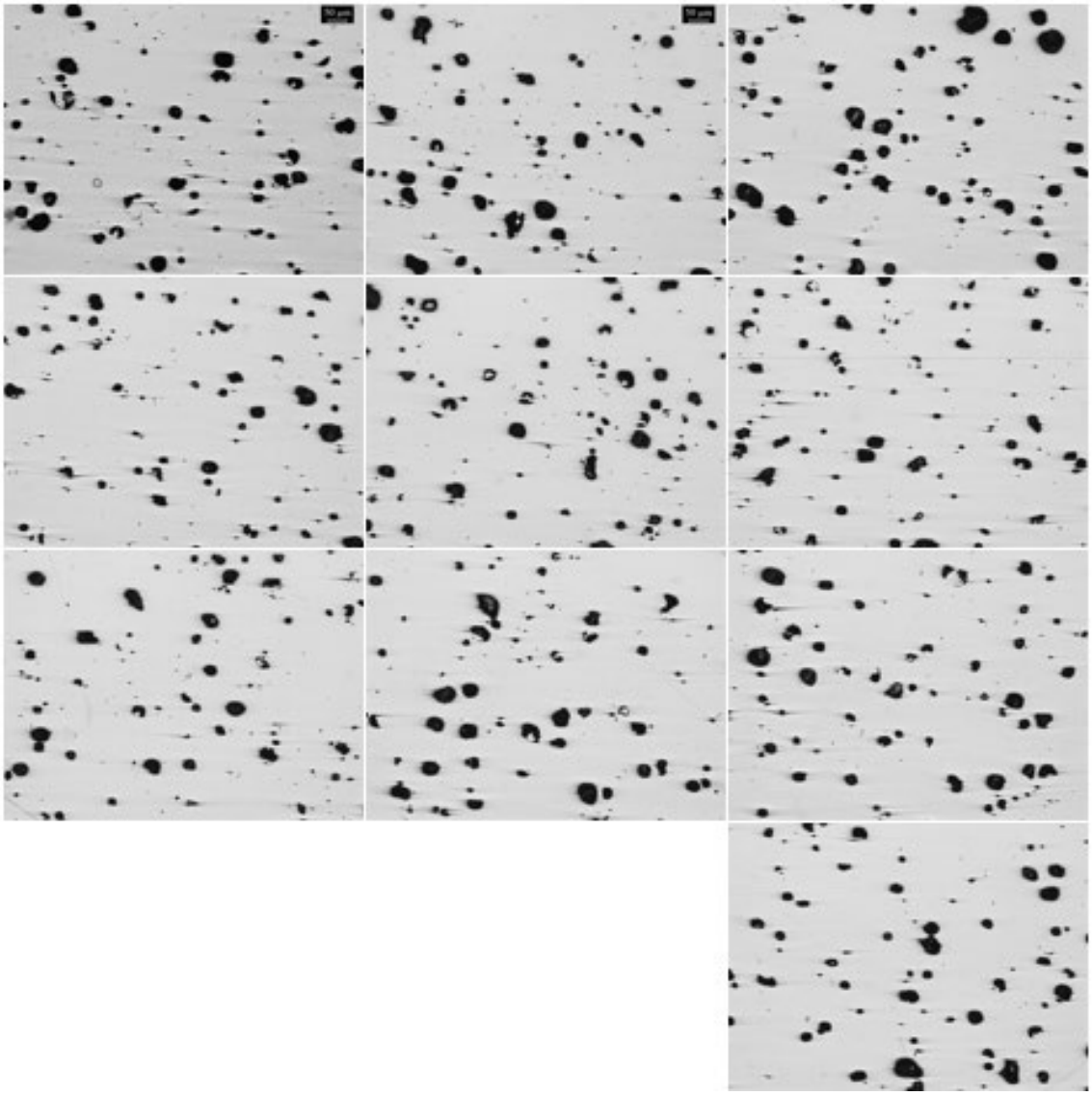

SPECIMEN 6

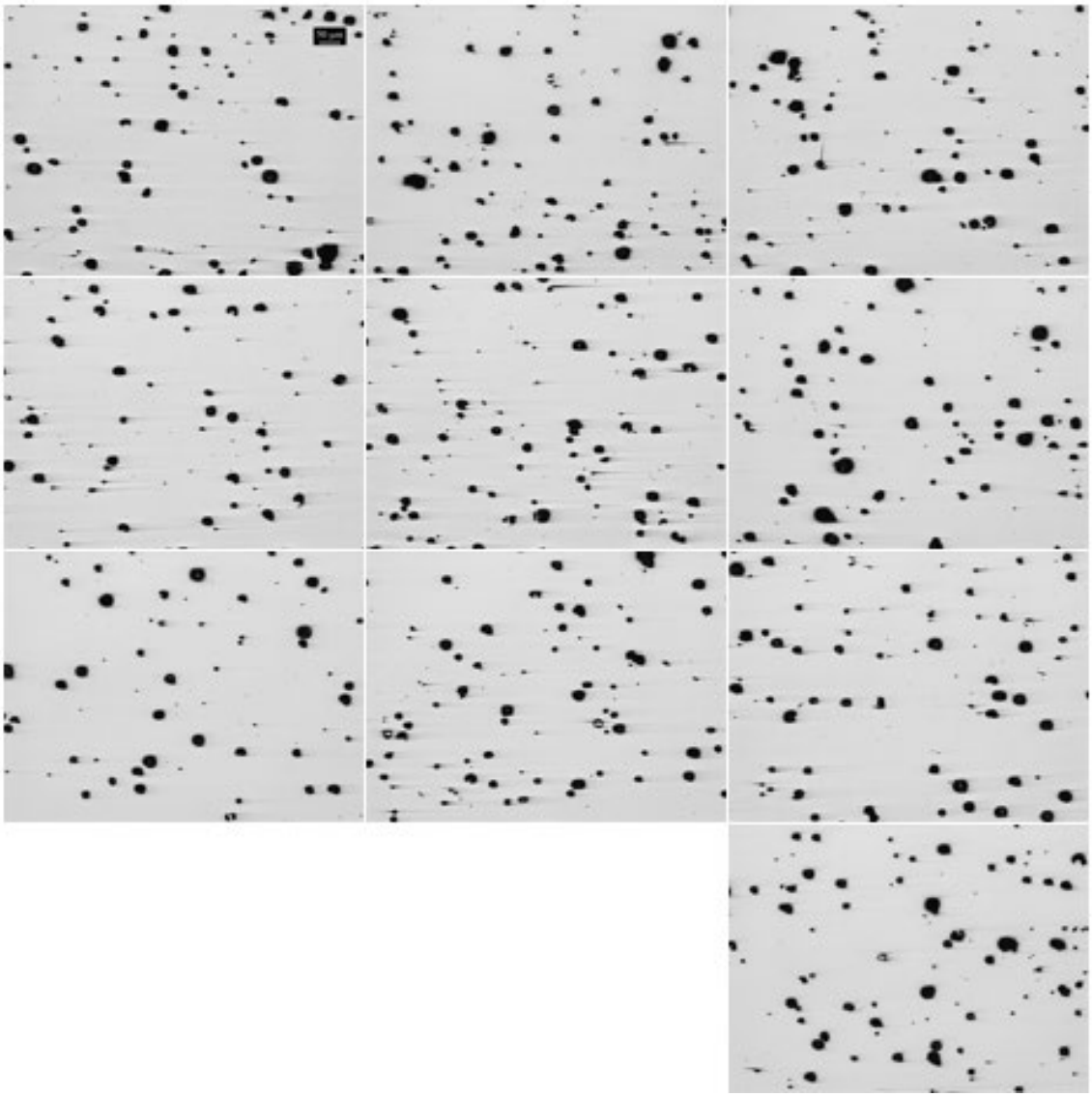

SPECIMEN 7

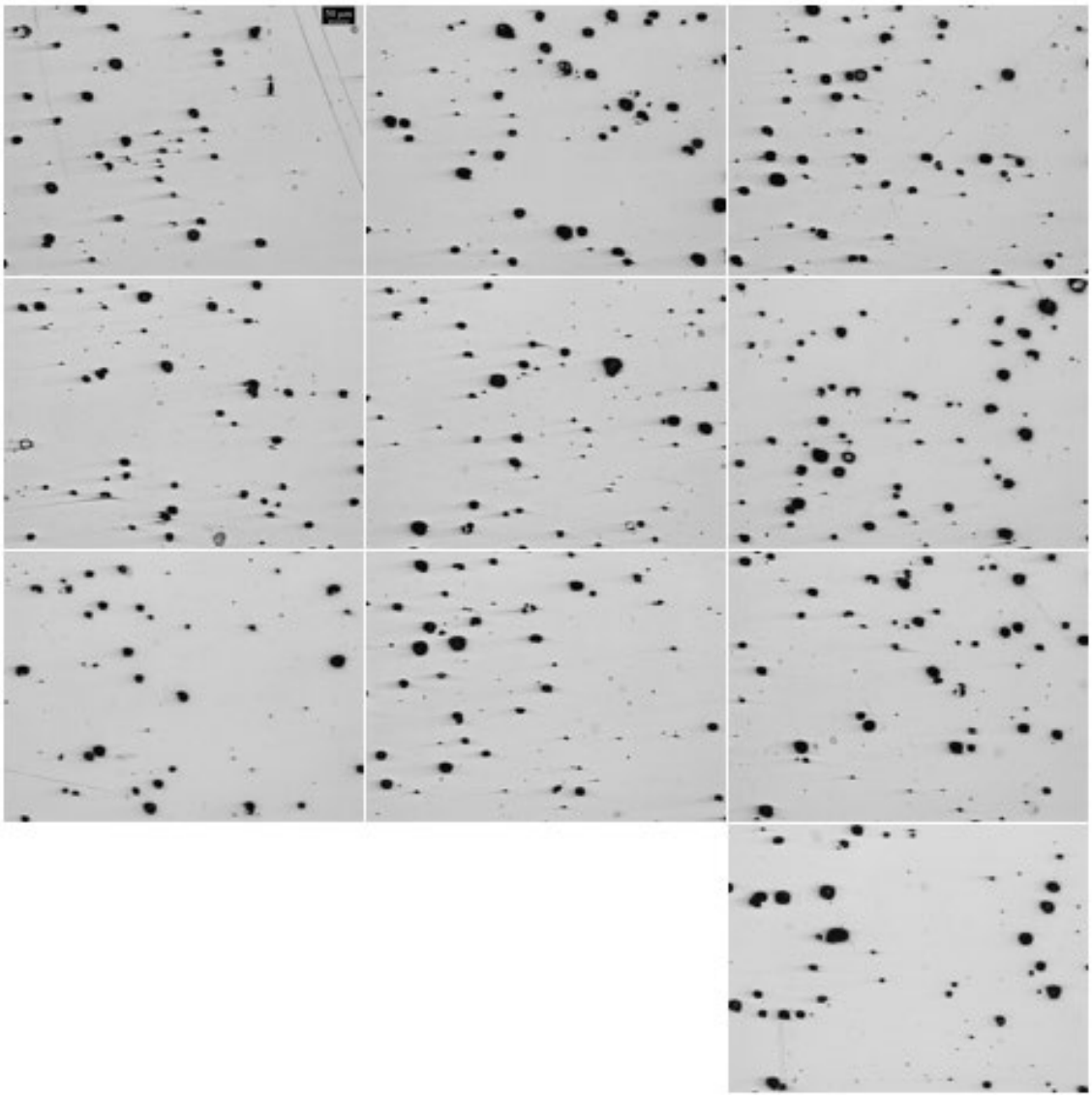

SPECIMEN 8

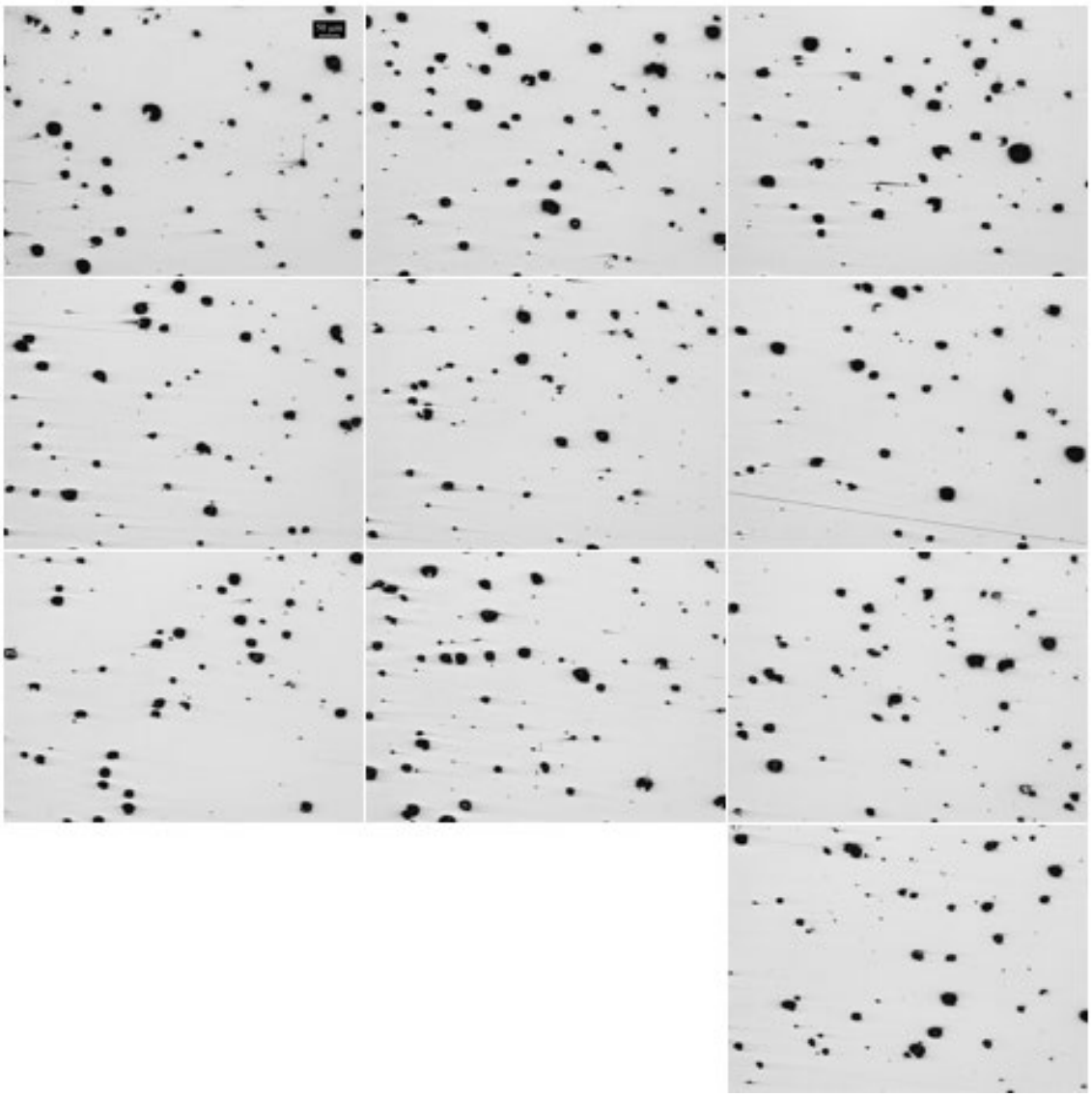

SPECIMEN 9

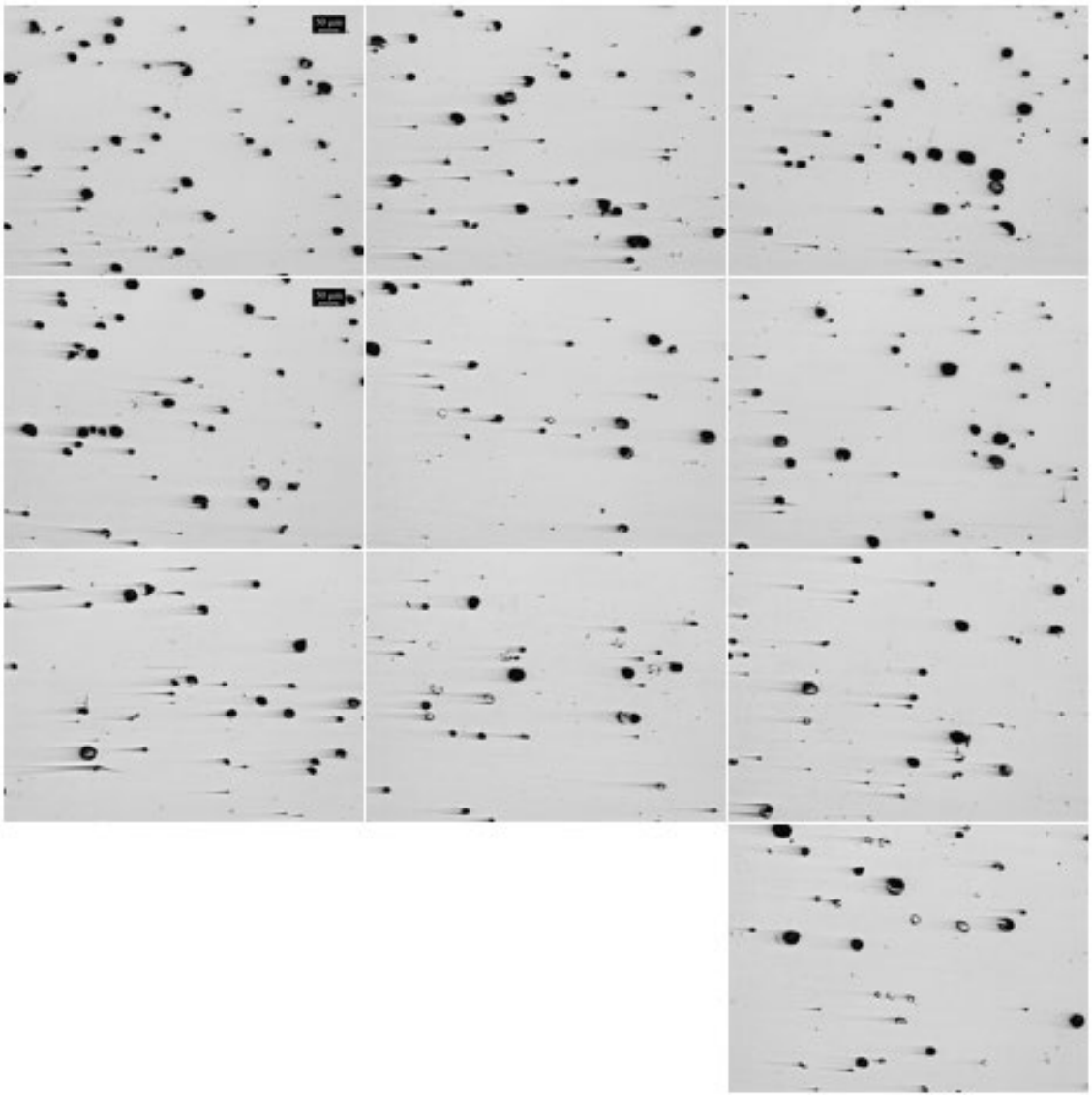

SPECIMEN 10

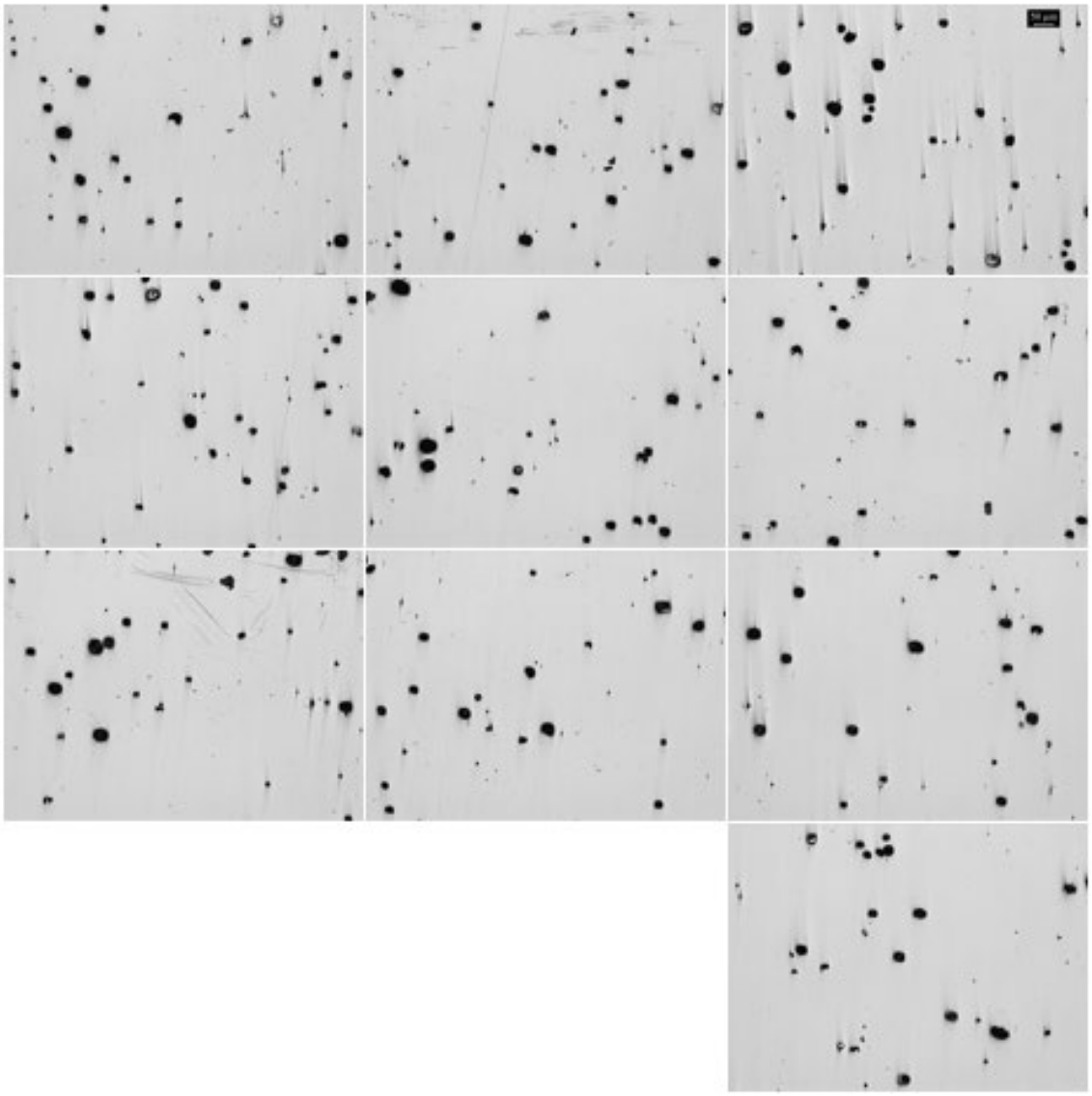

SPECIMEN 11

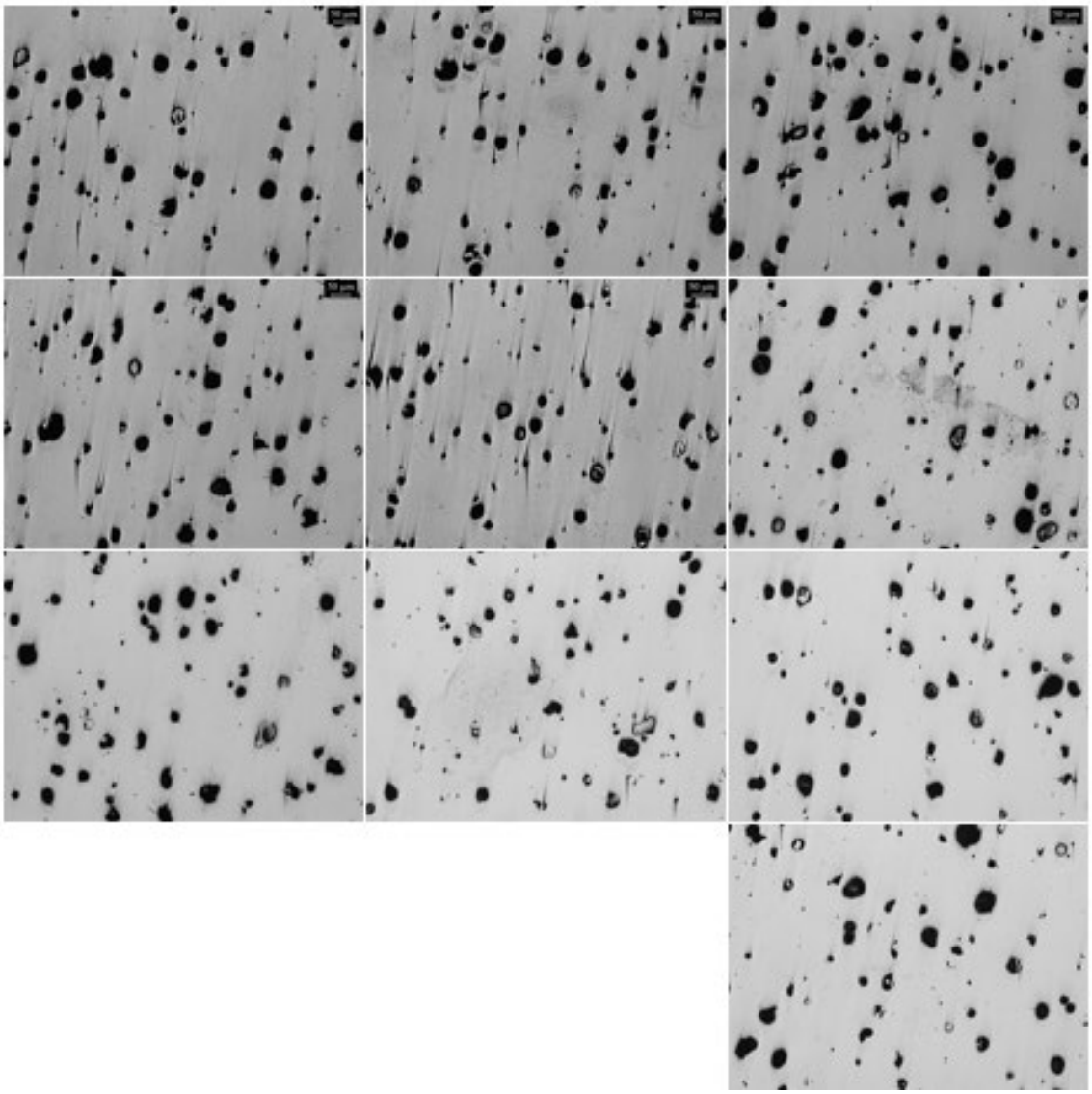

SPECIMEN 12

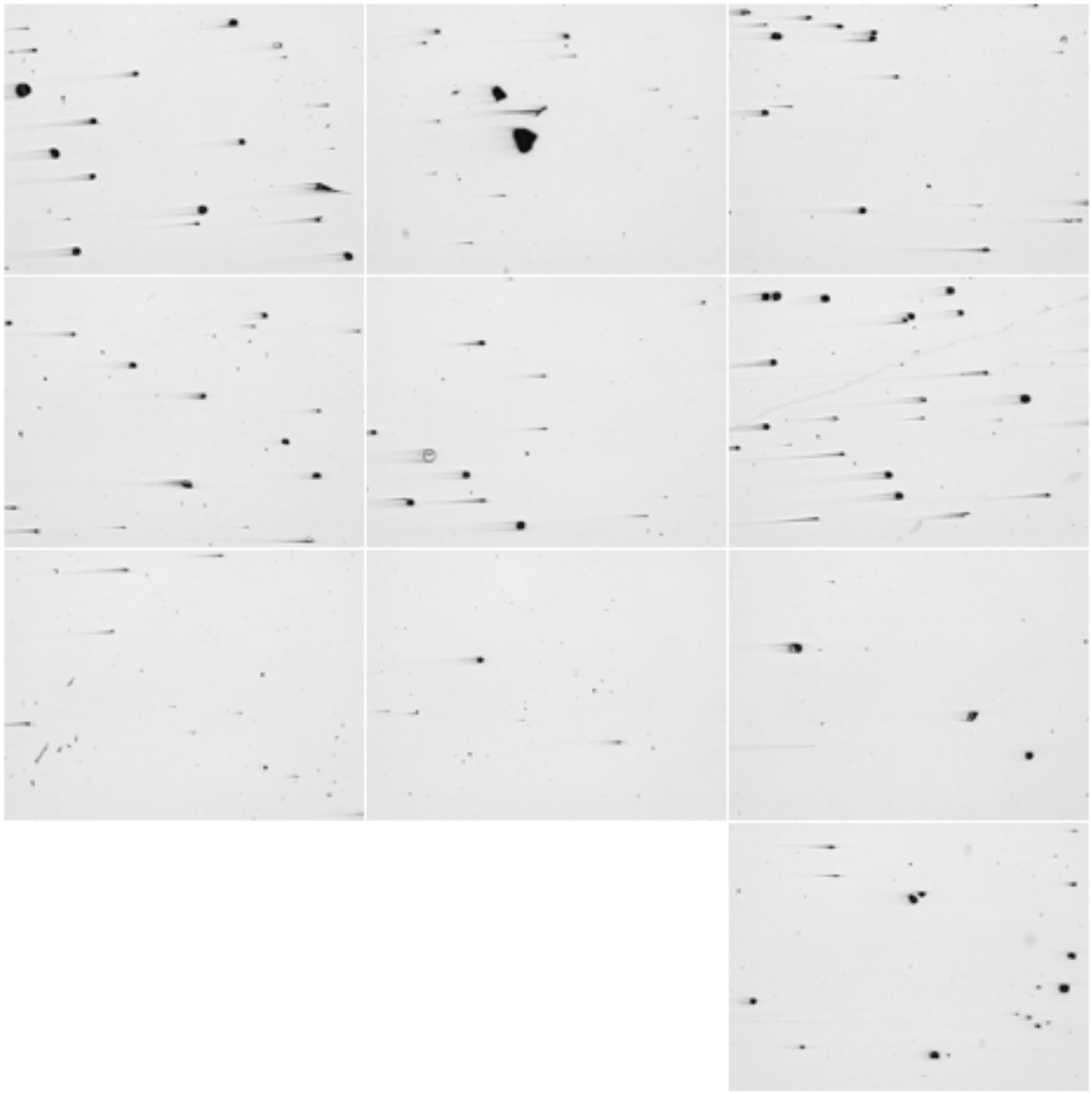

SPECIMEN 13

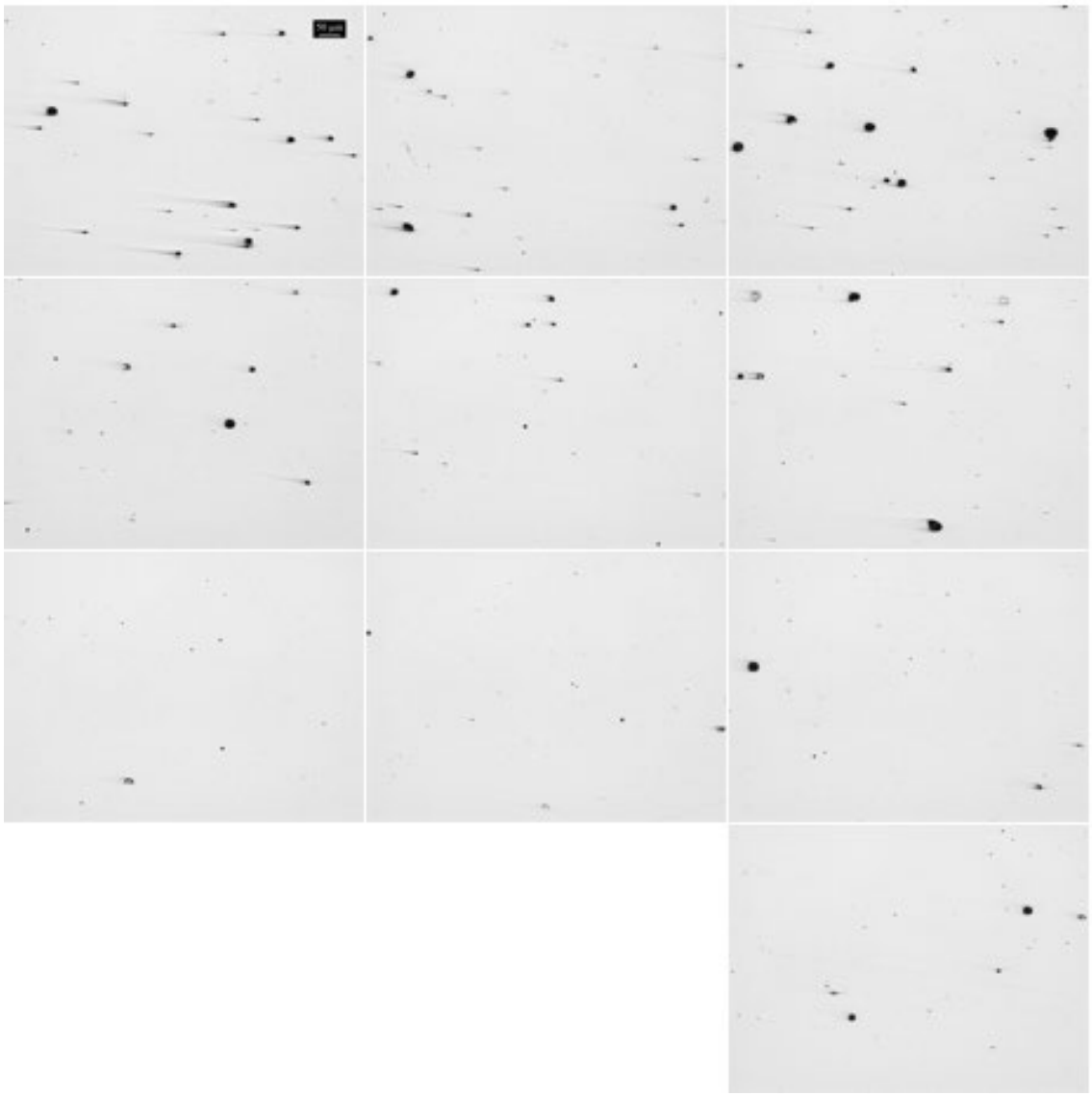

SPECIMEN 14

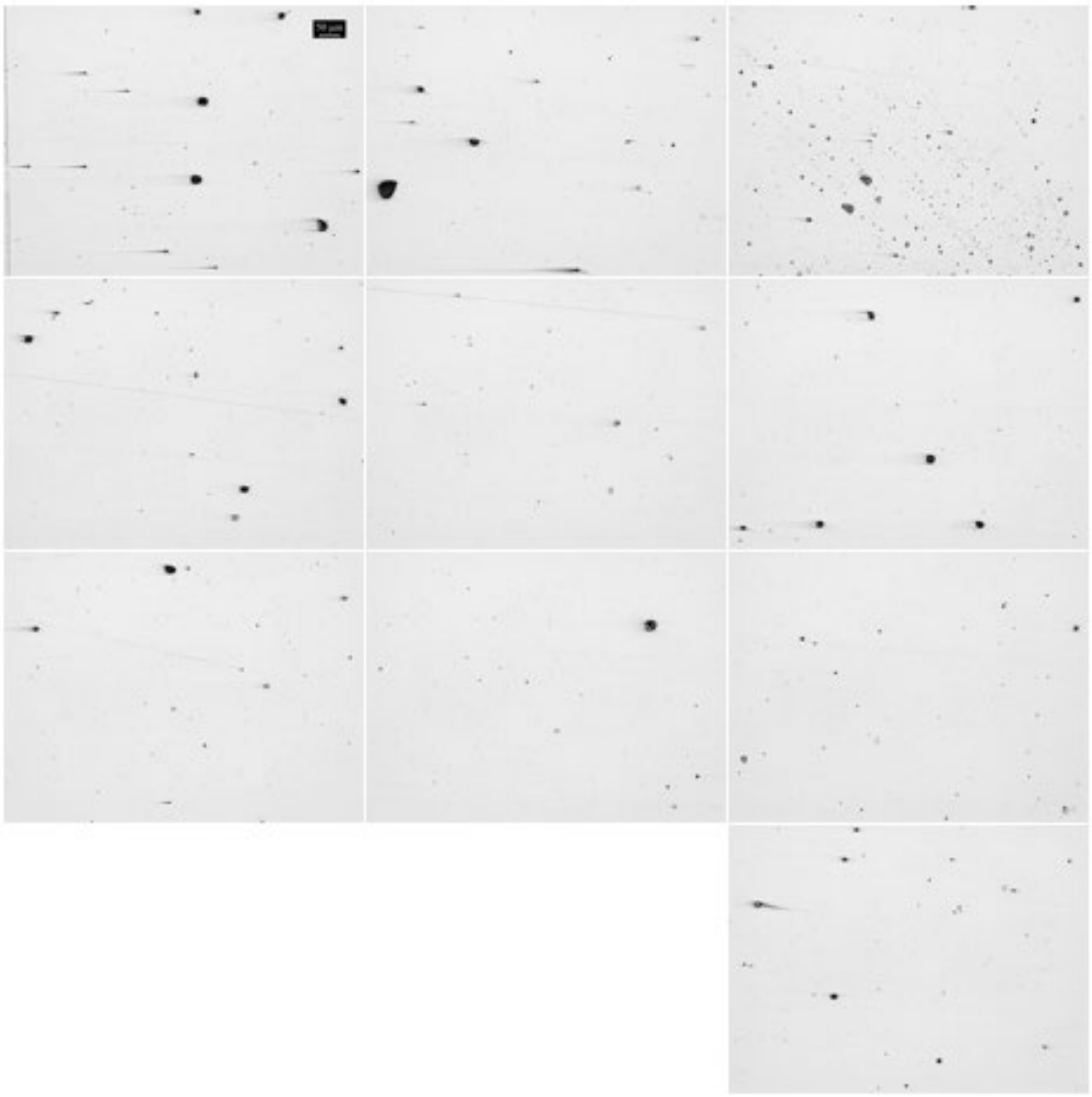

SPECIMEN 15

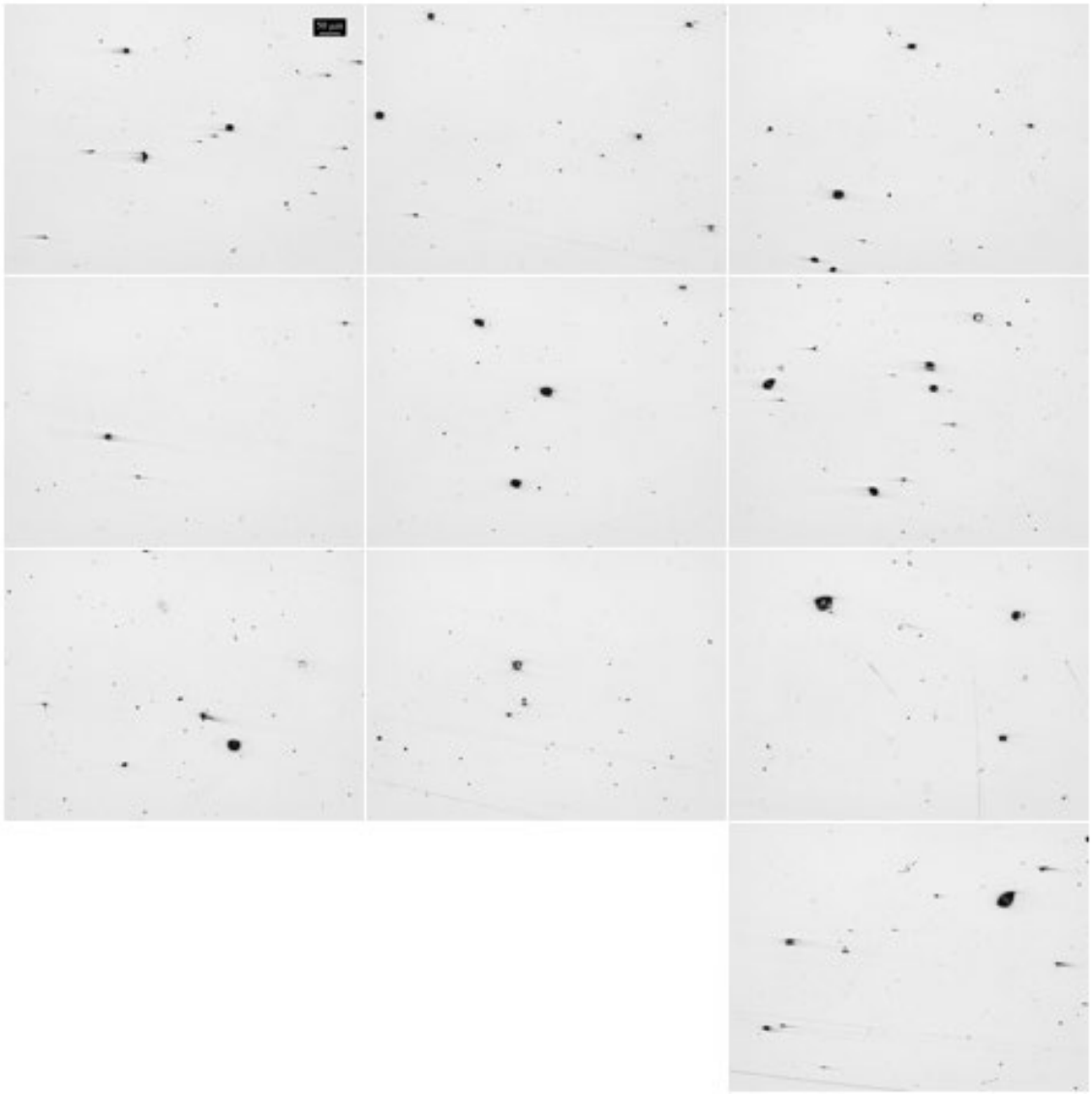

SPECIMEN 16

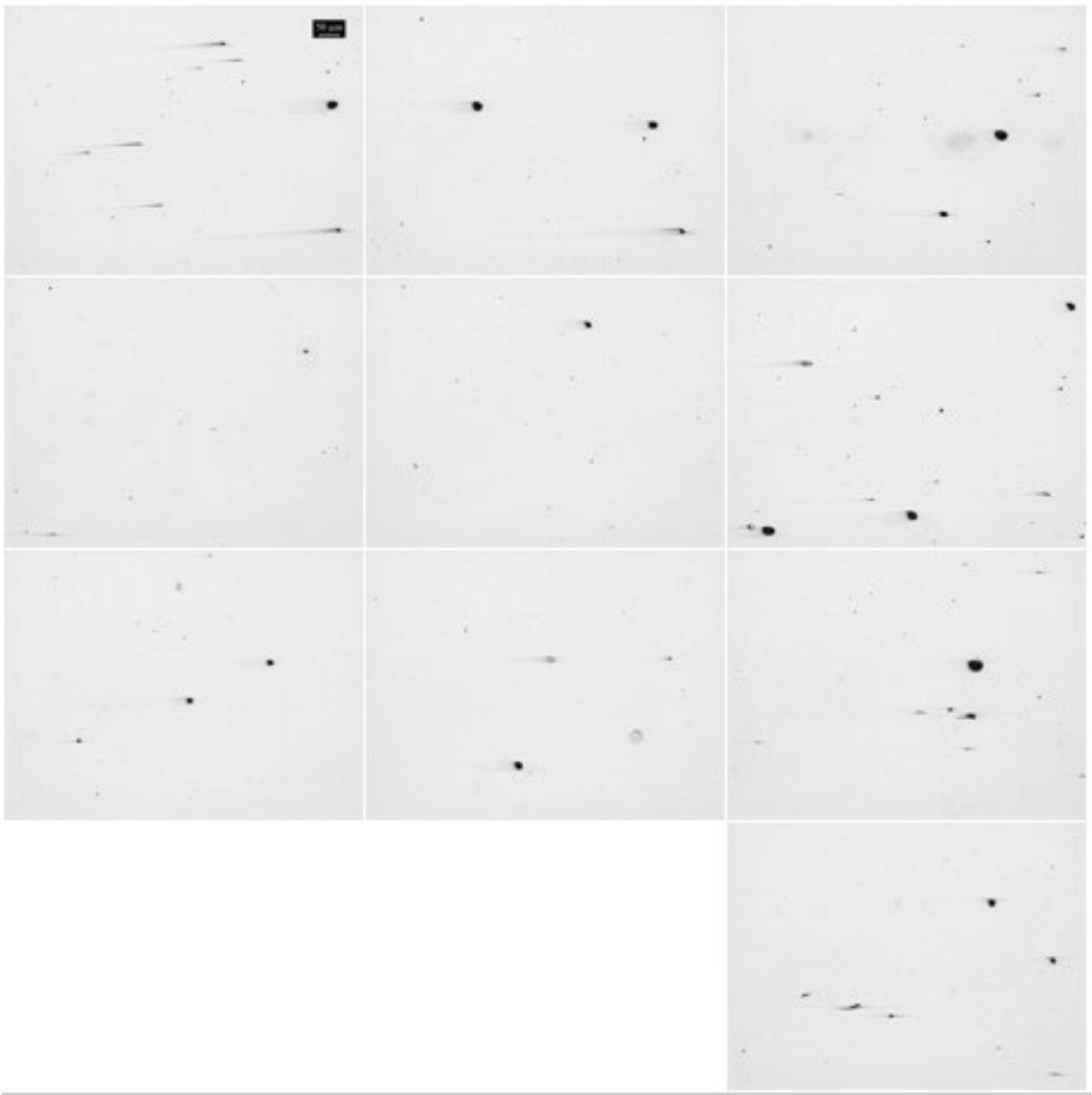

SPECIMEN 17

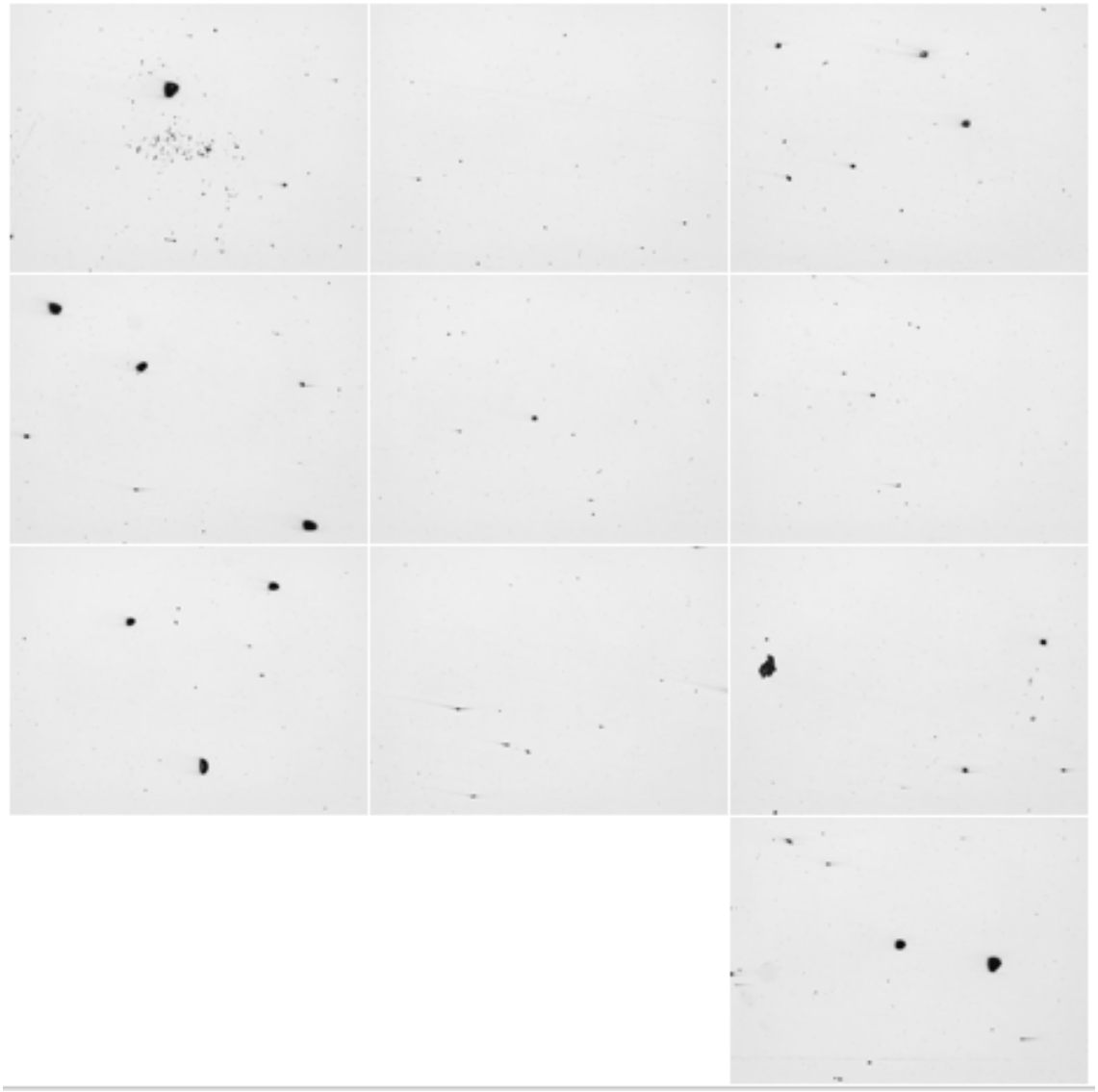

SPECIMEN 18

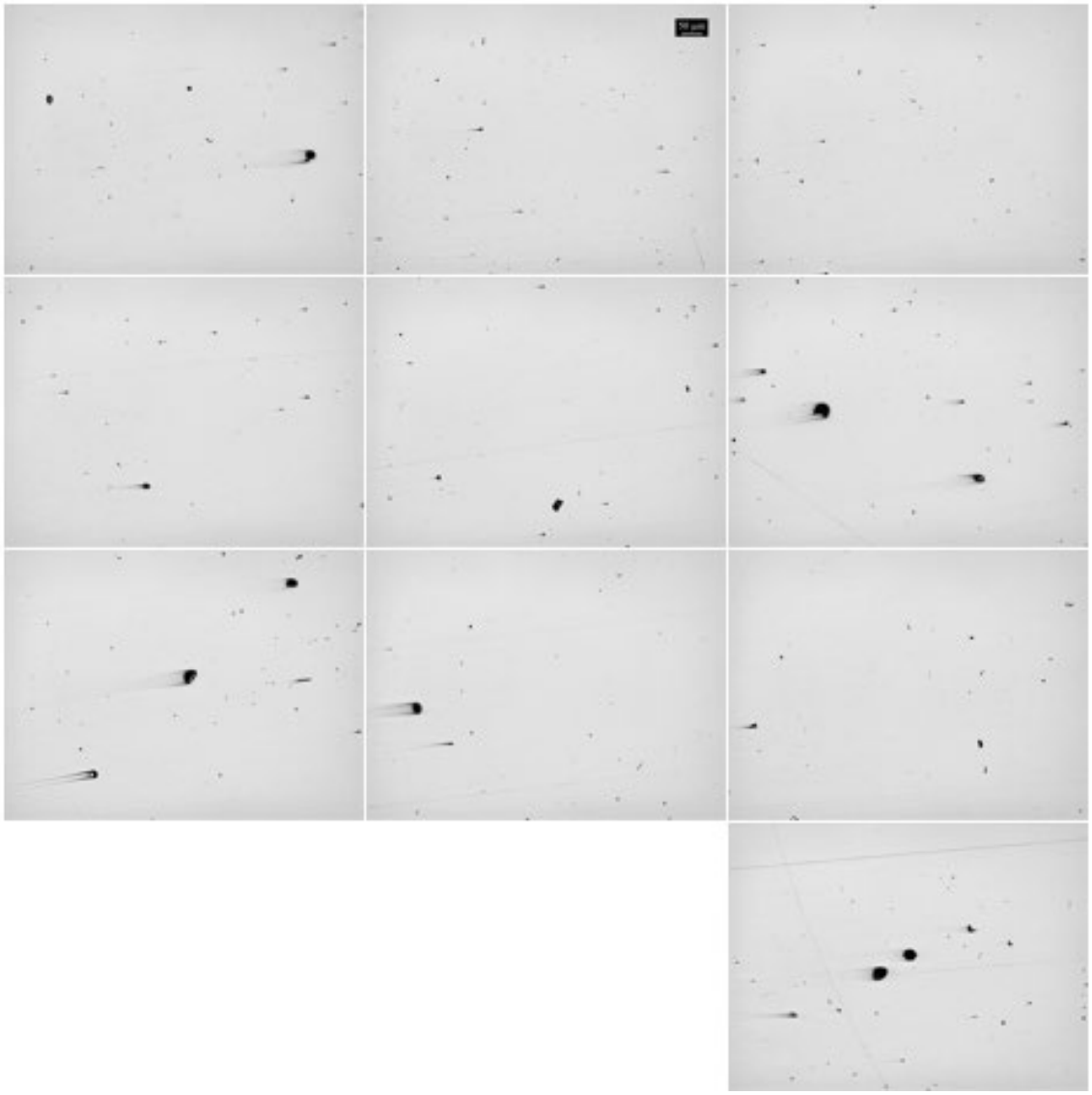

7.4 ANNEX 4 – POROSITY PERCENTAGE OF THE TEN IMAGES ACQUIRED ON EACH SPECIMEN FOR THE MICROGRAPH-BASED METHOD

Table 11 – Annex 4 - Porosity percentage of the ten images acquired on each specimen for the micrograph-based method

Spec.	1	2	3	4	5	6	7	8	9	10
1	7.830	7.555	6.127	7.436	6.650	6.753	6.867	7.982	6.338	6.592
2	4.460	4.328	3.092	4.068	4.349	4.054	5.433	5.563	6.780	4.597
3	5.763	3.312	4.027	4.663	3.789	3.403	3.141	3.839	4.809	5.045
4	4.281	4.682	4.430	4.657	4.026	3.316	2.229	2.701	4.221	5.341
5	5.481	4.845	6.902	3.864	4.449	3.957	4.020	5.122	4.777	5.032
6	3.798	3.450	3.509	2.481	3.686	4.053	2.747	3.489	3.731	3.515
7	1.931	3.233	2.838	2.059	2.175	3.138	1.584	2.161	2.588	2.494
8	2.400	3.338	2.887	2.540	1.814	2.232	2.325	3.081	2.479	2.187
9	2.182	2.228	2.087	2.350	1.289	1.758	1.529	1.197	1.465	1.680
10	1.396	1.294	1.869	1.411	1.696	1.295	1.741	1.255	1.351	1.355
11	6.424	6.268	8.447	6.692	5.886	5.314	5.261	3.449	4.398	4.971
12	0.780	0.665	0.417	0.396	0.293	0.683	0.105	0.099	0.236	0.428
13	0.387	0.256	0.591	0.231	0.183	0.378	0.075	0.066	0.168	0.202
14	0.482	0.504	-	0.245	0.101	0.316	0.207	0.189	0.126	0.198
15	0.240	0.228	0.290	0.087	0.322	0.413	0.267	0.177	0.367	0.444
16	0.120	0.180	0.183	0.047	0.070	0.310	0.103	0.089	0.181	0.102
17	-	0.056	0.164	0.393	0.064	0.075	0.294	0.053	0.110	0.359
18	0.162	0.107	0.100	0.105	0.202	0.401	0.387	0.165	0.128	0.468

7.5 ANNEX 5 – IMAGE MAPPING OF THE SCANNING SPEED AND HACTHING DISTANCE EFFECT ON PORES DISTRIBUTION, SIZE AND SHAPE

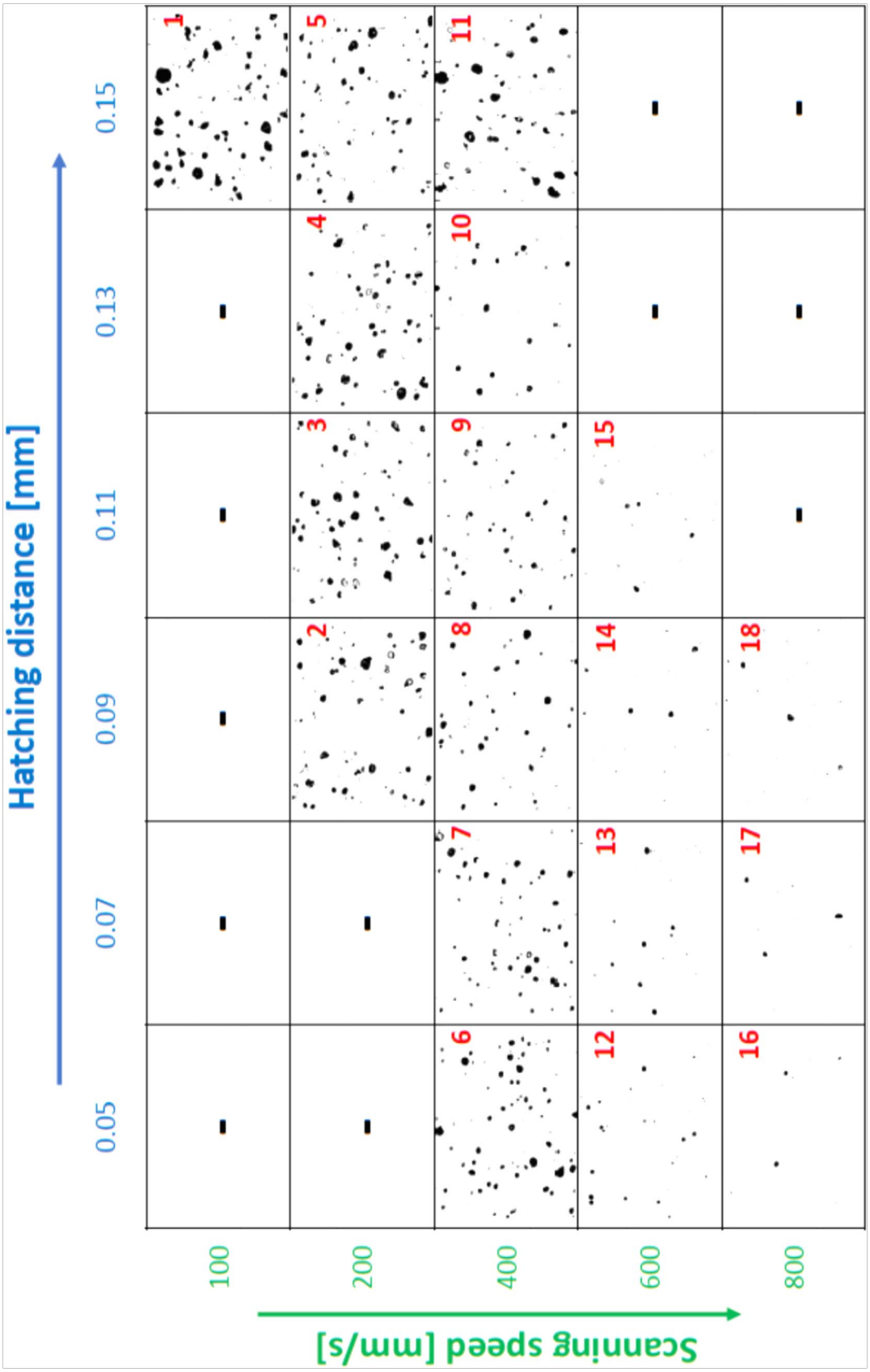

7.6 ANNEX 6 – CALCULATED RESIDUAL STRESSES FOR ALL CONDITIONS (TABLE FORMAT)

7.6.1 ANNEX 6.1 – AS-BUILT CONDITION (TOP)

Table 12 – Annex 6.1 - Detailed residual stress data of as-built specimens (top surface)

Depth [mm]	T1_min [MPa]	T1_max [MPa]	Beta [°]	T2_min [MPa]	T2_max [MPa]	Beta [°]	T3_min [MPa]	T3_max [MPa]	Beta [°]
0.025	88.603	153.179	71.731	14.535	77.111	89.316	-69.599	-25.438	30.836
0.075	296.366	314.133	19.076	178.364	246.852	55.104	163.846	240.198	20.115
0.125	392.178	436.795	12.619	265.871	349.445	44.195	294.148	385.598	19.255
0.175	384.594	433.73	24.194	289.478	364.892	42.276	314.961	396.437	19.907
0.225	323.092	366.365	27.796	280.249	357.622	45.728	300.521	367.225	16.208
0.275	272.826	325.377	37.916	269.711	357.908	46.936	299.879	377.911	12.72
0.325	267.205	326.257	48.254	281.227	367.639	44.792	294.363	389.169	16.308
0.375	294.177	344.367	61.214	318.012	388.898	41.381	301.944	401.844	23.283
0.425	322.02	374.095	73.478	358.424	417.002	37.257	347.65	440.148	31.935
0.475	347.524	407.111	78.97	377.849	438.626	33.04	396.228	471.52	42.795
0.525	375.002	431.87	85.423	376.964	444.508	30.044	422.504	475.772	49.75
0.575	397.027	442.243	-87.451	376.692	437.311	27.762	450.588	486.357	30.116
0.625	406.262	439.948	84.494	388.94	427.192	23.923	470.52	531.915	10.874
0.675	395.375	447.456	64.102	405.083	424.67	10.492	486.948	554.499	11.024
0.725	390.677	467.29	58.602	413.633	435.124	-3.36	502.94	551.94	20.243
0.775	427.942	487.39	54.105	418.932	451.428	-1.426	526.746	573.207	32.286
0.825	496.175	524.051	15.209	423.292	466.542	-0.052	559.085	620.742	35.81
0.875	545.807	614.099	-5.918	424.293	474.356	-3.474	585.461	666.194	40.563
0.925	617.466	697.609	-0.364	418.935	475.831	-10.732	602.56	705.244	47.058
0.975	698.202	774.827	13.124	408.867	476.533	-17.949	617.62	746.326	51.427

7.6.2 ANNEX 6.2 – AS-BUILT CONDITION (LATERAL)

Table 13 – Annex 6.2 - Detailed residual stress data of as-built specimens (lateral surface)

Depth [mm]	L1_min [MPa]	L1_max [MPa]	Beta [°]	L2_min [MPa]	L2_max [MPa]	Beta [°]	L3_min [MPa]	L3_max [MPa]	Beta [°]
0.025	-40.424	72.752	-35.118	-46.555	229.174	-31.624	-101.464	-23.466	-50.223
0.075	74.415	467.841	-37.873	144.264	700.544	-34.801	68.089	347.411	-38.851
0.125	149.745	637.196	-37.581	235.539	899.388	-35.058	151.936	577.482	-37.707
0.175	177.482	634.855	-37.718	239.71	853.676	-35.773	188.617	687.151	-38.121
0.225	190.856	619.567	-38.973	208.548	742.321	-37.639	238.702	768.934	-39.754
0.275	200.11	631.417	-41.434	202.335	717.762	-40.481	258.52	763.618	-42.377
0.325	203.526	627.583	-44.079	231.617	791.564	-43.001	247.77	693.884	-45.77
0.375	218.51	621.7	-46.342	264.872	858.579	-44.423	253.615	664.986	-49.429
0.425	254.246	664.292	-48.105	287.375	845.943	-45.505	263.36	667.589	-51.993
0.475	291.928	738.062	-49.339	302.959	779.446	-47.523	251.617	653.358	-52.9
0.525	308.569	770.533	-50.24	301.427	713.976	-50.804	236.653	646.836	-52.355
0.575	299.457	731.824	-51.005	272.092	661.817	-53.589	236.894	672.799	-51.322
0.625	272.749	660.111	-51.686	234.13	608.644	-55.12	249.34	712.364	-51.189
0.675	240.4	601.845	-52.402	216.028	559.366	-56.943	273.056	756.035	-52.545
0.725	217.723	571.152	-53.646	215.499	532.423	-60.035	298.707	799.374	-54.681
0.775	213.805	561.561	-55.957	205.366	526.874	-62.852	295.476	804.293	-56.587
0.825	217.774	561.35	-59.226	174.977	518.997	-64.034	244.376	742.664	-58.2
0.875	208.743	557.745	-62.451	137.337	491.081	-64.548	163.478	641.642	-59.749
0.925	179.313	548.114	-64.557	103.313	445.389	-65.207	80.459	538.535	-60.985
0.975	138.577	539.756	-65.548	71.086	393.578	-65.912	2.264	439.25	-61.891

7.6.3 ANNEX 6.3 – SOLUTION ANNEALING CONDITION (TOP)

Table 14 – Annex 6.3 - Detailed residual stress data of solution annealed specimens (top surface)

Depth [mm]	T4_min [MPa]	T4_max [MPa]	Beta [°]	T5_min [MPa]	T5_max [MPa]	Beta [°]	T6_min [MPa]	T6_max [MPa]	Beta [°]
0.025	-306.481	-229.837	26.104	-168.105	-131.788	75.841	-116.409	-96.752	11.315
0.075	-129.798	-102.332	25.196	-56.158	-26.419	-61.703	4.39	14.269	-39.673
0.125	-84.705	-70.012	-9.368	-10.3	15.315	-47.524	15.756	43.676	-65.198
0.175	-35.751	-2.41	-7.595	4.009	12.145	1.109	31.743	61.583	-61.422
0.225	42.141	87.307	8.252	3.1	23.679	29.623	42.837	65.793	-54.243
0.275	50.024	88.76	33.609	22.659	36.874	36.587	31.276	39.187	-66.7
0.325	16.215	48.862	70.889	48.837	54.715	-73.941	13.158	26.371	46.837
0.375	10.178	51.63	-79.981	60.665	80.392	-56.782	21.394	42.017	27.31
0.425	43.771	79.049	-73.338	66.729	86.747	-42.711	53.339	76.653	7.696
0.475	78.403	97.926	88.744	57.74	79.305	-11.402	84.576	102.276	-4.097
0.525	84.493	100.599	75.885	43.438	75.761	2.487	91.921	94.606	-63.614
0.575	70.183	81.03	-69.902	54.392	80.832	-1.175	60.005	74.743	87.645
0.625	49.985	68.465	-44.471	79.573	97.787	-29.104	34.952	37.951	73.819
0.675	62.38	79.658	-27.157	87.659	107.52	-40.984	-10.003	16.546	-0.381
0.725	105.067	121.911	-7.289	77.782	93.653	-10.144	-67.18	-23.712	-0.878
0.775	166.179	180.381	-1.308	65.521	96.512	6.78	-111.188	-74.534	1.98
0.825	255.582	262.844	-12.92	92.688	122.412	-1.873	-104.053	-73.893	13.177
0.875	391.558	395.801	-31.013	130.705	158.241	-24.475	-35.879	7.516	18.063
0.925	566.885	573.923	34.649	145.098	169.305	-27.395	65.949	125.095	14.398
0.975	746.715	774.089	41.622	138.234	158.76	3.631	172.221	239.176	9.444

7.6.4 ANNEX 6.4 – SOLUTION ANNEALING CONDITION (LATERAL)

Table 15 – Annex 6.4 - Detailed residual stress data of solution annealed specimens (lateral surface)

Depth [mm]	L4_min [MPa]	L4_max [MPa]	Beta [°]	L5_min [MPa]	L5_max [MPa]	Beta [°]	L6_min [MPa]	L6_max [MPa]	Beta [°]
0.025	-165.679	-121.294	-36.105	-198.261	-174.803	-22.549	-251.769	-236.39	-85.939
0.075	-56.739	-28.258	-46.927	-36.355	26.624	-38.565	-45.141	-13.364	-26.105
0.125	-2.391	21.629	-63.705	29.627	87.938	-34.92	18.273	73.267	-26.108
0.175	39.256	70.189	-54.656	-6.926	44.379	-42.776	28.8	72.882	-35.067
0.225	68.455	110.935	-48.947	4.641	31.765	-42.671	23.1	35.892	-70.612
0.275	70.687	110.279	-54.548	43.214	71.237	-31.203	-17.042	6.132	68.59
0.325	56.282	78.105	-59.44	55.012	110.424	-34.389	-52.005	-30.68	-51.315
0.375	26.557	36.439	9.872	52.47	90.489	-31.939	-95.649	-33.356	-38.7
0.425	14.421	47.722	-4.648	20.2	39.669	40.862	-79.202	-43.671	-27.309
0.475	62.62	135.245	-32.139	-2.207	16.795	43.725	-39.534	-8.56	38.927
0.525	98.43	214.456	-48.696	20.788	68.661	-28.214	18.284	59.008	60.061
0.575	56.918	161.207	-64.551	66.127	141.717	-28.094	76.34	111.756	86.173
0.625	-7.908	35.092	88.368	110.794	119.399	-48.693	94.081	108.855	89.731
0.675	-22.424	40.742	17.916	32.784	129.116	73.487	32.803	67.86	1.666
0.725	54.161	164.286	0.904	0.479	131.323	78.549	-58.271	26.232	-12.884
0.775	153.579	227.024	-12.704	53.99	142.655	87.059	-88.631	10.578	-22.843
0.825	140.358	179.211	-61.726	130.493	161.276	-77.288	-37.698	-4.747	-30.145
0.875	-15.599	66.991	-80.985	171.998	180.892	-16.527	-64.423	-8.172	65.229
0.925	-226.46	-109.527	-83.461	184.788	195.822	20.509	-169.199	-108.144	70.31
0.975	-463.111	-306.243	-85.51	191.424	205.896	58.701	-317.228	-276.117	-62.713

7.6.5 ANNEX 6.5 – SOLUTION ANNEALING PLUS DOUBLE AGING CONDITION (TOP)

Table 16 – Annex 6.5 - Detailed residual stress data of solution annealed plus double aged specimens (top surface)

Depth [mm]	T7_min [MPa]	T7_max [MPa]	Beta [°]	T8_min [MPa]	T8_max [MPa]	Beta [°]	T9_min [MPa]	T9_max [MPa]	Beta [°]
0.025	-39.362	-33.314	40.605	-172.737	-148.926	-65.488	-136.668	-102.155	-31.175
0.075	3.645	10.2	33.928	-44.151	-34.01	-60.47	-36.338	-23.432	-19.633
0.125	9.774	17.199	35.026	19.062	22.785	-48.03	6.898	11.087	-3.166
0.175	9.144	18.189	48.688	31.953	33.923	6.244	17.076	17.896	-70.513
0.225	10.546	15.085	55.264	34.705	38.199	20.687	18.998	20.857	-34.473
0.275	14.575	17.95	40.662	26.648	31.282	16.423	7.59	10.955	7.173
0.325	25.009	36.24	46.311	15.414	20.796	14.056	6.791	14.122	25.532
0.375	37.736	50.191	49.299	28.149	31.016	11.9	28.554	37.325	19.467
0.425	42.793	46.099	37.904	55.565	57.244	-61.284	35.385	41.914	-1.788
0.475	37.013	40.732	1.085	61.825	65.594	-65.716	11.103	14.321	-45.96
0.525	34.086	41.266	36.711	38.791	42.362	-63.744	-5.08	2.891	79.775
0.575	32.836	40.74	49.56	9.437	13.059	-62.077	22.011	36.277	62.052
0.625	28.316	31.691	-55.951	-3.44	-0.006	-63.827	62.06	77.606	53.329
0.675	22.044	34.518	-44.345	2.299	2.918	87.213	69.205	81.967	56.006
0.725	39.352	50.428	-46.996	17.401	22.956	27.948	48.478	60.553	65.486
0.775	64.998	72.149	-54.084	45.693	57.285	20.506	34.154	44.004	60.449
0.825	74.895	82.612	-41.633	79.737	97.061	13.252	23.794	31.613	22.517
0.875	75.946	87.062	-27.116	102.9	123.762	9.05	-7.494	7.745	1.574
0.925	94.55	103.727	-16.313	111.464	128.361	8.286	-48.349	-30.112	2.433
0.975	129.495	134.278	14.195	115.338	121.1	12.974	-85.871	-66.112	13.482

7.6.6 ANNEX 6.6 – SOLUTION ANNEALING PLUS DOUBLE AGING CONDITION (LATERAL)

Table 17 – Annex 6.6 - Detailed residual stress data of solution annealed plus double aged specimens (lateral surface)

Depth [mm]	L7_min [MPa]	L7_max [MPa]	Beta [°]	L8_min [MPa]	L8_max [MPa]	Beta [°]	L9_min [MPa]	L9_max [MPa]	Beta [°]
0.025	-132.725	-128.709	-11.749	-73.857	-55.902	18.801	-96.345	-47.564	-40.323
0.075	-37.656	-29.299	-30.02	-28.668	-13.697	-19.487	-13.784	8.38	-36.39
0.125	-12.676	0.163	-41.477	-0.89	24.766	-32.357	5.616	23.762	-37.495
0.175	-17.979	-5.582	-43.015	9.145	29.296	-28.594	6.351	16.748	-38.109
0.225	-13.777	-3.558	-41.662	12.339	19.593	-16.118	16.265	18.523	44.283
0.275	3.646	16.812	-48.413	19.671	23.352	-70.668	21.521	26.973	38.551
0.325	19.591	37.089	-50.546	25.521	37.06	-69.259	24.095	30.629	18.458
0.375	25.044	40.539	-43.984	29.138	38.782	-63.857	29.744	36.953	5.717
0.425	22.558	34.171	-29.727	30.453	35.317	-33.242	36.395	46.149	-23.95
0.475	23.194	32.705	-29.396	33.709	44.675	-27.7	31.768	52.316	-33.865
0.525	29.915	42.267	-50.827	41.942	63.957	-42.604	21.945	47.808	-32.803
0.575	35.838	54.95	-58.077	45.389	77.051	-52.566	19.559	42.237	-31.815
0.625	37.758	58.342	-54.694	39.777	69.847	-61.761	26.506	47.16	-38.799
0.675	35.77	56.882	-45.532	29.806	51.286	-73.925	31.943	59.696	-45.568
0.725	34.451	61.019	-40.454	25.839	40.331	-80.771	34.979	68.57	-44.572
0.775	36.33	70.126	-40.546	31.522	44.417	-61.956	46.108	76.199	-39.368
0.825	39.403	76.488	-39.454	37.259	58.499	-46.755	66.248	90.868	-32.085
0.875	45.176	79.826	-33.961	41.538	67.006	-40.939	80.526	106.346	-28.43
0.925	57.434	88.982	-24.75	44.634	68.104	-35.133	80.445	111.253	-27.299
0.975	74.48	105.727	-15.544	46.881	67.88	-27.887	74.407	108.095	-24.731